MASTER OF SCIENCE THESIS

Modelling Skin-Stringer Separation in a Post-Buckled Composite Stiffened Panel through Single Stringer Specimens

F.U. Germonpré

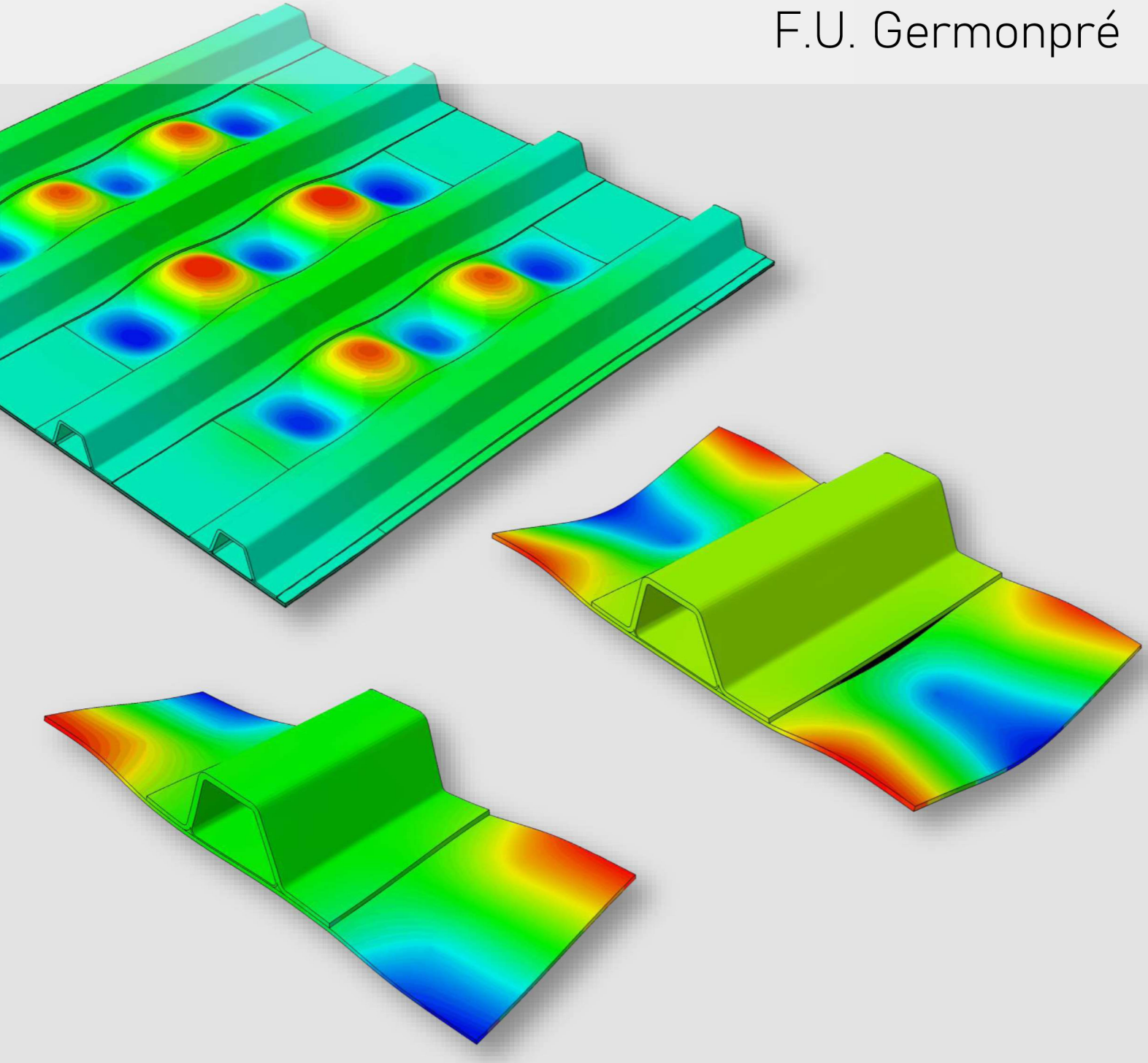

FACULTY OF AEROSPACE ENGINEERING · DELFT UNIVERSITY OF TECHNOLOGY

TU Delft

Modelling Skin-Stringer Separation in a Post-Buckled Composite Stiffened Panel through Single Stringer Specimens

Master of Science Thesis

For obtaining the degree of Master of Science in Aerospace Engineering
at Delft University of Technology

F.U. Germonpré

27 September 2021

Faculty of Aerospace Engineering · Delft University of Technology

Delft University of Technology
Faculty of Aerospace Engineering
Department of Aerospace Structures and Materials

GRADUATION COMMITTEE

Dated: 27 September 2021

Chair holder:

Prof. Dr. Chiara Bisagni

Committee members:

Dr. Calvin D. Rans

Dr. ir. Daniël M.J. Peeters

Dr. Carlos G. Dávila

Abstract

The collapse of composite stiffened panels in compression is complex and involves the interactions of many different failure modes. However, when the panel is allowed to enter the post-buckling regime, skin-stringer separation due to the interaction of the post-buckling deformations with the skin-stringer interface is often the critical failure mode. The accurate prediction of skin-stringer separation in these types of panels is therefore crucial for their design. Due to the high computational costs associated with modelling damage in a large multistringer panel and the manufacturing and testing costs associated with testing such a panel, single stringer specimens that accurately represent the behaviour of critical regions in these panels have been proposed in literature. In this thesis, transversely loaded single stringer specimens are designed and verified and are used to predict skin-stringer separation in the critical regions of a specific multistringer panel.

A specific composite stiffened panel is considered that contains a skin of a tape material and four co-cured stringers of a fabric material. At the intersections of the skin and stringers, resin-rich noodle regions are created. A buckling analysis is first performed on the panel to obtain its post-buckling deformations. Based on these, two types of regions where skin-stringer separation may occur are identified; a mode I dominated skin-stringer separation at the minima of the buckling waves and a combined mode II and mode III skin-stringer separation at the inflection points of the buckling waves. A seven point bending specimen is designed based on the panel deformations near the former critical region, while a four point twisting specimen is designed based on the deformations near the latter region. Finally, detailed damage models are set up for the single stringer specimens to predict skin-stringer separation and the models are verified with the multistringer panel.

The analyses showed that a mode I dominated skin-stringer separation is critical for this panel. The detailed analysis of the four point twisting specimen showed that no damage occurred at the inflection point. To predict the skin-stringer separation at the minimum, a verified seven point bending specimen has successfully been obtained. To do so, it was important to accurately simulate the deformation of the skin at the stringer flange edge, since this proved to be driving for the initiation and propagation of skin-stringer separation. Next to that, a trilinear cohesive law was used to capture the R-curve effect in the tape/fabric interfaces. Finally, a first assessment of the noodle region behaviour showed that damage in this region will probably happen at the location of maximum bending. Recommendations for future research have been provided.

Acknowledgements

The past year has proven to be the most challenging year in my academic career. Working on this thesis full-time for an entire year has put me to the test intellectually, but also emotionally. Having to work mostly from home, I often felt demotivated and discouraged. However, the challenging topic of this thesis sparked my competitiveness and perfectionism in a way that made me push myself to complete this work to the best of my abilities. Nevertheless, I do not think I would have gotten through it without the support of the following people.

First of all, I would like to thank my thesis supervisor, Chiara Bisagni, for proposing this topic to me and for providing excellent guidance. More than once, you steered me back in the right direction when I got off track. I also want to thank Luc Kootte, for always being available for questions, Abaqus related problems or a chat. You really helped me gain a better understanding of the topic. Finally, I would like to acknowledge Dr. Carlos Dávila and Dr. Vipul Ranatunga and their colleagues for providing extra guidance and pushing me to be even more critical.

I want to thank my family for giving me the opportunity to study in Delft and for supporting me in every way I can think of for the past six, but actually, 24 years. I am eternally grateful for that. Papa, thank you for always pretending to know what I am talking about and encouraging me to pursue my passions. Mama, thank you for all the motivational speeches and shoulders to cry on. And Faye, thank you for not only being my sister, but also my best friend and role model.

I am so grateful for the friends I have made in Delft. You have become a second family and have made Delft feel like home. Specifically, I want to thank my best friend/roommate/twin, Kaat. You have literally been by my side for the past six years. I hope you know how much that meant to me. Thanks to my roommate Isaac, for being the best roommate I could have wished for. And thanks to my best friend Harry, for being my library buddy, feeding me and hyping me up, always.

Finally, I want to thank my boyfriend, Benjamin, for never asking about my thesis unless I wanted to talk about it, for never failing to make me smile and cheer me up at the end of the day and for making me feel like the best version of myself. Thanks for being you, because you are great.

Delft, University of Technology — F.U. Germonpré
27 September 2021

Table of Contents

List of Figures

List of Tables

Chapter 1

Introduction

Composite stiffened panels can provide efficient structural solutions, as they contain load carrying capabilities beyond their critical buckling load. However, due to the complex nature of the collapse of these structures in compression, they are often designed conservatively as to not exceed their critical buckling load. The collapse involves the interaction of many different damage mechanisms, but from experimental observations and literature, it becomes clear that, when the panel is allowed to enter the post-buckling state, skin-stringer separation due to the interaction of the skin-stringer interfaces with the post-buckling deformations of the panel is often the critical failure mode [1–5]. In order to reduce the conservatism in the design of composite stiffened panels, an accurate prediction of skin-stringer separation is necessary.

Different methodologies to do so have been developed in past studies. Since a numerical model of a multistringer panel can become computationally expensive due to its large size and small mesh size requirements for the accurate modelling of the different damage mechanisms, it can become impractical for designing purposes. On top of that, to obtain data to validate the design, extensive testing of the multistringer panel is required, which can become time-consuming and expensive. A more computationally efficient way to analyze a multistringer panel is through smaller, single stringer specimens that are representative of the behaviour of the multistringer panel in critical regions where skin-stringer separation is likely to occur. This way, detailed damage models can be developed for the single stringer specimens rather than for the multistringer panel. Numerically, the computational expenses are significantly reduced due to the smaller size of the model, while experimentally, the manufacturing and testing costs are decreased [6]. Single stringer specimens on which the post-buckling deformation is enforced through transverse loading show a lot of potential. Seven point bending specimens have been developed to simulate skin-stringer separation due to the skin pulling away from the stringer and more recently, a four point twisting specimen has been developed as well. In this specimen, the skin-stringer separation that can occur due to twisting of the skin with respect to the stringer at the inflection points of the buckling waves, is simulated.

The goal of this thesis work is to develop a numerical tool that is able to capture skin-stringer separation at critical locations of a specific composite multistringer panel in compression by means of transversely loaded single stringer specimens in a seven point bending or four point

twisting configuration. The design of the single stringer specimens should be verified to ensure that they are representative of the behaviour of the multistringer panel. Furthermore, the considered panel contains four hat stringers, made out of a fabric material, while the skin is built using a tape material. At the intersections of the skin and stringer, resin-filled pockets are created. These panel characteristics should be accurately incorporated in the numerical models.

The thesis is structured as follows. First, an extensive literature study is performed to evaluate the work that has been done on this topic in the past. This can be found in chapter 2. Then, in chapter 3, the composite stiffened panel considered for this work is described in detail and a methodology to achieve the objective is proposed. In chapter 4, preliminary analyses are performed on a generic seven point bending specimen to investigate how to model the panel characteristics and to evaluate the sensitivity of the panel to different modelling parameters. Next, the multistringer panel in consideration is modelled to obtain its post-buckling behaviour. This is described in chapter 5. Based on the post-buckling deformations of the multistringer panel, the regions where skin-stringer separation is expected to occur are identified. A seven point bending and a four point twisting specimen are then designed such they show a similar deformation as the multistringer panel in the corresponding critical region. This is reported in chapter 6. As a final step, in chapter 7, detailed damage models are developed for the single stringer specimens to predict skin-stringer separation. The specimens are then verified with the multistringer panel. Finally, conclusions are drawn and recommendations are given for future work.

Chapter 2

Literature Study

A literature study is performed to investigate what has been researched on the topic of skin-stringer separation of composite stiffened panels in post-buckling thus far. Furthermore, the composite stiffened panel considered in this research is a panel consisting of a tape skin and four fabric co-cured hat stringers. The stringer cross-sections are closed and resin-filled pockets occur at the intersections between the skin and stringer [3]. These are referred to as the noodle regions. Different methodologies on how to incorporate these panel specifications in a finite element model and what effect these may have on the panel performance are researched.

2.1 Skin-Stringer Separation in Composite Stiffened Panels

Composite stiffened panels can provide efficient structural solutions: composite materials have high specific properties and stiffened panels contain load carrying capabilities beyond the critical buckling load. When the critical buckling load is exceeded, the composite stiffened panel enters the post-buckling regime. Further increasing the load will eventually lead to the collapse of the panel, which is a complex phenomenon, involving interactions of different damage mechanisms [1]. From literature, it becomes clear that one of the main critical failure modes of a post-buckled panel is skin-stringer separation [1–4]. When the panel enters post-buckling, the skin in between the stringers locally buckles. The out-of-plane displacements of the skin interact with the stringers, causing high interlaminar stresses at the skin-stringer interface and damage can initiate, especially in the presence of pre-existing defects, such as impact damage or a delamination, and geometric discontinuities [7–11]. When the load is further increased, the damage propagates and eventually the skin and stringers separate. At this point, the load within the panel has redistributed and the stringers take up all of the load, which can cause them to fail in crippling. This results in the collapse of the panel [6, 12–16]. Apart from interlaminar damage at the skin-stringer interface, other damage mechanisms can also occur, such as fiber or matrix failure. However, these are usually not critical but can interact with or trigger more critical failure modes [1, 13].

2.2 Single Stringer Specimens

Different methodologies have been developed in the past to predict the collapse of post-buckled composite stiffened panels. However, due to the large sizes of these panels and the small mesh size requirements for the accurate modelling of different damage mechanisms, a numerical model of a multistringer panel can be computationally expensive and therefore impractical for design. On top of that, to validate the numerical model, extensive testing is required. Testing a large multistringer panel can become time-consuming and expensive. Single stringer specimens can be used as a representation of the multistringer panel. They bridge the gap between coupon and sub-component analyses. From an experimental point of view, the use of single stringer specimens is advantageous due to the low manufacturing and testing costs. Next to that, from a numerical point of view, the computational effort required is reduced compared to the analysis of a multistringer panel [6]. In literature, the most commonly used single stringer specimen is the single stringer compression specimen (SSCS) [4, 6, 9, 15–24]. However, these studies show that the SSCSs are imperfection sensitive, which leads to a high variability in terms of buckling mode shape. This changes the stress distribution within the specimen and therefore the damage initiation, propagation and collapse. This makes it difficult for numerical models to correctly predict the buckling mode shapes and deformation patterns. Next to that, the damage mechanisms in a SSCS happen suddenly and almost simultaneously, making observation and monitoring of the damage sequence during testing challenging. Finally, Vescovini et al. recognized that skin-stringer separation occurs due to the interaction of the skin-stringer interface with the post-buckling deformation. Most studies focus on a mode I dominated skin-stringer separation that occurs at locations where the skin peels away from the stringer. However, a combined mode II and mode III skin-stringer separation can also occur at the inflection points of the buckling waves due to twisting [25]. Orifici et al. also observed this [26]. Therefore, to study these separation modes separately and more progressively and to remove the influence of geometric imperfections on the buckling mode, two alternative single stringer specimens have been proposed in literature: a seven point bending (7PB) specimen and a four point twisting (4PT) specimen.

2.2.1 Seven Point Bending Specimen

In several studies, a 7PB specimen has been proposed for the investigation of damage initiation and propagation caused by mode I peeling. Mode I dominated skin-stringer separation is caused by the skin peeling away from the stringer at the antinodal lines of the buckling waves. This corresponds to a region in the panel where bending of the skin is maximum [25]. The 7PB specimen was developed at NLR, by Rijn and Wiggenraad [27] to determine the strength of the skin-stringer interface in composite aircraft panels. The 7PB configuration consists of five lower support points and two upper loading points. This way, three point bending is enforced along the centerline of the specimen, while the edges are constrained by the remaining four supports. This configuration allows for the investigation of a mode I dominated separation. Furthermore, while the specimen is loaded transversely into the post-buckled shape, damage propagates in a stable way, facilitating the gathering of validation data and the monitoring of the damage progress [5, 28].

Bertolini et al. [29] performed a numerical and experimental investigation of single stringer specimens in a 7PB configuration. The specimens contained a blade stringer and a pre-

embedded delamination underneath the flange. The 7PB configuration was used to create symmetric buckles, to mimic the response of a multistringer panel in compression, and antisymmetric buckles, to mimic the response of a multistringer panel in shear. The position of the support and loading points could be modified to simulate different displacement fields. The symmetric load case is shown in Figure 2.1. To model the supports, rigid bodies were used.

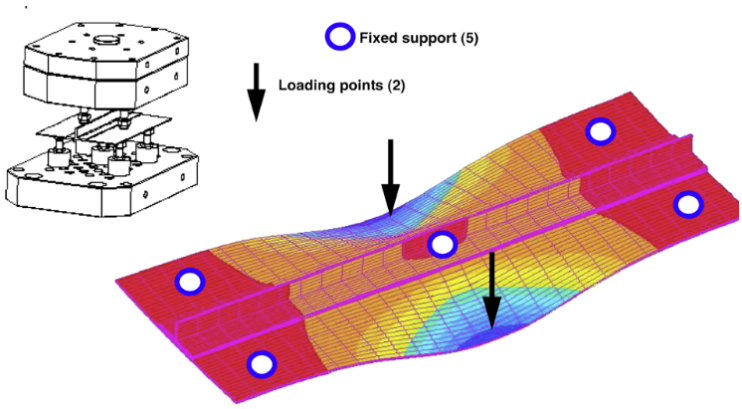

Figure 2.1: Symmetric 7PB configuration, proposed by Bertolini et al. [29].

Dávila et al. [30] investigated a 7PB specimen experimentally to examine the damage initiation and propagation related to skin-stringer separation, in a controlled manner. The damage propagation in a 7PB specimen is somewhat stable, allowing for good observation of the details involved in the skin-stringer separation. This is advantageous compared to the sudden collapse of SSCSs. The deformation achieved was similar to the post-buckling deformation of composite stiffened panels in compression. The study was purely experimental: the load was applied incrementally and ultrasonic inspection was performed after every step to monitor the damage propagation and gather validation data. The test rig used can be seen in Figure 2.2.

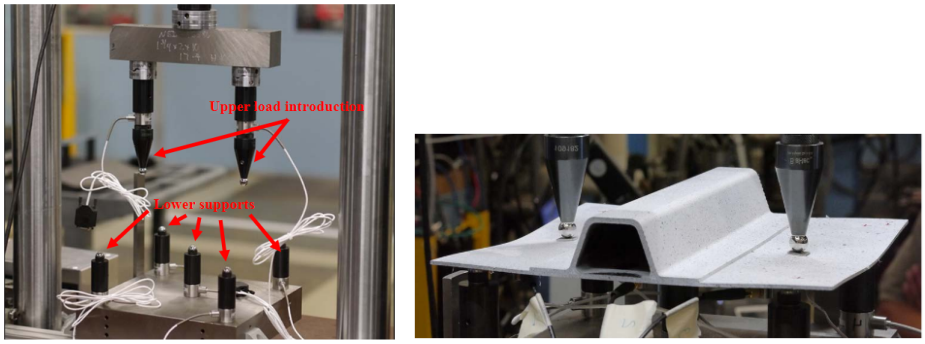

(a) 7PB test rig. (b) 7PB specimen in the test rig.

Figure 2.2: The test set up used by Dávila et al. to load a 7PB specimen in a post-buckled shape [31].

In [28] and [31], these 7PB specimens were numerically modelled by Leone et al. and Kosztowny et al. respectively. The test conditions were simulated and the supports and loads were

displaced in opposite directions, to reduce the kinetic energy exerted on the specimen. The loads were introduced through the displacement of spherical rigid bodies. Leone et al. analyzed three initial damage states of the specimen: (1) pristine; (2) containing a pre-embedded delamination and; (3) impact damage to the flange.

Finally, Kootte et al. recognized the potential of the 7PB specimen and conducted a study in which a 7PB specimen was developed that was able to capture the behaviour of critical locations of a multistringer panel. In [32], a multistringer panel was first considered to obtain the post-buckling shapes and identify the critical locations. The critical locations were defined as regions where skin-stringer separation in either mode I or mode II+III was expected to occur. For mode I, the location where the out-of-plane deformation of the skin, away from the stringer, is maximum, was identified as the critical location. A single stringer specimen in a 7PB configuration was then sized to represent this location: it was sized such that a full buckling wave was captured on each side of the stringer, with the location of maximum bending at the center. The relative position of the five support points and two loading points was determined such that the displacements resembled the displacements of the corresponding region in the multistringer panel as well as possible. This was done using the Residual Sum of Squares (RSS) methodology. The loading configuration resulting in the lowest RSS then corresponded to the best approximation of the post-buckled shape.

In [33], Kootte and Bisagni extended the study by modelling skin-stringer separation on the 7PB specimen. First, the multistringer panel was modelled and the region in which skin-stringer separation was expected to occur was refined and contained cohesive elements to predict the onset of interlaminar damage. This way, the critical location and the post-buckled shape at which skin-stringer separation initiates, was identified. Then, using the methodology described in [32], a 7PB specimen was sized and the loading configuration was determined. A more detailed analysis was then performed on this specimen to capture interlaminar damage initiation and propagation. The specimen was loaded through the displacement of rigid hemispherical surfaces. The model was validated using experimental data. Tests were conducted using adaptive multi-point testing equipment, which has the ability to move the relative position of the support and loading points, enabling the exact recreation of the loading configuration used in the numerical models. A recommendation was given to extend this methodology to different panel configurations.

2.2.2 Four Point Twisting Specimen

Skin-stringer separation does not only occur in mode I, but can also occur in a combination of mode II and mode III at the inflection points of the buckling waves, where there is twisting of the skin. These points can even be critical if there is a low bending stiffness mismatch between the skin and the stringer flange. Kootte et al. came up with a testing configuration to capture the behaviour at this critical location. To do so, a similar procedure was followed as described for the 7PB specimen in [32]. A model of the multistringer panel was developed to capture the post-buckling shape and identify locations where skin-stringer separation was likely to occur. For a mode II+III separation, this corresponded to a location where twisting of the skin is maximum. A single stringer specimen in a 4PT configuration was then sized to represent this location. It should be noted that with the 4PT configuration, a configuration similar to the Edge Crack Torsion test is meant: the test rig consists of two lower supports and two upper

loading points, placed diagonally. This way, the specimen is subjected to opposite torsional moments at its ends [34–36], see Figure 2.3. The specimen was sized such that the inflection point of the buckling wave on both sides of the stringer was captured. The relative position of the supports and loading points was determined such that the displacements resembled the displacements of the corresponding region in the multistringer panel as well as possible. Similar as for the 7PB specimen, this was done through the RSS methodology.

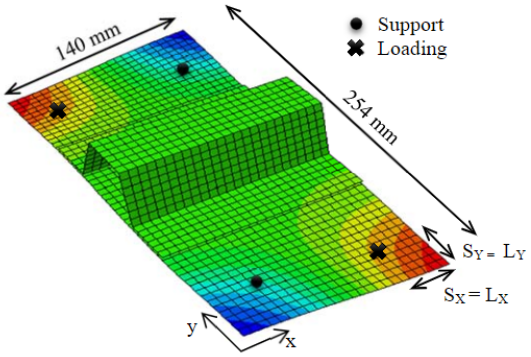

Figure 2.3: Loading configuration of the 4PT specimen [32].

In [33], Kootte and Bisagni extended the study by modelling skin-stringer separation on the 4PT specimen. The model was validated using experimental results obtained from tests using the adaptive multi-point test equipment, mentioned before. The test set up can be seen in Figure 2.4. The authors could conclude that this novel 4PT configuration on a single stringer specimen was able to capture the skin-stringer separation in a combined mode II and mode III opening.

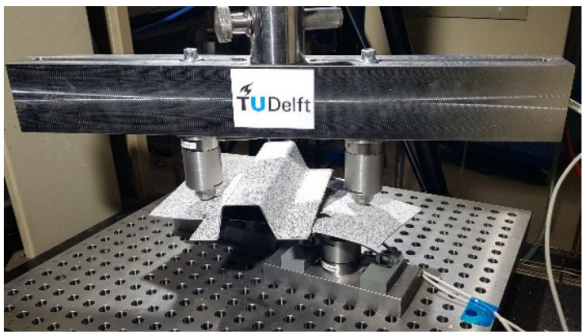

Figure 2.4: The adaptive multi-point test equipment for testing a single stringer specimen in a 4PT configuration [33].

2.3 Tape/Fabric Interfaces

Sometimes, in composite stiffened panels, the skin is manufactured using tape materials, while the stringer consists of fabric material. Usually, this is done because the stringer has a more complex shape and requires a more drapable material [37]. However, composites

are susceptible to delaminations, especially at dissimilar interfaces, where high interlaminar stresses are generated due to the difference in elastic properties between the two materials [38].

In fracture mechanics, the onset and propagation of a delamination are characterized by the strain energy release rate, which represents the energy that is dissipated per unit of propagated delamination area. The strain energy release rate can be decomposed into three components: the mode I component, the mode II component and the mode III component [39]. These can be seen in Figure 2.5. In mode I, two plies separate due to interlaminar tensile stresses; they peel off of each other. In mode II, the plies separate due to in-plane shearing or sliding, and in mode III, the plies separate due to transverse shearing or scissoring [40]. The resistance to delamination initiation and propagation is referred to as the critical strain energy release rate or interlaminar fracture toughness. The interlaminar fracture toughness for each of the modes is obtained experimentally through standardized tests and is considered inherent to the material. To predict onset or growth of the delamination, the strain energy release rate along the front is calculated and compared to the interlaminar fracture toughness: exceedance of the fracture toughness results in propagation [40].

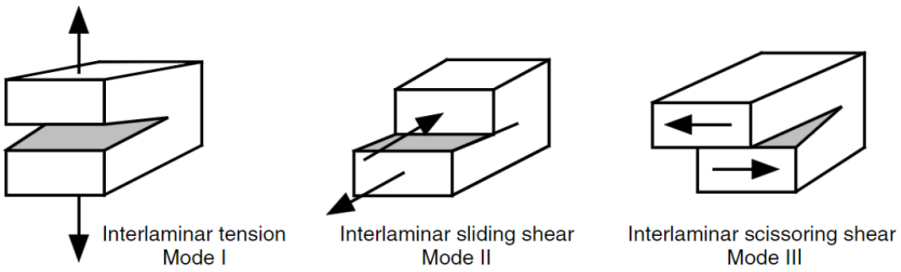

Figure 2.5: Separation modes of a composite laminate [40].

In the standardized tests, the specimens are unidirectional laminates containing a pre-embedded delamination at their mid-plane. The interlaminar fracture toughness is derived from the first point of non-linearity in the experimentally obtained load-displacement curve. Therefore, the value of the fracture toughness relates to the onset of damage. However, interfaces in actual structural components are generally multi-directional or even consist of different materials, as is the case for the considered composite stiffened panel, which contains a tape/fabric skin-stringer interface. Separation between dissimilar interfaces is usually accompanied by complex interactions of matrix cracks, fiber bridging, migrating delaminations, etc. This results in a toughening effect and increases the fracture toughness. This is known as the crack growth resistance curve or R-curve: as the delamination propagates, the fracture toughness increases to a steady-state value. This R-curve effect is more explicit in dissimilar interfaces [30]. This is illustrated in Figure 2.6, which shows the R-curve effect of typical interfaces. Therefore, the use of standard interlaminar properties when modelling non-standard interfaces can lead to discrepancies with experimental data, especially when substantial damage is present [4, 17, 33].

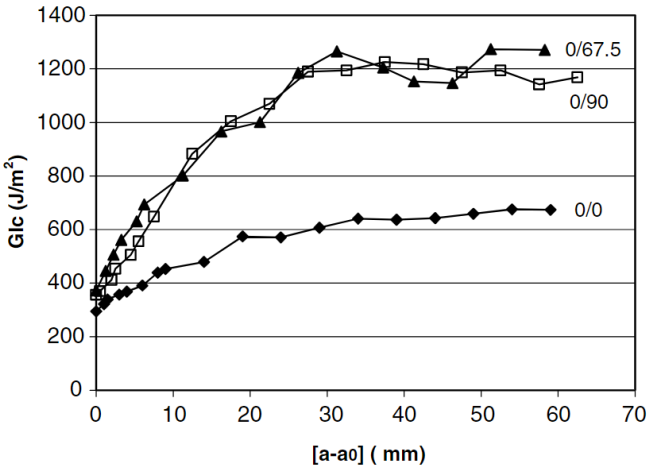

Figure 2.6: R-curve effect of different interfaces [41].

In literature, efforts have been made to incorporate the effect of the R-curve into a numerical model. To capture the R-curve effect in a numerical model, a very detailed three-dimensional model, accounting for every damage mode at every interface and location could be developed. The reasoning behind this is that since the R-curve effect exists due to damage mechanisms, other than just delamination, that blunt the crack tip, by capturing all of these, the model should be able to predict the R-curve. However, the R-curve effect is often also caused by sub-ply mechanisms and surface effects, which cannot (yet) be modelled using current methodologies. Alternatively, an empirical approach could be developed that is able to account for all of these mechanisms. Essentially, the separation of two components is represented by a material law at a single interface that accounts for all of the damage mechanisms causing the R-curve effect. It should be noted that this approach is an approximation of the actual physical phenomena associated with the separation of two composite components. As can be seen in Figure 2.7, the separation does not just consist of a delamination at the interface, but includes migrating delaminations, transverse matrix cracks, matrix cracks at different planes etc. [30, 31].

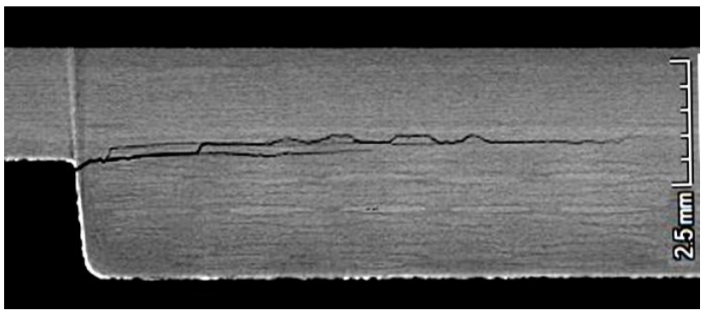

Figure 2.7: Damage mechanisms associated with the separation of two composite components [30].

Several studies have been conducted on this. Dávila et al. [30] tested specimens containing a tape/fabric interface in the Double Cantilever Beam (DCB), End-Loaded Split (ELS) and

Mixed Mode Bending (MMB) tests. The specimen layups contained a mixture of fabric and tape plies. From these tests, the critical strain energy release rate for the tape/fabric interfaces was derived. To represent the R-curve effect, a trilinear cohesive law was proposed at a single interface. The trilinear law was incorporated through the superposition of two bilinear cohesive laws. This can be visualized in the following figure, Figure 2.8. Here, σ_{c1}, $\sigma_{c,2}$ and $\sigma_{c,T}$ correspond to the interlaminar strengths of the individual bilinear laws. The area underneath the curves is equal to the corresponding interlaminar fracture toughness, G_1, G_2 and G_T. The displacement δ_0 corresponds to the opening displacement of the interfaces at which damage initiates. It can be seen that δ_0 is the same for all cohesive laws, which corresponds to what is observed in Figure 2.6: the behaviour of the different interfaces is similar up until damage onset. Displacements δ_1 and δ_2 then correspond to the separation of the interfaces at which the crack propagates. Cohesive laws are explained in more detail in section 2.5.

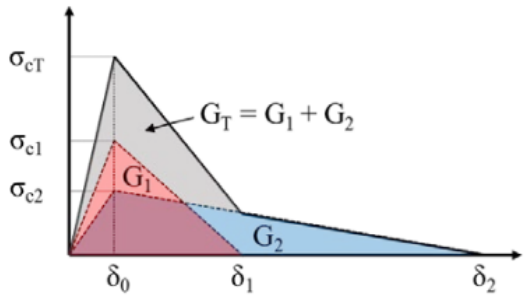

Figure 2.8: The trilinear cohesive law as a superposition of two bilinear cohesive laws [31].

The first cohesive law is based on the standard interlaminar properties (tape/tape), as these correspond well to the first non-linearity observed in experimental results. This law is represented by the red curve in Figure 2.8. The second bilinear cohesive law is referred to as the "bridging" law (in blue) and is based on the difference between the steady-state fracture toughness values from the standard (tape/tape) and non-standard (tape/fabric) interfaces. It represents the fact that the fracture toughness increases as the crack grows. Using this trilinear cohesive law in the numerical models for the DCB, ELS and MMB tests, showed an excellent agreement with experimental results. The same law was then applied in a numerical model of a three point bending (3PB) doubler specimen, containing a tape skin and a fabric patch. Upon comparison with experimental results, it was seen that the onset of damage was captured well, but after some damage propagation, the ability to carry load was underpredicted. The "bridging" properties were then increased, such that the total of the standard interlaminar properties (tape/tape) and the new "bridging" properties was equal to four times the standard tape/tape properties. This comes from previous studies that have shown that for arbitrary interfaces, there is an increase of approximately 400% of the standard interlaminar properties (tape/tape) [42]. This resulted in a better agreement with experimental results.

The trilinear cohesive law described above was also used by Kosztowny et al. [31] on a 7PB specimen. Cohesive elements were included at the skin-stringer interface and the analysis was run using three types of material properties: (1) a single bilinear cohesive law with the standard interlaminar properties (tape/tape) (the cohesive base), which resulted in an

overprediction of the damage and an underestimation of specimen stiffness after damage onset; (2) a superposition of the cohesive base and the "bridging" properties, as defined by [30] and (3) a superposition of the cohesive base and an increased set of structural "bridging" properties, as done by [30]. The results were more accurate in the last two analyses, but damage growth was underpredicted.

Leone et al. [24] and Action et al. [1] took a different approach and implemented cohesive elements at the skin-stringer interface and between the top-most skin ply interfaces of the SSCS and the multistringer panel respectively. At the skin ply interfaces, a single bilinear cohesive law based on standard properties was used, while at the skin-stringer interfaces, two sets of interlaminar properties were used in a single bilinear cohesive law: the tape/fabric values for damage onset and for the steady-state, obtained in [30]. The results with either of these sets showed inaccuracies with experimental data in terms of the damage and peak loads.

Nikishkov et al. [43] developed a numerical model of a single hat stringer specimen with a mechanically attached aluminium rib under compression and pull-off loading. The skin was made of unidirectional tape material, while the hat stringer was manufactured from a fabric material. The authors recognized that providing correct material data input is crucial to produce accurate numerical predictions. Therefore, material characterization tests were performed on coupon specimens to determine the appropriate material properties for tape/tape, fabric/fabric and tape/fabric interfaces. These properties were then used for the cohesive elements at the skin-stringer interface in the numerical models.

2.4 Noodle Region

The noodle region is defined as the region at the intersection of the stringer and the skin. In the target application, it is filled with an adhesive material, but often it is filled with unidirectional tape or some other filler material [44]. The noodle regions exist due to manufacturing limitations that create "pockets" or voids at composite laminate intersections. These are filled up with a filler material to make sure that the intersections are geometrically stable and to remove stress concentrations at these points. Nevertheless, the noodle region forms the weakest link in the panel [44, 45].

Sápi et al. performed a study in [46], in which a numerical model was developed taking into account damage in the noodle region. A single stringer specimen in a pull-off configuration was considered, containing a noodle region filled with unidirectional prepreg material. Six node wedge elements were applied to the noodle region such that its sharp corners could be discretized as well. Furthermore, the mesh in the noodle region was double biased to allow for a more refined mesh near the noodle edges. The mesh in the radius of the stringer was then matched to the mesh at the noodle edges. Regarding intralaminar damage in the noodle region, matrix failure, fiber failure, fiber kinking and fiber splitting were accounted for in the model using the LaRC05 failure criterion. However, to take into account the increase in strength due to the constraining effect of adjacent, differently oriented plies, in situ strengths were considered in the failure criterion. Next to that, interlaminar damage near the noodle was also taken into account through the implementation of cohesive elements at the stringer ply interfaces, the skin-stringer interface, the skin-noodle interface and the stringer-noodle interfaces. From the results, the direction of the expected crack could be derived

by considering the direction of the maximum principle stress. In Figure 2.9, the critical locations at failure initiation can be observed. The pink arrow in the noodle region indicates the direction of the maximum principle stress. Since it is horizontal, it is expected that any crack in the noodle region will develop vertically, which is consistent with experimental observations.

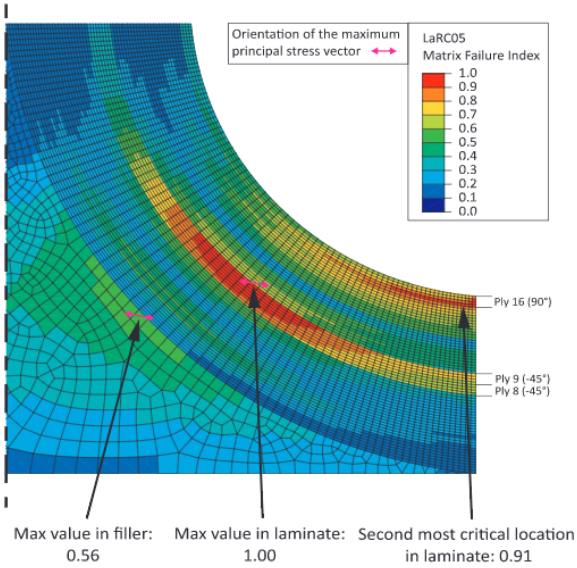

Figure 2.9: Failure index at failure initiation of the single blade-stringer specimen subjected to pull-off loading [46].

Kosztowny et al. [31], Leone et al. [24] and Action et al. [3] took into account the noodle in the model of a 7PB specimen, a SSCS and in a multistringer panel, respectively. In all of the models, the noodle region was meshed using continuum solid elements. In [3], Action et al. mentioned that the combined stiffness of the resin rich noodle, the interior wrap and the overwrap was taken into account in the solid elements by assigning it a "smeared orthotropic material property". None of the models allowed for the prediction of inter- or intralaminar damage at the noodle interfaces or within the noodle itself. However, Kosztowny et al. [31] suggested that the interlaminar damage at the skin-stringer interface *may* have been stopped by the noodle. It is also possible that the delamination propagated upwards in the noodle, but this was not taken into account by the model.

Ma et al. [47] did take into account damage propagation in the noodle region during the investigation of a single stringer specimen under pull-off loading. Plain strain continuum elements with reduced integration and hour glass control were used in the noodle regions. The mesh of the noodle region was fine, and even more refined near its ends, to ensure the accuracy of the results. X-FEM was used to predict the damage initiation and propagation inside the noodle region. Furthermore, the interfaces of the noodle with the stringer and skin were modelled using cohesive elements. To better understand the failure of the noodle region, the authors have performed a comparison between the numerically and experimentally obtained strain distributions in this area. The maximum principal strains just before damage initiated in the noodle region were obtained, see Figure 2.10.

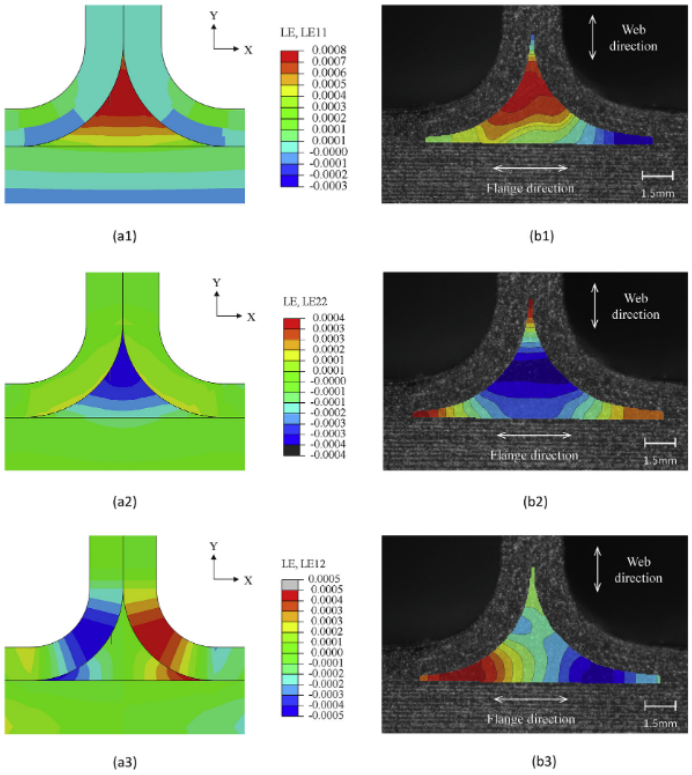

Figure 2.10: Maximum principle strain distribution of a single blade-stringer specimen under pull-off loading, just before damage initiation, in the noodle region: (a) numerically and (b) experimentally [47].

Several aspects could be noted from this figure. First of all, the crack within the noodle initiated at a location of maximum strain. Next to that, the noodle region contained large strain concentrations. Furthermore, there is an obvious discontinuity in strain between the noodle region and skin and stringer. According to the authors, this was the result of the stiffness mismatch between the skin, stringer and noodle region.

2.5 Cohesive Zone Method

Two main techniques exist to numerically model interlaminar damage: the Virtual Crack Closure Technique (VCCT) and the Cohesive Zone Method (CZM). The VCCT is based on the assumption that the strain energy released during crack growth is equal to the energy required to close that crack to its original length [17, 48, 49]. The VCCT can only predict crack growth, as it requires an initial delamination [17, 49]. In the CZM, it is assumed that a cohesive zone exists ahead of the crack tip of a crack in a certain material [50]. The cohesive zone can be defined as a region in which the material irreversibly degrades [51] due to micro-cracking, fiber bridging, small scale yielding, interaction of damage modes, etc. [52]. The cohesive zone can be numerically represented by zero or small thickness interface elements, called cohesive elements [50]. The behaviour of the cohesive elements is based on a traction-separation law, which relates stresses and displacements across an interface [50, 51, 53]. The

law dictates that the stress (or traction) across an interface increases until a maximum is reached, which corresponds to the interlaminar strength of the material. Then, the material starts to degrade: the stiffness decreases to zero, corresponding to complete separation of the interface faces [54, 55]. Numerically, this means that as the nodes of the cohesive elements separate, the material properties degrade until a complete loss of stiffness of the element is achieved when a critical opening displacement is reached and the nodes separate completely [50].

The most commonly used shape of the traction-separation law is bilinear [4, 49, 51], as it is the most computationally efficient and shows good numerical stability [55]. The bilinear traction-separation law shows an initial elastic linear region up until a peak stress, corresponding to the interface strength. Then, the material linearly degrades to zero, resulting in element failure [51], since no load can be carried by the material anymore [49]. The area underneath the curve corresponds to the critical fracture toughness of the interface [4, 49, 51, 53, 56]. The bilinear law for a mixed mode separation can be seen in Figure 2.11.

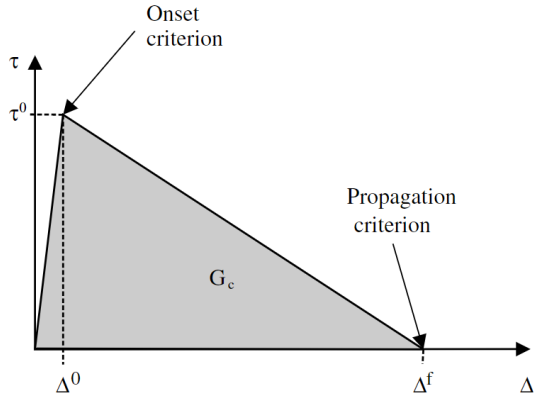

Figure 2.11: The bilinear traction-separation law for mixed mode separations [57].

A bilinear traction-separation law is characterized by three main parameters: the initial stiffness (or penalty stiffness), the interfacial strength and the critical fracture toughness associated with the mode [49, 57]. The interfacial strength corresponds to the interlaminar strength of the material: for shear modes, the interlaminar shear strength is used, while for normal modes, the interlaminar normal strength is used. It should be noted that it is assumed that compressive stresses do not cause opening of a crack. The area underneath the traction-separation curve corresponds to the respective interlaminar fracture toughness for each mode: G_{IC}, G_{IIC} and G_{IIIC} [49]. For mixed mode separations, the interaction of the different modes needs to be taken into account. In Figure 2.11, it can be seen that a distinction can be made between damage initiation and damage propagation. In the CZM, damage initiation is predicted using a strength-based failure criterion, while propagation is predicted through a fracture mechanics approach. A commonly used criterion for mixed mode damage initiation is the quadratic stress failure criterion [49, 57]:

$$\left(\frac{\langle \tau_I \rangle}{\tau_I^c}\right)^2 + \left(\frac{\tau_{II}}{\tau_{II}^c}\right)^2 + \left(\frac{\tau_{III}}{\tau_{III}^c}\right)^2 = 1 \tag{2.1}$$

In Equation 2.1, τ_I, τ_{II} and τ_{III} correspond to the normal and shear tractions, while τ_I^c, τ_{II}^c and τ_{III}^c correspond to the respective normal and shear interlaminar strengths [49, 57]. The Macauley brackets, $\langle\rangle$, indicate that only tensile normal tractions contribute to mode I opening [54].

Once this criterion is met, damage within the cohesive element initiates and the element starts to degrade. Once the element has completely failed, the crack propagates [51]. Damage within the cohesive element is represented by a scalar damage variable, d, that adopts a value between 0 and 1. The parameter has no physical meaning and is solely meant to represent damage growth within a cohesive element [50]. A value of 0 means that no damage has occurred within the cohesive element yet, while a value of 1 means that the cohesive element has failed (complete loss of stiffness) and separation has happened [55]. The traction-separation law can therefore be expressed in terms of the damage variable:

$$\tau = (1 - d)K\delta \tag{2.2}$$

In Equation 2.2, τ represents the traction across the interface, δ the opening displacement, K the initial or penalty stiffness and d the damage parameter. It can be seen that before the initiation criterion in Equation 2.1 is met, $d = 0$ and the separation is proportional to the traction through the penalty stiffness. After the criterion is met, $d > 0$ and the material of the cohesive element degrades [58].

Propagation predictions are related to the critical fracture toughness of the material. For mixed mode separations, a commonly used criterion to predict propagation is the Benzeggagh-Kenane criterion (the B-K criterion), which takes into account the mode mixity ratio [49], see Equation 2.3. The criterion is widely accepted to use for epoxy and PEEK composites [57].

$$G_{IC} + (G_{IIC} - G_{IC})\Big(\frac{G_{shear}}{G_T}\Big)^{\eta} = G_C \tag{2.3}$$

Here, G_{IC}, G_{IIC} and G_{IIIC} correspond to the pure mode fracture toughness values for mode I, mode II and mode III respectively. Furthermore, $G_{shear} = G_{II} + G_{III}$ and $G_T = G_I + G_{shear}$. Next to that, η is the B-K exponent and is derived from MMB tests with different mode-mixity ratios and is thus material dependent [49]. Once the strain energy release rate at the delamination front exceeds the critical strain energy release rate, G_C, depicted in Equation 2.3, the delamination propagates [57].

The incorporation of the CZM in Abaqus comes with some challenges. Often, numerical issues related to the penalty stiffness, mesh refinements and convergence due to the softening nature of the CZM occur [53]. To ensure accurate numerical results, a sufficient amount of cohesive elements need to be present in the cohesive zone, such that the stress distribution ahead of the crack tip can be accurately captured [51, 53]. To determine the required mesh size to do so, accurate values for the cohesive zone length and the minimum number of cohesive elements required in the cohesive zone are needed [51]. The mesh size can then be calculated using the following formula [53]:

$$l_e = \frac{l_{CZ}}{N} \tag{2.4}$$

In Equation 2.4, l_e is the mesh size in the crack direction, l_{CZ} is the cohesive zone length and N is the minimum required number of elements in the cohesive zone. Several analytical formulas exist to calculate the cohesive zone length, but these tend to overpredict the numerical cohesive zone length. Therefore, mesh convergence analyses should be performed to predict the cohesive zone length. For the minimum number of cohesive elements in the cohesive zone, Harper and Hallett have proposed at least two or three elements [51], which was confirmed by Yetman et al. [10], Kolanu et al. [16] and Farohki et al. [23].

2.6 Research Objective

Based on the literature gathered in the previous sections, a research objective for this thesis project can be set up.

The research objective of the thesis project is:

> "To develop a numerical tool that is able to capture skin-stringer separation at critical locations of a specific composite multistringer panel in compression by means of a transversely loaded single stringer specimen in a seven point bending or four point twisting configuration".

To do so, the following sub-objectives need to be achieved:

- The critical locations of the considered panel need to be determined.
- The separation modes corresponding to the critical locations need to be identified.
- The single stringer specimens should be sized and loaded accordingly, such that the out-of-plane displacements of the specimens mimic the out-of-plane displacements of the corresponding critical locations.
- A methodology to numerically model the skin-stringer separation in the single stringer specimens needs to be developed, taking into account the tape/fabric interface and noodle regions.

Chapter 3

Methodology

Considering the research objective set up in chapter 2, a numerical tool is to be developed to study skin-stringer separation in a composite stiffened panel. Due to the large computational and manufacturing expenses associated with simulating and validating the damage behaviour of a multistringer panel, single stringer specimens should be developed that bridge the gap between the multistringer panel and coupon specimens. The behaviour of the single stringer specimens should be representative of the behaviour of the multistringer panel at locations where skin-stringer separation is expected to occur. This way, damage in the multistringer panel can be modelled on a smaller, less computationally expensive scale. In this chapter, first, the composite stiffened panel used for this thesis project is described. Then, the methodology to achieve the research objective is elaborated upon.

3.1 Description of the Composite Stiffened Panel

The panel discussed in this thesis project is a composite stiffened multistringer panel, that is used in the NASA Advanced Composite Project. The panel consists of a skin and four hat stringers, that are co-cured together. It has a length of 749.30 mm and a width of 769.62 mm. The stringers are placed onto the skin, such that the central bay is slightly larger than the outer bays. Specifically, the central bay is 108.20 mm wide, while the outer bays are 103.12 mm wide. A pad-up region is added to the skin at the top and bottom of the panel. This way, the "free" length of the panel is 490.22 mm long. The pad-up region is added to avoid failure near the edges. Furthermore, potting is added to the top and bottom edge of the panel to allow for a uniform load application [1, 3, 24, 28, 31]. The multistringer panel can be seen in Figure 3.1. In Subfigure 3.1(a), the panel including the potting at its ends is shown, while in Subfigure 3.1(b), the relevant dimensions are shown.

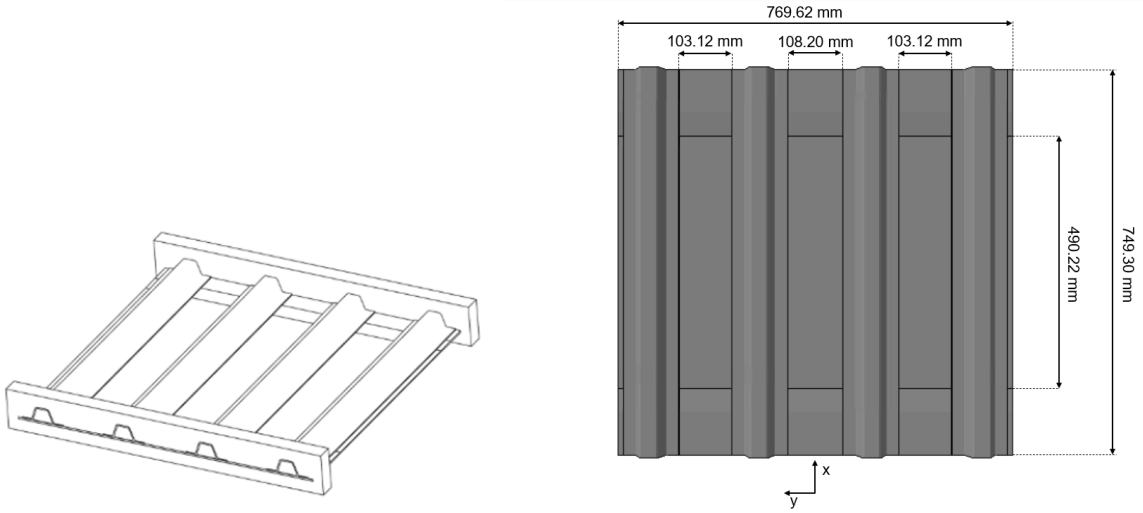

(a) The composite stiffened panel with potting at its ends [3].

(b) Dimensions of the multistringer panel and its bays.

Figure 3.1: The composite stiffened multistringer panel considered for this thesis project.

The stringers contain three distinct regions: the interior wrap, the overwrap and the noodle regions. The overwrap folds over the interior wrap and extends further outwards to form the stringer flanges. This way, the webs and the crown of the stringer are a combination of the interior wrap and overwrap. At the intersection of the interior wrap, overwrap and skin, a resin-filled pocket is created, which is referred to here as the noodle region. The width of a single stringer is 108.5 mm and it extends over the entire length of the panel. The different regions of a single stringer and its relevant dimension are shown in Figure 3.2.

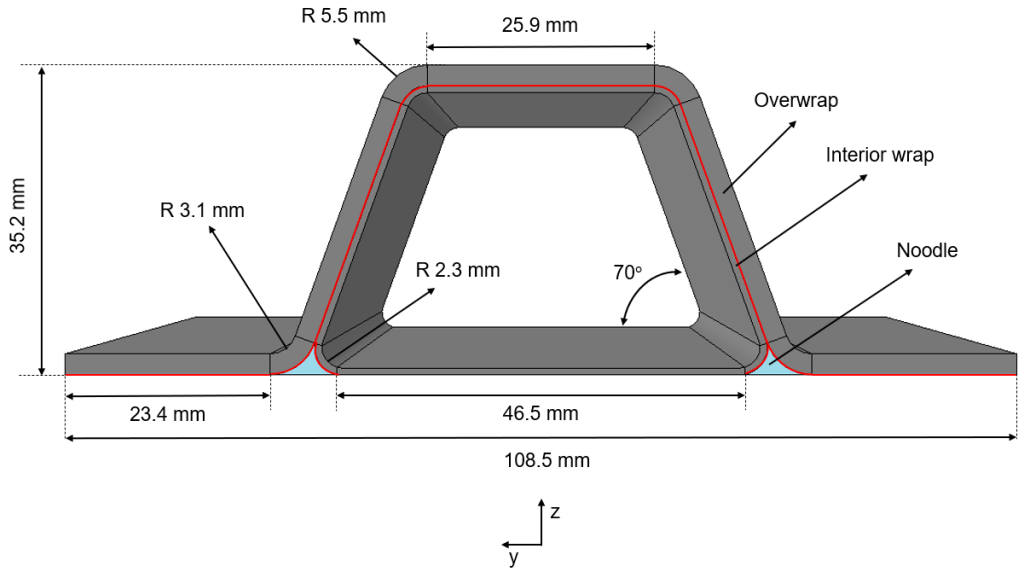

Figure 3.2: Cross-sectional view of the stringer showing the different parts of the stringer and the relevant dimensions.

The skin of the multistringer panel contains 12 plies of IM7/8552 tape material, stacked in a quasi-isotropic, symmetric and balanced layup: $[-45/+45/0/90/-45/+45]_s$. Next to that, the interior wrap is made of IM7/8552 plain weave fabric material, containing four plies in the following layup: $[+45/-45/0/+45]$ (inwards to outwards). The overwrap is made out of the same material and contains 12 plies stacked as follows: $[+45/-45/0/+45/+45/0/-45/+45/+45/-45/0/+45]$ (inwards to outwards). This way, the webs and the crown of the stringer contain 16 plies in a balanced and quasi-isotropic layup: $[+45/-45/0/+45/+45/-45/0/+45/+45/0/-45/+45/+45/-45/0/+45]$. It should be noted that the direction in which the 0 degree plies are oriented is parallel to the length of the specimen (in the x-direction). Finally, the noodle region is filled with an adhesive. All of this can be visualized in Figure 3.3.

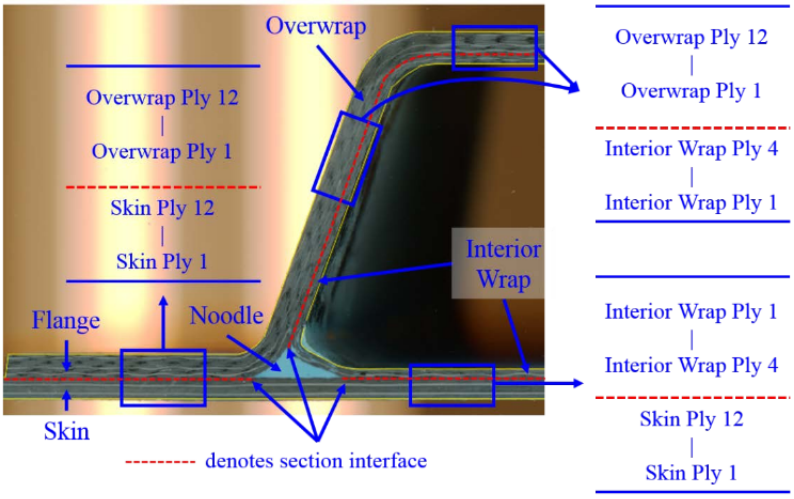

Figure 3.3: Cross-sectional view of the stringer specifying the layup of the different parts [31].

The lamina properties for the tape and fabric material used in the skin and stringer respectively, are reported in Table 3.1.

Table 3.1: Lamina properties of IM7/8552 tape and IM7/8552 fabric material [31].

	E_{11} [GPa]	E_{22} [GPa]	ν_{12} [-]	G_{12} [GPa]	G_{13} [GPa]	G_{23} [GPa]	t_{ply} [mm]
Tape	146.76	8.68	0.32	5.16	5.16	3.00	0.18
Fabric	65.99	65.79	0.052	5.08	3.39	3.39	0.20

3.2 Methodology

The methodology on how the research objective is achieved, is briefly described here and is described in more detail in the next chapters.

As shown in section 3.1, the composite stiffened panel that is considered in this thesis project is quite complicated and contains some very specific characteristics, such as the tape/fabric interfaces between the skin and the stringers and the noodle regions at the skin-stringer intersection. Implementing these in a numerical model is challenging. Therefore, a generic 7PB specimen of the considered panel is modelled in Abaqus and verified, to understand how the different parts of the panel should be modelled. Next, some preliminary analyses are performed on this 7PB specimen to determine its sensitivity to different modelling parameters, such as the mesh size and the applied cohesive law, on the predicted results.

Then, the multistringer panel in compression is modelled in Abaqus, using what was learnt during the preliminary analyses on the generic 7PB specimen. The model is verified and linear and non-linear buckling analyses are performed to understand the (post-)buckling behaviour of the panel. In this model, the panel is rather coarsely meshed and no damage has been included. This is because this model is only used to determine the post-buckling deformations of the panel and to determine the critical locations in the panel based on the post-buckling deformations, where skin-stringer separation is expected to occur.

Then, the critical locations on the multistringer panel are identified and verified. Two types of locations are distinguished. At the location where the skin pulls away from the stringer, a mode I dominated skin-stringer separation is expected to occur. Next to that, at the location where the skin twists with respect to the stringer, skin-stringer separation in a combined mode II and mode III can occur. Based on these locations and the deformation of the skin in the multistringer panel near the critical locations, a critical region and consequently a single stringer specimen are sized to represent this critical region. For the location where a mode I dominated skin-stringer separation is expected to occur, a 7PB specimen is designed. For the location where a mode II and mode III skin-stringer separation is expected to occur, a 4PT specimen is designed. The position of the loading and supporting points for each of these specimens is determined by comparing the out-of-plane displacements of the skin in the critical region of the multistringer panel, to the out-of-plane displacements of the skin in the single stringer specimen. By minimizing the shape error between these two, an optimal loading configuration can be determined.

Finally, detailed analyses are performed on the 7PB specimen and the 4PT specimen. In these analyses, damage models based on the cohesive zone method are incorporated that aim to capture skin-stringer separation. Both the damage initiation, as well as the damage propagation in the specimens is modelled and the results are discussed. To verify whether they are indeed representative for the multistringer panel, a damage model for the multistringer panel is developed as well. The results of the single stringer specimens are then compared to the results of the multistringer panel as a means of verification.

An overview of the methodology can be seen in Figure 3.4. In this flowchart, the rectangular boxes represent analyses, while the parallelograms are outputs of the specific analyses.

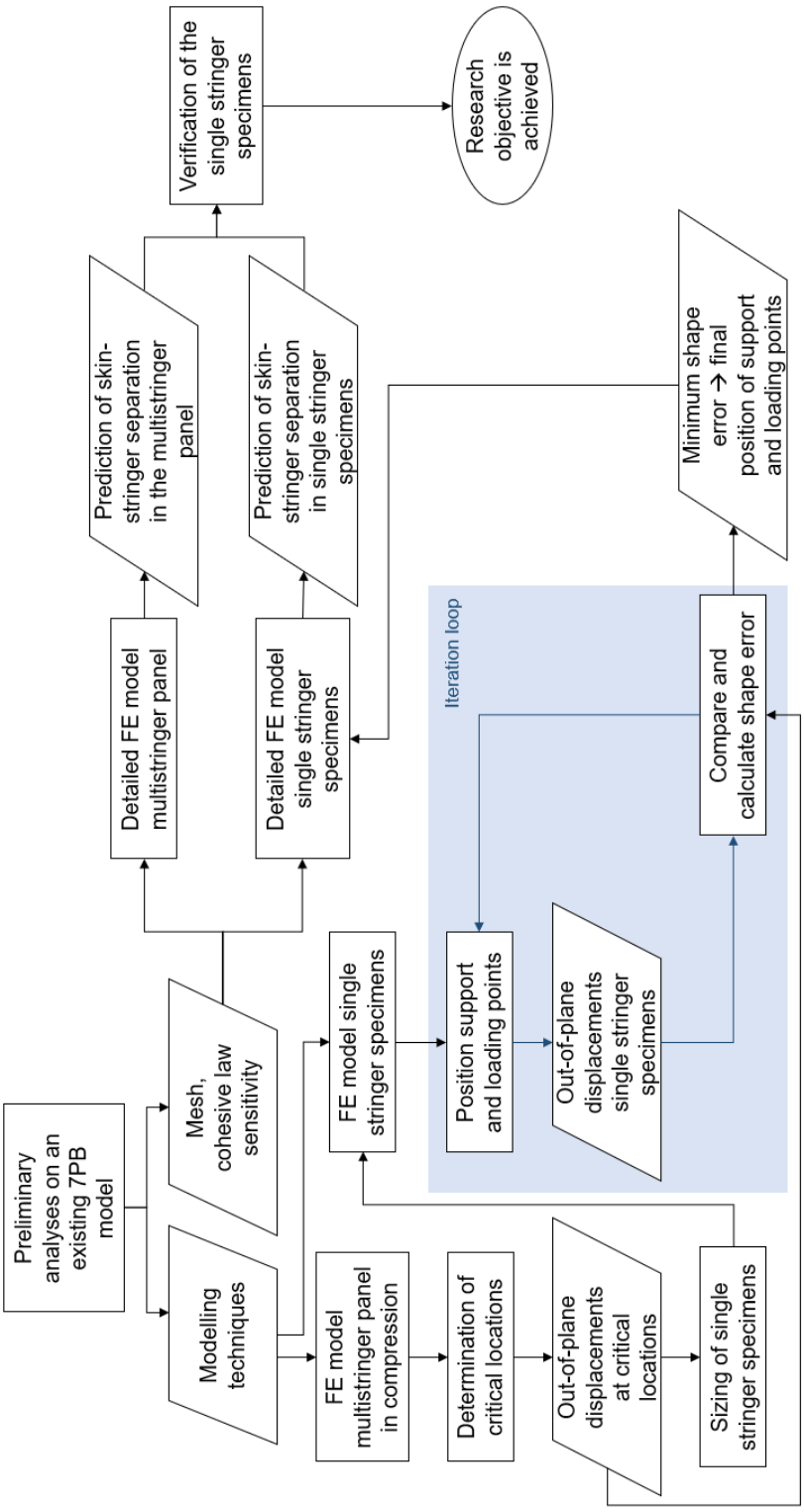

Figure 3.4: Overview of the methodology used to achieve the research objective.

Chapter 4

Preliminary Analyses of a Seven Point Bending Model

To study how to model the composite stiffened panel and its characteristics, a 7PB specimen with the same panel characteristics as the target application is modelled and verified with an existing model [31]. The model is created in Abaqus and is referred to here as the *baseline model*. After having verified the baseline model, some sensitivity studies are performed to identify the influence of three different variables: the mesh, the initial imperfections caused by a thermal analysis and the applied cohesive law.

4.1 Set Up of the Baseline Model

In this section, the procedure of how the baseline model is created, is discussed.

4.1.1 Geometry

The 7PB specimen is built up out of different parts. It consists of a skin and a single stringer. The stringer is as described in section 3.1. The skin has a square shape with a length and width equal to 254 mm. The stringer spans the entire length of the skin, resulting in a stringer length also equal to 254 mm. The width of the stringer is 108.5 mm and the stringer is positioned exactly in the middle of the skin. A top view of the skin-stringer assembly can be seen in Figure 4.1.

As mentioned in section 3.1, the skin is made out of a tape material, while the stringer is made out of a fabric material. The lamina properties for each can be found in Table 3.1. The noodle regions at the intersection of the skin and stringer are filled with an adhesive.

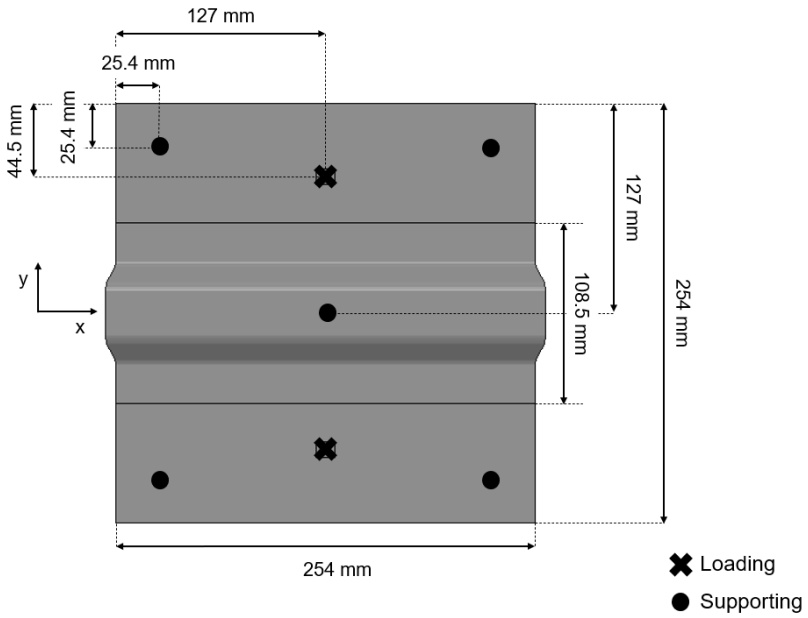

Figure 4.1: Top view of the 7PB specimen showing relevant dimensions.

Seven indenters are used to enforce the deformation onto the specimen. Five of these are located on the skin side of the specimen and remain stationary, while the other two indenters introduce the load on the stringer side of the specimen. A cross-sectional view of the assembly can be seen in Figure 4.2. Metallic shims are placed on the skin at locations where the top indenters apply the load. This is to ensure that no damage is created there due to the load introduction and to distribute the stress concentration underneath the top indenters.

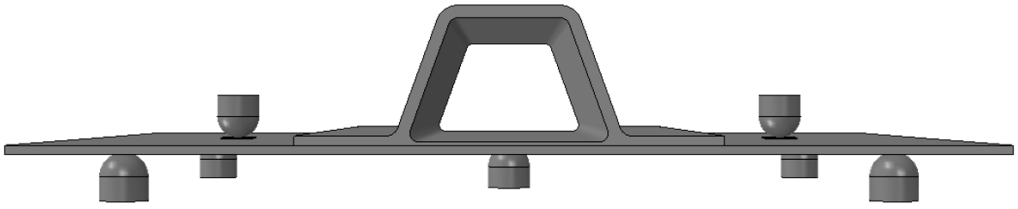

Figure 4.2: Cross-sectional view of the 7PB specimen.

The two top indenters are placed central along the length of the specimen (along the x-direction) and 44.5 mm from the skin edge along the y-direction. The central bottom indenter is positioned exactly in the center of the skin; 127 mm from every edge. Finally, the remaining four bottom indenters are placed symmetrically in each corner, namely 25.4 mm from the nearest skin edges. The locations of the indenters are specified in Figure 4.1.

4.1.2 Finite Element Model

A finite element model is created that aims to simulate the behaviour of the specimen in the 7PB configuration. To do so, the different parts of the specimen are meshed, a material definition is assigned to all the elements, interactions and constraints associated with the load application are specified and finally, the model is submitted for analysis.

Mesh

The mesh of the stringer is refined in two directions. First of all, the mesh becomes more refined towards the center of the stringer along its length. This way, the elements in the middle of the stringer have an aspect ratio of approximately equal to one. Elements with an aspect ratio closer to one produce more accurate results, as the variation in output variable along a single element is minimized. When the aspect ratio is larger, the accuracy may be less due to interpolation errors [59]. In the 7PB configuration, it is expected that damage will initiate at the location along the stringer length where the skin buckles away from the stringer. In this case, this location corresponds to the center of the stringer, since a symmetric shape is enforced onto the specimen by the indenters. Therefore, the mesh is refined such that in the central portion of the specimen, the aspect ratio of the elements is approximately equal to one. The outer portions of the stringer are less important for damage initiation and propagation and can therefore be more coarsely meshed. The mesh is refined gradually from the coarser mesh at the stringer ends to the finer mesh at the central part. Looking at Figure 4.3, this means that in the parts indicated with the letter *A*, the mesh is relatively coarse. The mesh becomes sequentially more refined in the parts indicated by *B* and *C*, until the elements have an aspect ratio approximately equal to one in the part indicated by *D*, which corresponds to the central part of the stringer.

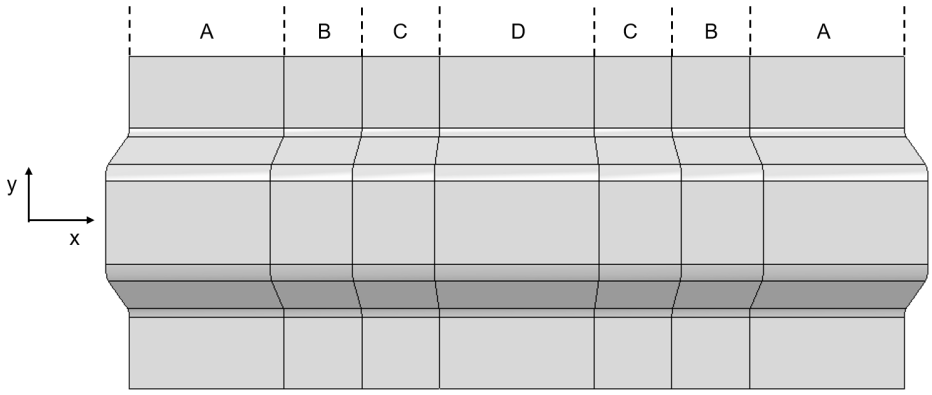

Figure 4.3: Regions of the stringer with different mesh sizes.

Furthermore, the stringer is refined in the transverse direction (along y) as well. More specifically, the flanges are refined along the y-direction, to ensure a sufficient amount of cohesive elements in the cohesive zone ahead of the crack tip and consequently, to ensure accurate damage initiation and propagation predictions. The element size in the y-direction of the flange is equal to 0.24 mm. An overview of the mesh size in each region of the stringer shown in Figure 4.3, can be seen in Table 4.1.

Table 4.1: Mesh sizes along the stringer length in the baseline model.

Region	Length [mm]	Element size along y [mm]	Element size along x [mm]	Aspect ratio [-]
Region A	50.8	0.24	2.54	10.6
Region B	25.4	0.24	1.02	4.3
Region C	25.4	0.24	0.51	2.1
Region D	50.8	0.24	0.26	1.1

The mesh of the skin matches with the mesh of the stringer in the regions where the two overlap. The remainder of the skin is more coarsely meshed along the y-direction. An element size of 2.6 mm at the skin edges is used, which gradually decreases to 0.24 mm underneath the flanges. Furthermore, the parts of the skin directly underneath the top indenters are finely meshed and match the mesh of the shims. This is to reduce the stress concentration directly underneath the indenters and to redistribute the stress to the rest of the specimen. Finally, two elements are used through the skin thickness, as opposed to the stringer, where only one element is used. Between the skin and stringer, underneath the flanges, a cohesive strip is inserted. This strip has the dimensions of the flanges and has a very small thickness of 10^{-5} mm. This way, a zero-thickness cohesive layer is approximated. The cohesive strips cover the regions *B, C* and *D*, shown in Figure 4.3, and are meshed to match with the skin and stringer. The mesh size requirements for the cohesive layer are critical. A finely meshed cohesive layer is necessary to ensure that the stress distribution ahead of the crack tip is accurately captured [51, 53]. The mesh of the cohesive layer therefore dictates the mesh of the skin and stringer.

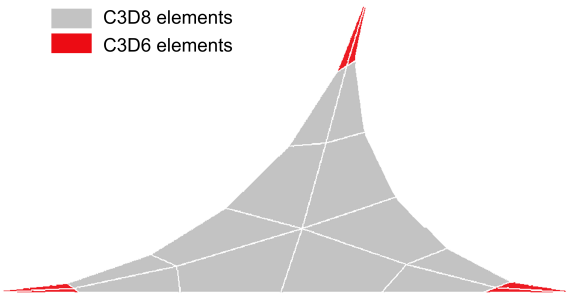

Figure 4.4: Mesh of the noodle in the baseline model, showing the distinction between C3D6 and C3D8 elements.

The skin, interior wrap and overwrap have been meshed using continuum shell elements (SC8R), while the noodle region is meshed with hexahedral solid elements (C3D8) and wedge solid elements (C3D6) in the noodle corners. This can be seen in Figure 4.4, where the elements indicated in red are C3D6 elements and the elements indicated in grey are C3D8 elements. C3D8 elements are used in the majority of the noodle as these are computationally efficient elements. C3D6 elements on the other hand require very fine meshes to produce accurate results and should therefore only be used to complete a mesh. For example in this case, if C3D8 elements would be used in the sharp corners of the noodle region, the mesh would be distorted there, which could lead to poor results. Therefore, C3D6 elements are used in the corners [59]. Next to that, the shims are meshed using reduced integration hexahedral solid elements (C3D8R). Finally, the cohesive strips are meshed using hexahedral three-dimensional cohesive elements (COH3D8). An overview of the elements used in the different parts of the baseline model can be seen in Table 4.2.

Table 4.2: Element types used in different parts of the baseline model.

	Element type
Interior wrap	SC8R
Overwrap	SC8R
Skin	SC8R
Noodle regions	C3D8 & C3D6
Cohesive strips	COH3D8
Shims	C3D8R

An overview of the final mesh of the baseline model can be seen in Figure 4.5.

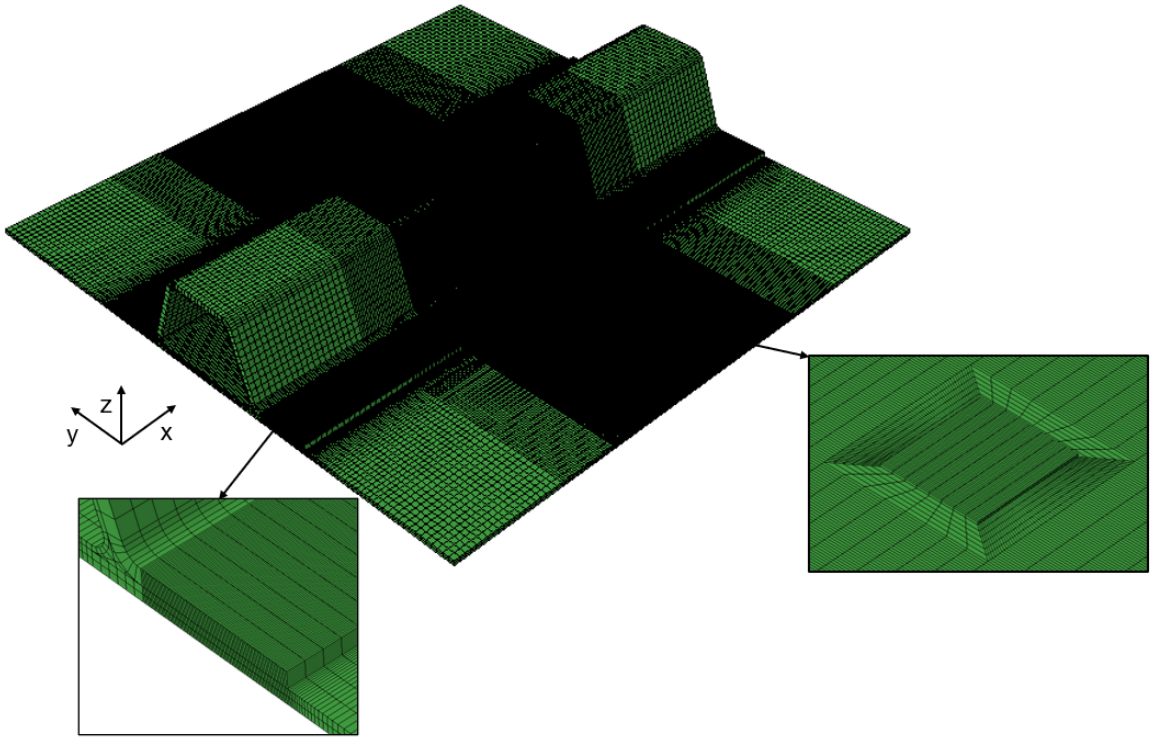

Figure 4.5: Mesh of the 7PB specimen in the baseline model.

Material Definition

For the composite parts of the 7PB specimen, the layup specified in section 3.1 for each of the parts is created in Abaqus and assigned to the SC8R elements belonging to that part. The properties used for the individual tape and fabric plies can be seen in Table 3.1.

A trilinear cohesive law is assigned to the cohesive strips. This trilinear law is achieved by superposing two bilinear cohesive laws. The properties applied in the first cohesive law are referred to as the cohesive base properties. The properties used in the second bilinear cohesive law are the tape/fabric bridging properties. By superposing the two laws, the R-curve effect at the skin-stringer interface can be taken into account. The superposition of

the cohesive laws is explained in more detail in section 2.3 of chapter 2. The properties for both cohesive laws used in the baseline model can be seen in Table 4.3. The cohesive base properties in this table are obtained through standardized characterization tests using specimens containing all tape plies with the same ply orientation. The tape/fabric bridging properties are obtained as follows; the values for the fracture toughness are determined by taking the difference between the steady-state values of the fracture toughness for standard tape/tape interfaces and non-standard tape/fabric interfaces. These last values are obtained from characterization tests with specimens containing a mixture of tape and fabric plies. The B-K exponent is determined such that the obtained fracture toughness values match with the experimental outcomes of the MMB test. Next, the interlaminar strength values for the tape/fabric bridging law are determined through trial and error such that the numerically obtained load-displacement curve fits the experimentally obtained load-displacement curve. Finally, the values for the penalty stiffness are calculated by ensuring that the opening displacement at which the cohesive elements start to degrade matches with the cohesive base [15].

Table 4.3: Properties for the cohesive base and superposed tape/fabric bridging law used in the baseline model [31].

	K_I [N/m^3]	K_{II} [N/m^3]	G_{Ic} [kJ/m^2]	G_{IIc} [kJ/m^2]	σ_c [MPa]	τ_{IIc} [MPa]	η_{BK} [-]
Cohesive base	$4.89e^{13}$	$3.53e^{13}$	0.240	0.739	62.29	92.95	2.07
Tape/fabric bridging	$5.43e^{12}$	$8.14e^{12}$	0.350	2.102	6.89	20.67	3

The superposition of the two bilinear cohesive laws is numerically achieved by duplicating the layer of cohesive elements, such that a new layer is created which shares nodes with the original layer. The first bilinear law, using the cohesive base properties shown in Table 4.3, is assigned to the original layer of elements. The second bilinear law, using the tape/fabric bridging properties shown in Table 4.3, is applied to the duplicated layer.

The cohesive law is said to be a traction-separation law, which relates stresses and opening displacements across an interface [50, 51, 53]. In traction-separation laws, a distinction can be made between damage initiation and damage propagation. In the baseline model, the damage initiation is predicted using a strength-based failure criterion, namely the quadratic stress failure criterion, see Equation 2.1. It is assumed that $\tau_{IIc} = \tau_{IIIc}$. The damage propagation is predicted using the critical fracture toughness of the interface material. The mixed mode Benzeggagh-Kenane criterion (or B-K criterion) is used, see Equation 2.3. It is assumed that $G_{IIc} = G_{IIIc}$. Next to that, $G_{shear} = G_{II} + G_{III}$ and $G_T = G_I + G_{shear}$.

The noodle regions and the metallic shims are assigned elastic isotropic materials. The material properties of the epoxy used in the noodle regions and of the metal used for the shims can be seen in Table 4.4.

Table 4.4: Epoxy and shim properties used in the baseline model.

	E [GPa]	ν [-]
Epoxy	3.1	0.4
Shim material	68.9	0.3

Contact and Constraints

All parts are assembled in a 7PB configuration as shown in Figure 4.1. The indenters are built as rigid surfaces and are positioned as described in subsection 4.1.1. Spring elements are placed between the indenters and the skin node directly underneath the indenters. Or in case of the top indenters, the spring element is placed between the top indenters and the node on the shim directly underneath. The spring elements are constrained to the out-of-plane degree of freedom (along the z-direction) and are assigned a spring stiffness of 1 N/mm. This ensures that during the analyses, the skin stays in contact with the indenters. The spring stiffness is so small that the accuracy of the results is not affected. Next to that, a surface-to-surface contact interaction is defined between the indenters and the skin or shims. A friction coefficient of 0.333 is defined in the interaction to take into account the fact that surfaces in contact transmit both shear and normal forces that usually are related. Furthermore, small sliding is defined for the contact pairs to limit the computational cost. In the contact pairs, the indenters are defined as the master surfaces, while the skin or shims are defined as the slave surfaces.

Next to that, several tie constraints are defined between the different parts. First of all, the cohesive strips are tied to both the skin and stringer. In these constraints, the cohesive surfaces are defined as slave surfaces. As a default, the part with the finest mesh, or if the mesh size of the tied surfaces matches, the part with the softest material is selected as the slave surface. This is to avoid interpenetration, since in any constraint or contact pair, the nodes on the slave surface cannot penetrate the master surface, but the nodes on the master surface are able to penetrate the slave surface [59]. The central part of the stringer (the noodle and the interior wrap) is tied directly to the skin. Furthermore, at the edges of the specimen (denoted by A in Figure 4.3), the skin and stringer are also directly tied to each other. It should be noted that due to the non-zero thickness of the cohesive strips, a gap of 10^{-5} mm is present between the skin and stringer, so the position tolerance criterion in the tie constraint is adjusted to 10^{-4} mm. This way, the slave nodes that lie within this tolerance are moved towards the master surface, such that the gap is bridged without causing any strains [59]. Finally, the shims are tied to the skin.

Analyses

A thermal step is included to simulate the effect of cool-down after curing. During this non-linear static step, no loads are introduced, but the temperature of all the nodes is lowered from 160^{o}C to 0^{o}C. The indenters are constrained in all directions, except for translation along the z-direction and are kept in contact with the skin through the spring elements.

After the thermal step, all of the indenters are kept fixed at their final position. The bottom indenters are constrained in all directions, while the top indenters are left free for translation along the z-direction. During a subsequent non-linear dynamic implicit step, a downward displacement of 10 mm is applied to the top indenters at a rate of 25 mm/s.

4.2 Verification of the Baseline Model

In order to verify the baseline model, its results are compared to the results obtained in [31]. The comparison is made in terms of the load-displacement curve, the displacement at which damage initiates and the damage propagation at similar displacements.

The load-displacement curves can be seen in Figure 4.6. From the graph, it can be seen that the curves match very well. The differences between the curves can be attributed to small differences in the stringer geometry and mesh, but also to differences in material input parameters due to the conversion of some properties from US units to SI units.

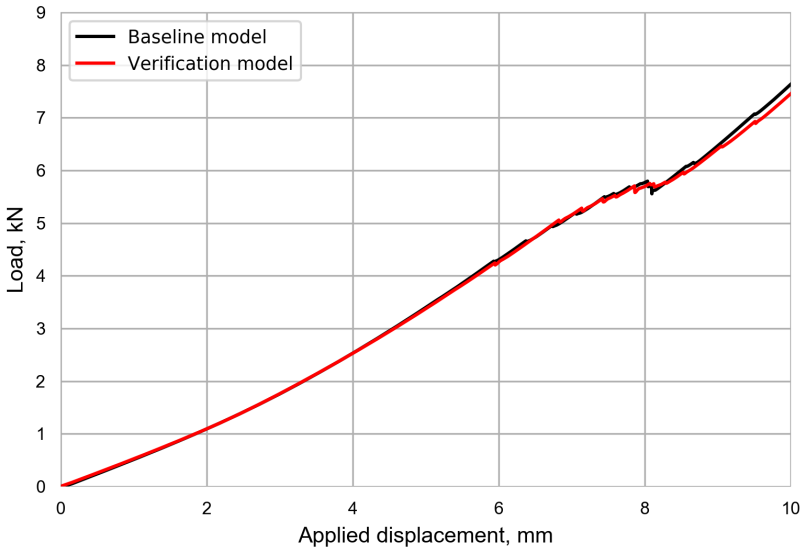

Figure 4.6: Comparison of the load-displacement curves of the baseline model and the verification model.

In Table 4.5, the average displacement of the top indenters at which damage initiates is given for each of the models.

The displacement is defined as the downward displacement after the thermal analysis. Furthermore, damage initiation is defined as the point at which a cohesive element has completely failed according to the applied cohesive law. This is the displacement at which the damage variable, d, is equal to one for the first time. The damage variable determines by how much the initial stiffness of an element has degraded. It is a scalar variable and adopts values between 0 and 1. When $d = 0$, no damage has occurred in the element, while when $d = 1$, the element has lost its stiffness and has completely failed [55]. In this analysis, the displacement at which $d = 1$ for the first time is determined using linear extrapolation methods. Figure 4.7 illustrates why this is justified and needed here. It should be noted that the damage variable in Abaqus is indicated by 'SDEG'.

Table 4.5: Comparison of the applied displacement at which damage initiates in the baseline model and the verification model.

	Displacement [mm]
Baseline model	3.48
Verification model	3.50
Relative difference	-0.6%

To reduce the computational expenses of the model, the damage variable is requested at every 0.5 mm of applied displacement, instead of at every increment. The black curve in Figure 4.7 shows the damage variable of one of the first failing elements in the baseline model, in function of applied displacement . Here, x_0, x_1 and x_2 are three consecutive applied displacement values for which the damage variable is requested. It can be seen that the damage variable increases from 0 to 1 and stays constant after $d = 1$ has been reached. For x_0 and x_1, $d < 1$, so damage initiation has not occurred yet. For an applied displacement of x_2, $d = 1$. However, it is unlikely that $d = 1$ for the first time at an applied displacement of exactly x_2. Probably, $d = 1$ for the first time somewhere between x_1 and x_2 and due to the rather coarse discretization at which the damage variable is requested, the applied displacement x at which the damage variable actually becomes 1 for the first time is missed. Therefore, taking the value of x_2 as the displacement at which damage initiates would be an overprediction. The actual displacement at which damage initiates is x, shown with the red dotted line in Figure 4.7. When plotting a linear curve through (x_0, y_0) and (x_1, y_1) (shown in red in Figure 4.7) and comparing it to the curve obtained from the baseline model, it can be seen that the relation between the damage variable for one of the first failing elements and the applied displacement, is more or less linear. Therefore, the displacement x at which damage initiates can be obtained through lin-

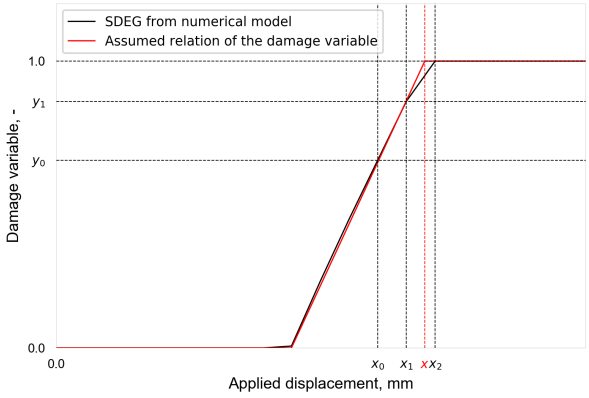

Figure 4.7: Curve showing the relation between the damage variable of one of the first failing cohesive elements in the baseline model and the applied displacement, to justify the use of linear extrapolation to obtain the displacement at which damage initiates.

ear extrapolation. It should be kept in mind however, that the relation between the damage variable of an element and the applied displacement is most likely not entirely linear and that the obtained displacements shown in Table 4.5 are thus approximations. Nevertheless, it can be observed that the displacements at which damage initiates match very well between the models.

Finally, in Figure 4.8, the damage at similar displacements for each of the models can be seen. This way, the damage propagation and its rate can be compared. From the figure, it becomes clear that the damage at similar applied displacements matches very well between the models.

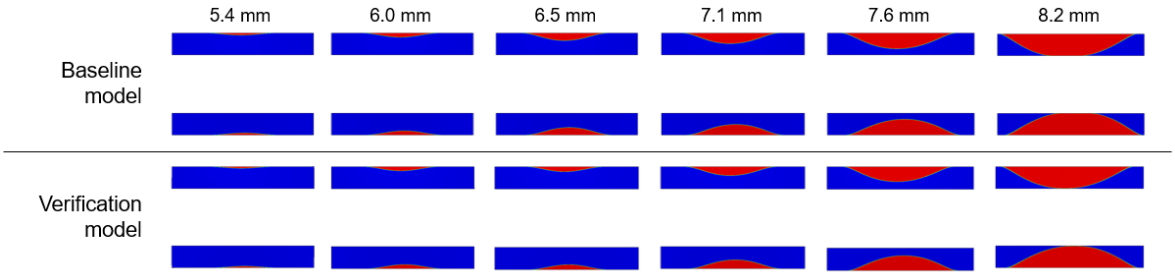

Figure 4.8: Comparison of the damage at similar displacements of the baseline model and the verification model.

From these comparisons, it can be concluded that the baseline model has been verified and that the geometry developed in this model can be used in the remainder of this research.

4.3 Sensitivity Analyses on the Baseline Model

In order to understand the influence of different parameters on the predictions of the baseline model, three sensitivity studies have been performed. A mesh sensitivity analysis is done to compare the influence of the mesh size, a thermal step analysis is done to evaluate the effect of the temperature on the resulting geometric imperfections and their results on the prediction accuracy. Finally, a sensitivity analysis is done on the cohesive law; three different cohesive laws are used and the differences between them are evaluated. The results of the different models are compared to the now verified baseline model.

4.3.1 Mesh Sensitivity Analysis

In order to evaluate the effect of the mesh size on the predictions and on the computational time required to complete the analysis, the mesh size is increased. This is done such that in every region defined in subsection 4.3.1 (Figure 4.3), the mesh size is twice the mesh size of the baseline model. The way of refinement towards the center of the specimen and underneath the flanges is kept the same as in the baseline model. This way, the aspect ratio of the elements in every region is kept the same as in the baseline model and the results are not affected by poor element quality. Furthermore, only one element is used through the skin thickness, as opposed to two elements in the baseline model. Everything else is also kept the same: the

same cohesive law is applied and a thermal step in which the temperature of the nodes is decreased by 160^{o}C is applied as well.

Table 4.6 shows the mesh size for the baseline model and the coarser model in conjunction with the regions defined in Figure 4.3. Furthermore, the total number of elements of the two models is shown.

Table 4.6: Comparison of the mesh size in every region of the stringer of the baseline model and a coarser model.

Region	Element size y x x baseline model [mm x mm]	Element size y x x coarse model [mm x mm]	Relative difference
Region A	0.24 x 2.54	0.48 x 5.08	-
Region B	0.24 x 1.02	0.48 x 1.95	-
Region C	0.24 x 0.51	0.48 x 1.02	-
Region D	0.24 x 0.26	0.48 x 0.51	-
Total elements	580270	97512	-83.2%

A comparison is made between the baseline model and the coarser model in terms of the load-displacement curve, damage initiation and propagation and the total CPU time, as the mesh directly influences the computational time required to complete the analysis.

First of all, a comparison is made in terms of the total CPU time. For both models, 20 CPUs are used to run the analysis. The total CPU time for each of the models can be seen in Table 4.7. The following CPUs were used: Intel(R) Xeon(R) CPU E5-2660v3.

Table 4.7: Comparison of the total CPU time required to complete the analysis for the baseline model and a coarser version of the baseline model.

	Total CPU [hrs]
Baseline model	756.69
Coarse model	723.64
Relative difference	-4.4%

It can be seen that the difference in CPU time is small, which is surprising considering that the difference in total number of elements is large. This is because the coarse model needs more increments to reach convergence. One on hand, this increase in number of increments can be explained by the contact formulation between the indenters and the skin/shims. The contact between these is defined as surface-to-surface contact. This means that the contact between the surfaces is enforced by averaging between the slave nodes; when the indenter comes into contact with the skin/shims, the penetration of the master surfaces (indenter) into the slave surface (skin/shims) is not only resisted at the nodes, but is resisted in between the nodes as well. This way, when using surface-to-surface contact, it is unlikely for large penetrations to occur. Nevertheless, some penetration of the indenter into the skin/shims may still occur, especially when the mesh is coarse, since less slave nodes are then involved in resisting the

penetration. During the analysis, for every increment, it is checked whether the penetration exceeds a certain thresh hold. If this is the case, the increment is abandoned and the solution is re-iterated with a smaller increment size [59]. It becomes clear that in this case, due to the coarser mesh of the slave surfaces (skin/shims), smaller increments were required to satisfy the penetration criterion. This is directly related to the increased number of increments for the coarser model (1611 increments vs. 175 increments) and an increase in CPU time. On the other hand, with the cohesive elements being larger, convergence may also be more difficult to reach. When a coarser mesh is used, there are fewer cohesive elements in the cohesive zone. Since the damage initiation and propagation are such localized phenomena, convergence and accuracy difficulties may arise because of the large transitions in stress at the crack tip that are difficult to be solved for with larger cohesive elements. Ahead of the crack tip, there is a cohesive zone. The length of the cohesive zone is equal to the distance measured from the crack tip to a point ahead of the crack tip where the maximum stress is reached [53]. This can be seen in Figure 4.9. A sufficient amount of cohesive elements needs to be present in the cohesive zone to ensure that the non-linear stress distribution ahead of the crack tip is accurately captured. In Subfigure 4.9(a), it can be seen that enough elements are present in the cohesive zone length to capture this stress state. However, in Subfigure 4.9(b), an example is shown where not enough cohesive elements are present in the cohesive zone. Clearly, the non-linear stress distribution is not captured, comparing the blue curve obtained with fewer elements to the black curve obtained with a sufficient amount of elements in the cohesive zone. This results in jumps or oscillations in the load-displacement response and makes convergence of the solution challenging [60]. Zooming in on the load-displacement curve of Figure 4.10, these jumps/oscillations become apparent.

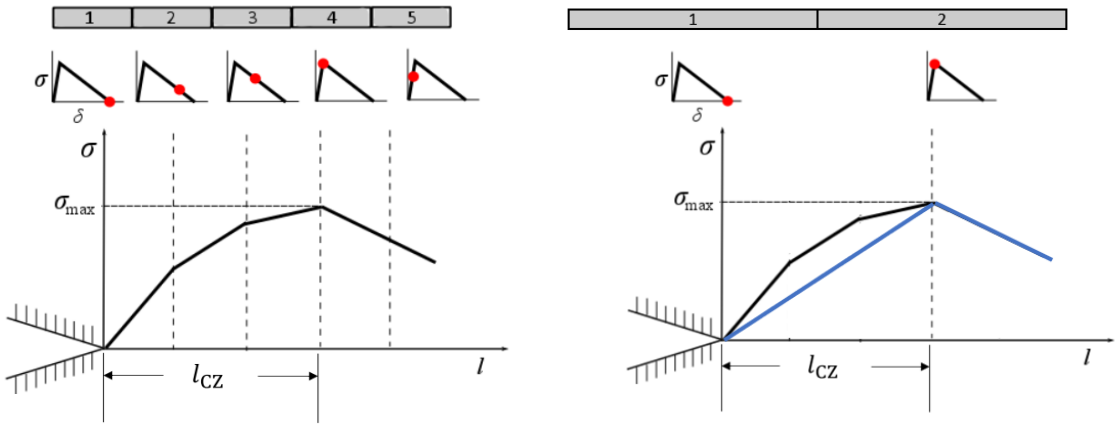

(a) For a fine mesh.

(b) For a coarser mesh.

Figure 4.9: Stress state in the cohesive zone ahead of the crack tip for two different mesh sizes [61].

Furthermore, the cohesive zone length is dependent on the critical fracture toughness. From the status file of the coarser model, it becomes clear that more and smaller increments and more iterations per increment are required after damage has already initiated and propagated. An explanation for this could be that during initiation, the separation mode is mixed, while when the damage has propagated already, the separation mode becomes more dominantly

mode I. Mode I has a lower critical fracture toughness and therefore a smaller cohesive zone. Therefore, later in the analysis, convergence is more difficult to reach because there are fewer cohesive elements in the smaller cohesive zone. This is probably also the reason why the oscillations in the load-displacement curve are more prominent later in the analysis, when the damage has already propagated a significant amount. All of this means that even though the mesh is coarser, the total CPU time does not decrease significantly due to convergence issues associated with the coarse mesh related to contact formulations and the cohesive elements. However, from the analysis, it could be seen that the model with the coarser mesh required less CPU time per increment compared to the model with the finer mesh, which is consistent with what would be expected for a coarser mesh.

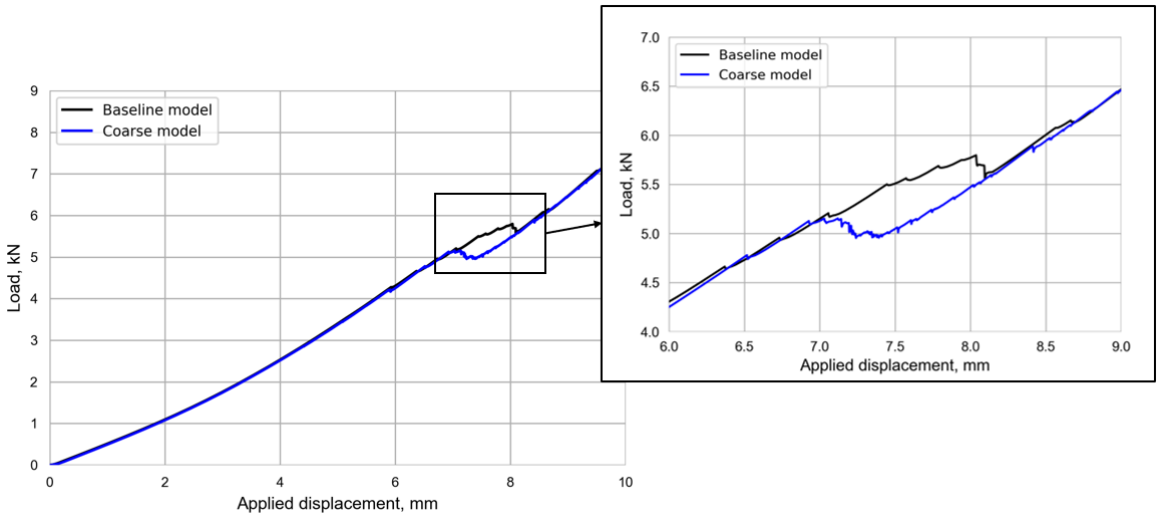

Figure 4.10: Comparison of the load-displacement curves of the baseline model and a coarser model, also showing oscillations in the curve as a result of large cohesive elements.

When comparing the load-displacement curves between the baseline model and the coarser model in Figure 4.10, it can be seen that the initial and final stiffness match well between the models. The load drop of the coarser model occurs approximately 1 mm before the load drop of the baseline model. This means that the displacement at which the damage reaches the noodle is underpredicted by the coarser model. The average displacement of the top indenters at which damage initiates is shown in Table 4.8. The displacement at which the damage initiates is determined as described in section 4.2.

Table 4.8: Comparison of the applied displacement at which damage initiates in the baseline model and the coarser model.

	Displacement [mm]
Baseline model	3.48
Coarse model	3.75
Relative difference	7.8%

The displacement at which damage initiates is higher for the coarse model, since the first failing cohesive element is larger. This means that the stress state at the crack tip is completely missed and that the element fails in an unstable way. This can be illustrated by looking at Figure 4.11.

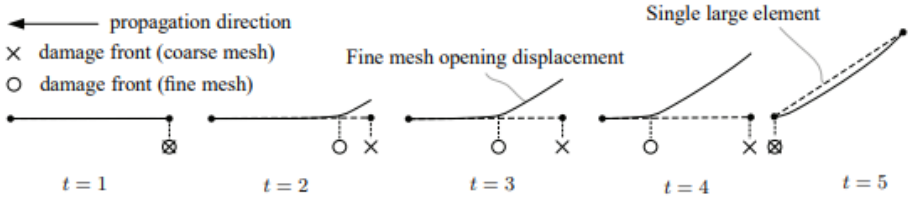

Figure 4.11: Schematic drawing showing the difference in opening displacement for a finer and coarser mesh [60].

Here, the difference in opening displacement between a finer and coarser mesh can be seen. The cross symbol indicates the damage front with a coarse element, while the circular symbol indicates the damage front with a finer element. As soon as the nodes of an element reach a certain opening displacement (onset opening displacement), damage propagates within the element until a critical opening displacement of the nodes is reached. At this point, the element has completely failed. Keeping in mind how damage initiation in the 7PB model was defined, this means that damage has initiated when an element has completely failed; its nodes have reached a critical opening displacement. Relating this back to Figure 4.11, it can be seen that the larger element temporarily arrests the damage propagation. However, when the nodes reach the onset opening displacement, the element becomes unstable and the nodes snap open all at once to the critical opening displacement, resulting in a failed element. This arrest causes the displacement of the top indenters at which the damage initiates to be larger for the coarser model than for the baseline model.

Finally, Figure 4.12 shows the damage at similar displacements for each of the models. It becomes clear that even though the damage initiates later in the coarser model, it propagates faster. Eventually, the damage reaches the noodle region at an applied displacement of approximately 7.5 mm. The displacement at which the damage reaches the noodle in the baseline model is approximately 8.1 mm. This means that the coarser model overpredicts the damage propagation rate, resulting in an underprediction of the displacement at which the damage reaches the noodle region.

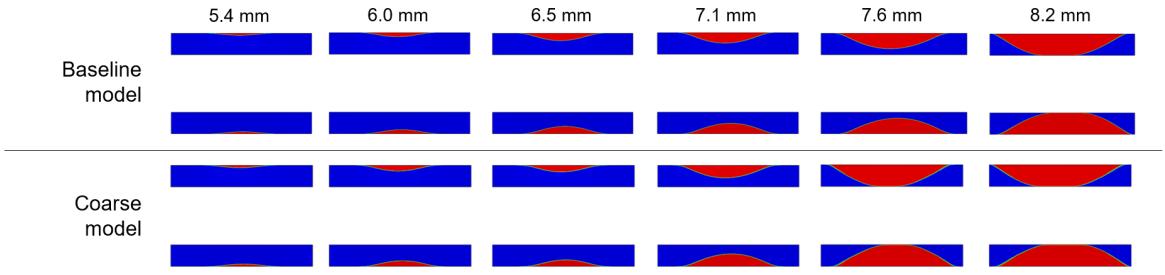

Figure 4.12: Comparison of the damage at similar displacements of the baseline model and a coarser model.

From these results, it seems that the coarser model is able to capture the global behaviour of the 7PB specimen, since the initial and final stiffness of the models match very well. However, the results also show that mesh refinement is needed in the area where damage is modelled; the area where the cohesive elements are. Because of the coarser cohesive elements, there are not enough elements in the cohesive zone to accurately capture the stress state at the crack tip, leading to inaccuracies in the damage predictions. This sensitivity analysis therefore demonstrates the importance of a mesh convergence analysis of the cohesive elements.

4.3.2 Thermal Step Sensitivity Analysis

In the baseline model, a thermal step is included before the displacement is applied to the top indenters. The thermal step is there to include geometric imperfections in the model. The temperature difference of 160^{o}C is not based on the curing cycle, but was determined such that the geometric imperfections of the model matched those of an actual physical panel that was being tested to validate the model [31]. The baseline model is compared to two different models: one without a thermal analysis and one with a thermal analysis, but with a temperature difference twice as high. Everything else is kept the same as in the baseline model. Table 4.9 shows the difference in temperature of the models between the initial conditions and loading. It should be noted that the temperature differences stated in this table are not physically representative of any curing process. They are purely meant to introduce geometric imperfections.

Table 4.9: Temperature differences in the thermal step between the baseline model, a model without thermal analysis and a model with an increased thermal analysis.

	Thermal step?	Temperature difference [^{o}C]
Baseline model	yes	160
Model without thermal analysis	no	0
Model with increased thermal analysis	yes	380

In Figure 4.13, the contour plots of the out-of-plane displacements at the beginning of the loading step (so at the end of the thermal step, if there is a thermal step) for each of the models can be seen. In Subfigure 4.13(a), the plot of the baseline model is shown, while in Subfigure 4.13(b) and Subfigure 4.13(c), the plots for the model without thermal analysis and the model with an increased temperature in the thermal analysis are shown respectively. As mentioned before, the indenters and skin stay in contact through spring elements during the thermal analysis, which allows for the derivation of the out-of-plane displacement of the top indenters at the end of the thermal step. After all, when the displacement is applied to the top indenters, this is done starting from their position at the end of the thermal step.

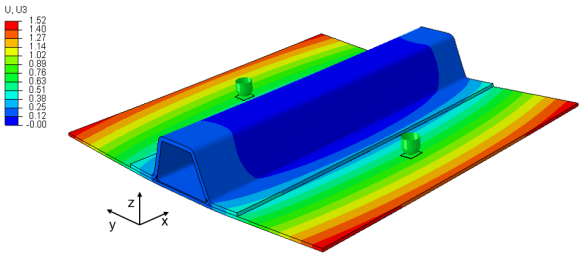

(a) Out-of-plane displacements at the beginning of the loading step of the baseline model.

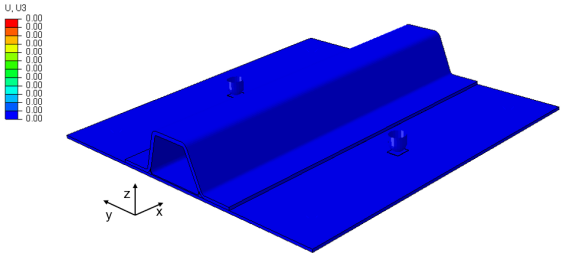

(b) Out-of-plane displacements at the beginning of the loading step of the model without a thermal analysis.

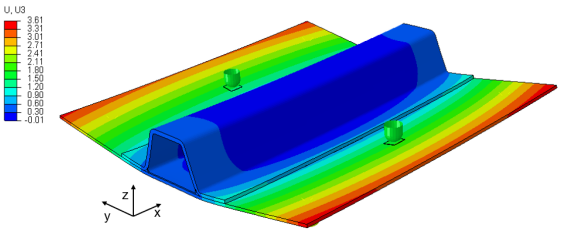

(c) Out-of-plane displacements at the beginning of the loading step of the model with an increased temperature in the thermal step.

Figure 4.13: Comparison of the out-of-plane displacements at the end of the thermal analysis, before the loading step, of three models with different thermal analyses, deformation scale factor = 5.

Both the values in Table 4.10 and the contour plots in Figure 4.13 show that the geometric imperfections increase as the temperature difference in the thermal step increases. From the contour plot, it also becomes clear that the shape of the geometric imperfection, when a thermal step is included, is the same. Both the baseline model and the model with an increased temperature in the thermal step show that the edges of the specimen curve upwards, which is consistent with how physical panels slightly curve upwards after cooling down from curing.

Table 4.10: Out-of-plane displacement of the top indenters at the beginning of the loading step.

	Displacement left indenter [mm]	Displacement right indenter [mm]
Baseline model	0.69	0.71
Model without thermal analysis	0	0
Model with increased thermal analysis	1.58	1.69

Figure 4.14 shows the influence of the geometric imperfections on the load-displacement curve. It becomes clear that, in this case, the geometric imperfections decrease the specimen stiffness. However, the difference in stiffness is rather small.

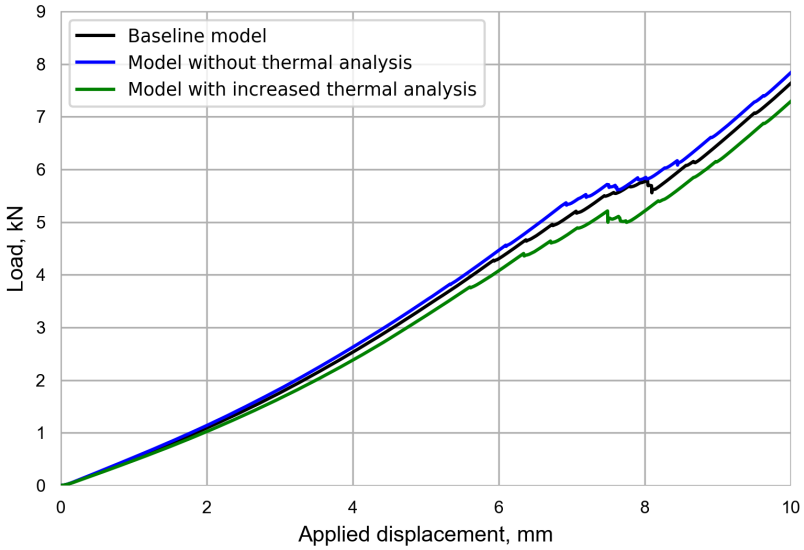

Figure 4.14: Comparison of the load-displacement curves of the baseline model, a model without the thermal analysis and a model with an increased temperature in the thermal step.

Considering the displacement at which damage initiates, the same methodology as described in previous sections is used. This way, the values shown in Table 4.11 are obtained.

Table 4.11: Comparison of the applied displacement at which damage initiates in the baseline model, the model without thermal analysis and the model with an increased temperature in the thermal step.

	Displacement [mm]	Relative difference
Baseline model	3.48	-
Model without thermal analysis	3.53	1.4%
Model with increased thermal analysis	3.26	-6.3%

Once again, it can be seen that an increase in temperature difference and therefore an increase in geometric imperfection, causes the damage to initiate earlier. Next to that, the difference in damage propagation rate is similar: the larger the temperature difference and therefore imperfection, the higher the damage propagation rate. However, the difference in damage at similar displacements (see Figure 4.15) is rather small.

From these results, it becomes clear that the higher the temperature difference, the larger the geometric imperfections. Furthermore, the geometric imperfections seem to have only a limited effect on the results. With a larger imperfection, the specimen stiffness is slightly decreased, while the displacement at which damage initiates and the damage propagation rate are slightly increased.

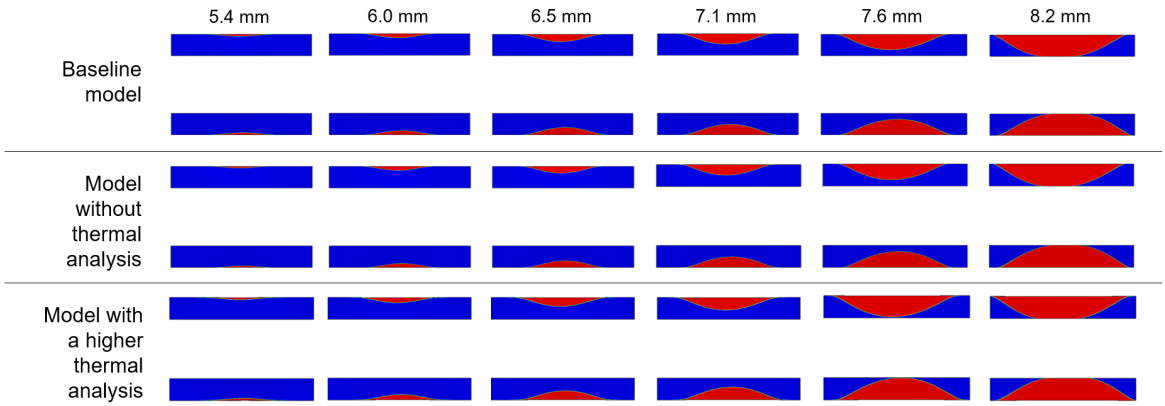

Figure 4.15: Comparison of the damage at similar displacements of the baseline model, a model without the thermal analysis and a model with an increased temperature in the thermal step.

4.3.3 Cohesive Law Sensitivity Analysis

Finally, a comparison is made between the baseline model and two additional models, each of which has a different cohesive law applied to the cohesive elements. As mentioned in section 4.1, the baseline model contains two strips of cohesive elements, underneath each of the flanges. The behaviour of the cohesive elements is dictated by a traction-separation law. In the baseline model, this is a trilinear cohesive law, through the superposition of two bilinear cohesive laws and is meant to simulate the R-curve effect. The first cohesive law is referred to as the cohesive base and is based on standard tape/tape interlaminar properties, since these are able to capture the damage initiation accurately [30]. The second bilinear law is referred to as the bridging law and is meant to capture the R-curve effect. In the baseline model, the bridging law is referred to as the tape/fabric bridging law. The properties used in the tape/fabric bridging law are based on the difference between the steady-state values from the standard tape/tape and non-standard tape/fabric interfaces. The properties of the cohesive base and tape/fabric bridging law can be seen in Table 4.3. In this analysis, the baseline model is compared to a cohesive base model and a structural bridging model. For the former, the cohesive base model, a single bilinear cohesive law is applied based on the cohesive base properties, as opposed to a trilinear cohesive law in the baseline model. For the latter, the structural bridging model, a trilinear cohesive law is applied. Here, the first bilinear law is the same as the one applied in the baseline model, namely, the cohesive base. The bridging law however is referred to here as the structural bridging law. In this bridging law, an increased set of properties is used. This way, the R-curve effect, not only from damage mechanisms at the skin-stringer interface, but also from damage mechanisms surrounding the skin-stringer interface, is captured. The properties of the different laws used in the three models can be seen in Table 4.12. In subsection 4.1.2, a description of how the cohesive base and the tape/fabric bridging properties are obtained, is provided. To obtain the structural bridging properties, a similar method is used as for the tape/fabric bridging properties; the fracture toughness values for the structural bridging law are calculated by ensuring that the sum of the steady-state tape/tape fracture toughness and the structural bridging fracture toughness is equal to four times the initiation tape/tape fracture toughness. The B-K coefficient, interlaminar strengths and penalty stiffnesses are then determined in a similar way as for the tape/fabric

bridging law [15].

Table 4.12: Properties used in the baseline model, cohesive base model and structural bridging model [15].

	K_I [N/m^3]	K_{II} [N/m^3]	G_{Ic} [kJ/m^2]	G_{IIc} [kJ/m^2]	σ_c [MPa]	τ_{IIc} [MPa]	η_{BK} [-]
Tape/fabric bridging (baseline model)	$5.43e^{12}$	$8.14e^{12}$	0.350	2.102	6.89	20.67	3
Cohesive base	$4.89e^{13}$	$3.53e^{13}$	0.240	0.739	62.29	92.95	2.07
Structural bridging	$2.71e^{12}$	$4.07e^{12}$	0.525	2.802	3.45	10.34	3

For the models using the trilinear cohesive law, the layer of cohesive elements underneath the flanges is duplicated, such that a new layer of cohesive elements is created that shares nodes with the original layer. The cohesive base properties are assigned to the original layer, while the tape/fabric bridging properties and the structural bridging properties are assigned to the duplicate layer of the baseline model and the structural bridging model respectively. Figure 4.16 shows the load-displacement curves of the three models. It can be seen that the initial stiffness matches well between the models. Next to that, it becomes clear that the models with a trilinear cohesive law maintain load-carrying capabilities longer; the load drop, when the damage reaches the noodle area, is at a higher applied displacement for the models with the trilinear cohesive law. This is consistent with the R-curve effect. Next to that, the load drop for the structural bridging model is clearly at a larger displacement and load compared to the baseline model, indicating that increased bridging properties increase the R-curve effect.

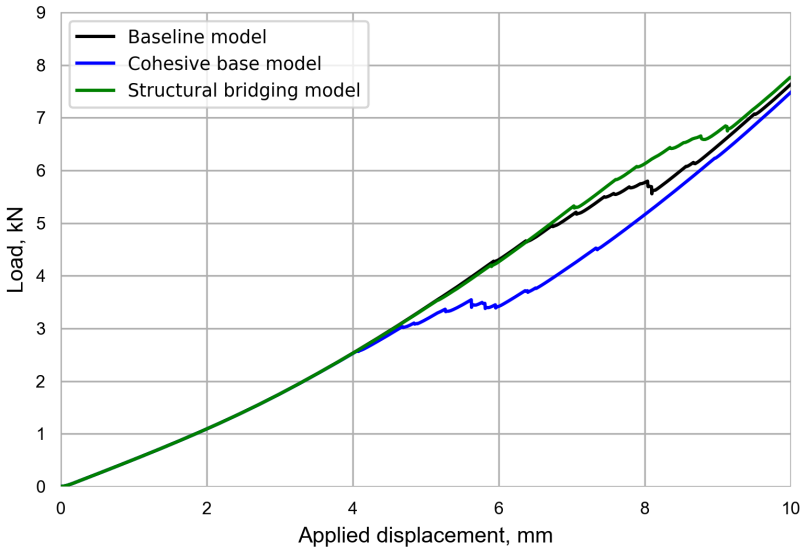

Figure 4.16: Comparison of the load-displacement curves of the baseline model, a model using a single bilinear cohesive law and a model using a trilinear cohesive law with structural bridging properties.

Table 4.13 shows the displacement at which damage initiates for each of the models.

Table 4.13: Comparison of the applied displacement at which damage initiates in the baseline model, the cohesive base model and the structural bridging model.

	Displacement [mm]	Relative difference
Baseline model	3.48	-
Cohesive base model	3.19	-8.3%
Structural bridging model	3.32	-4.6%

The applied displacement at which damage initiates matches relatively well, which makes sense since the damage initiation is mostly determined by the cohesive base properties, which are the same in all three laws. This also indicates that the bridging law has a limited effect on damage initiation, which is consistent with the R-curve effect influencing the behaviour during propagation. This becomes clear when looking at the damage propagation, shown in Figure 4.17, for each of the models. Even though damage initiates around the same applied displacement, the damage clearly propagates at different rates. This can also be related back to the load-displacement curve, showing the load drop at different applied displacement values. The damage in the cohesive base model propagates fast, while in the baseline model and structural bridging model, the rate of propagation is significantly lower. In fact, here, the R-curve effect is clearly visible once again: the higher the bridging properties, the slower the damage propagation.

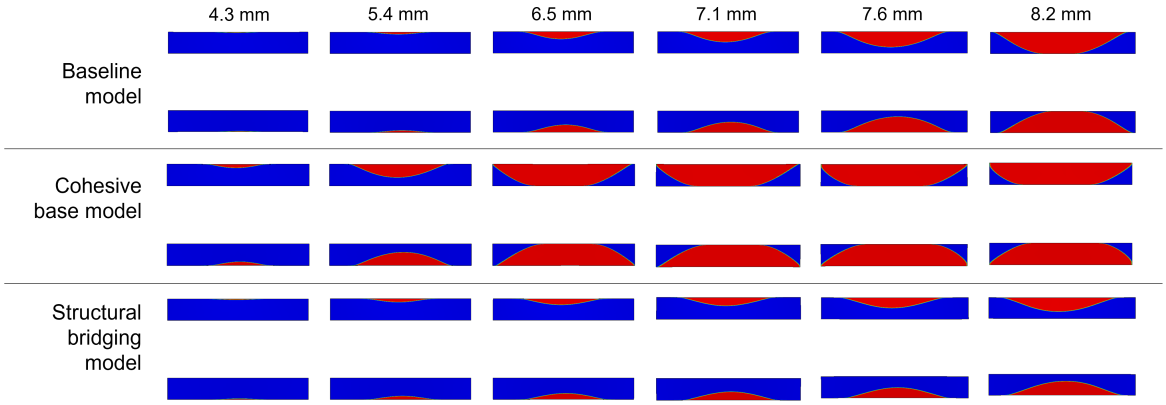

Figure 4.17: Comparison of the damage at similar displacements of the baseline model, a model using a single bilinear cohesive law and a model using a trilinear cohesive law with structural bridging properties.

Chapter 5

Multistringer Panel

The multistringer panel in compression is modelled by implementing the skills and lessons learned from the baseline model, discussed in chapter 4. In this chapter, the set up of the multistringer panel model is discussed first. Afterwards, a linear eigenvalue analysis is performed to identify the buckling loads, displacements and eigenmodes. Next, non-linear buckling analyses are performed on the panel and the model is verified. Furthermore, some sensitivity analyses are performed to identify the effect of the mesh, the geometric imperfections and the step settings in Abaqus.

5.1 Set Up of the Multistringer Panel Model

In this section, the procedure of how the multistringer panel model is created, is discussed.

5.1.1 Geometry

As mentioned before, the multistringer panel contains four co-cured hat stringers. The stringer and overall panel dimensions have been discussed in section 3.1. The panel contains pad-up regions at the top and bottom edge of the panel to avoid failure there. The pad-up regions are built out of the same tape material as the skin and are such that in the padded areas the skin thickness is doubled, while still having a quasi-isotropic layup. The following layup is used for the pad-up regions: $[+45/-45/90/0/+45/-45]$. The layup of the skin and stringers can be found in section 3.1, as well as the lamina properties for the tape and fabric material. Potting is added to the ends of the panel to allow for a uniform load introduction.

5.1.2 Finite Element Model

A finite element model is created that aims to simulate the buckling behaviour of the panel in compression. To do so, the different parts of the panel are meshed, a material is assigned to all elements, interactions, constraints and boundary conditions associated with the load application are specified and finally, the model is submitted for analysis.

Mesh

Similar to the baseline model, the skin, interior wrap and overwrap are meshed using SC8R elements. One element is used through the thickness of each of the composite parts. The noodle region is not modelled in detail and is meshed with C3D8R elements. The mesh size is uniform throughout the entire panel and is approximately 2.54 mm x 2.54 mm. Furthermore, the mesh of the skin directly underneath the stringer, matches the stringer mesh.

Material Definition

The material properties used for the noodle regions and composite regions can be found in Table 4.4 and Table 3.1 respectively. Next to that, no damage is modelled in the multistringer panel. This is because only the post-buckling behaviour of the multistringer panel is to be obtained, to see how it deforms. Based on the post-buckling deformation of the panel, the critical locations are determined and single stringer specimens, representative of the behaviour at these locations are sized.

Constraints and Boundary Conditions

The stringers and pad-up regions are tied to the skin using tie constraints. Boundary conditions are imposed on the model. To simulate the effect of potting at the ends, the nodes of the stringers, skin and padding in the first 45 mm of both ends are constrained in translation along the z-direction, so out-of-plane. This boundary condition is indicated in red in Figure 5.1.

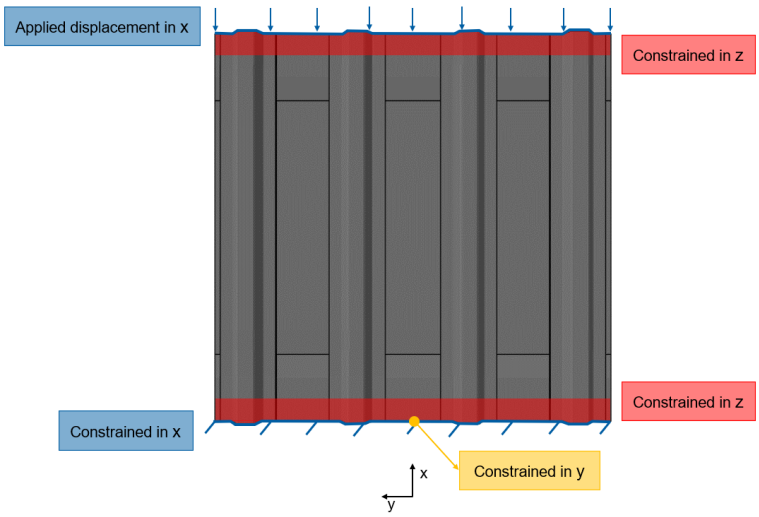

Figure 5.1: Boundary conditions imposed in the model of the multistringer panel.

The bottom edge of the panel is constrained along the x-direction, indicated with blue stripes in Figure 5.1. Next to that, on a single node on the bottom edge of the panel, a constraint is applied in the y-direction to prevent rigid body motion. This is indicated by the yellow dot in Figure 5.1. Finally, a compressive load is applied using displacement control: the displacement is applied to the top edge of the panel in the negative x-direction.

Analyses

Two kinds of analyses are performed on the multistringer panel. First, a linear eigenvalue analysis is performed to identify the buckling loads, displacements and eigenmodes. This is useful to estimate the critical buckling load and possibly how the panel will collapse, based on the buckling mode shape. Next to that, the buckling mode shapes can be used to apply scaled geometric imperfections when performing a non-linear buckling analysis.

Secondly, a non-linear buckling analysis is performed. This is to include the effect of any geometric non-linearities prior to buckling, to capture the post-buckling response and to obtain the entire buckling behaviour of the multistringer panel. Different solvers can be used for a non-linear buckling analysis. Initially, the static Newton-Raphson solver is used for the analysis. This is the default solver used in Abaqus for (quasi-)static problems. However, the Newton-Raphson solver is often incapable of solving for instabilities, so if instabilities occur during the analysis, a dynamic solver should be used instead.

5.2 Linear Eigenvalue Analysis

A linear eigenvalue analysis is performed to identify the buckling loads and buckling mode shapes of the multistringer panel. A linear perturbation step is applied. The compression is applied in two different ways: in load control and in displacement control. This is done such that both the critical buckling load, as well as the critical buckling displacement can be retrieved. The magnitude of the applied load and displacement is set to 1 N and 1 mm respectively. In a linear perturbation step, the magnitude of the applied load or displacement is irrelevant, since the eigenvalues are scaled with respect to them. By applying a unit load and displacement, the eigenvalues are scaled by one and the critical buckling load and displacement can be obtained directly from the eigenvalues.

In Figure 5.2, the first three eigenmodes of the multistringer panel can be seen, with their corresponding critical buckling load and displacement. It should be noted that the buckling mode shapes do not show the actual magnitude of the deformation at the applied critical buckling load or displacement, but are normalized such that the maximum out-of-plane displacement is equal to one. For the multistringer panel, the critical buckling load of the panel is approximately equal to 312 N and the critical buckling displacement of the panel is approximately equal to 1.5 mm.

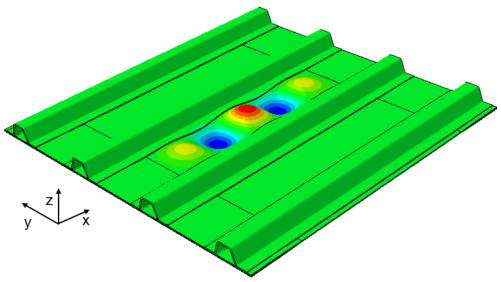

(a) First buckling eigenmode at a displacement of 1.486 mm and a load of 312.3 kN.

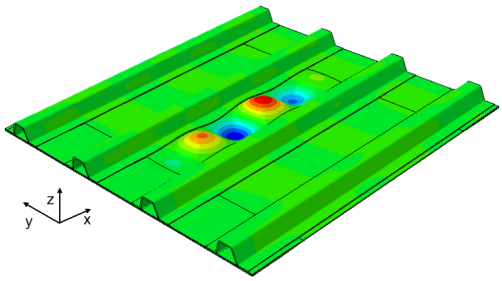

(b) Second buckling eigenmode at a displacement of 1.489 mm and a load of 313.0 kN.

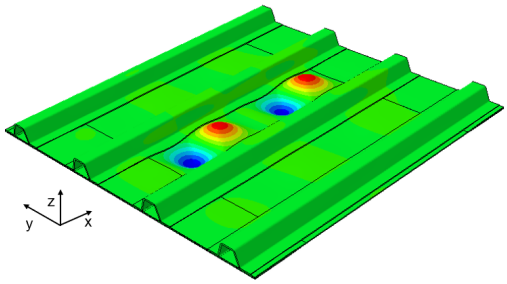

(c) Third buckling eigenmode at a displacement of 1.608 mm and a load of 339.9 kN.

Figure 5.2: An overview of the first three buckling eigenmodes of the multistringer panel and their corresponding buckling displacement and load, deformation scale factor = 30.

5.3 Non-Linear Buckling Analysis

To include the effect of geometric non-linearities and to obtain the post-buckling behaviour of the multistringer panel, a non-linear buckling analysis is performed.

5.3.1 Verification of the Multistringer Panel Model

A non-linear buckling analysis is performed on the multistringer panel, using the static Newton-Raphson solver. The panel is loaded in compression through displacement control. Specifically, a displacement of 4 mm is applied in the negative x-direction. To verify the model, the results are compared to the results of the model developed by Action and Palliyaguru [1]. Here, the authors tested a similar panel with the same dimensions in compression. Furthermore, they developed a numerical model to predict the compressive behaviour of the panel and to simulate skin-stringer separation. A comparison of the multistringer panel model with the model developed by Action and Palliyaguru is made in terms of the load-displacement curve, the buckling mode and the out-of-plane displacement at a single point.

Figure 5.3 shows the load-displacement curves of both models.

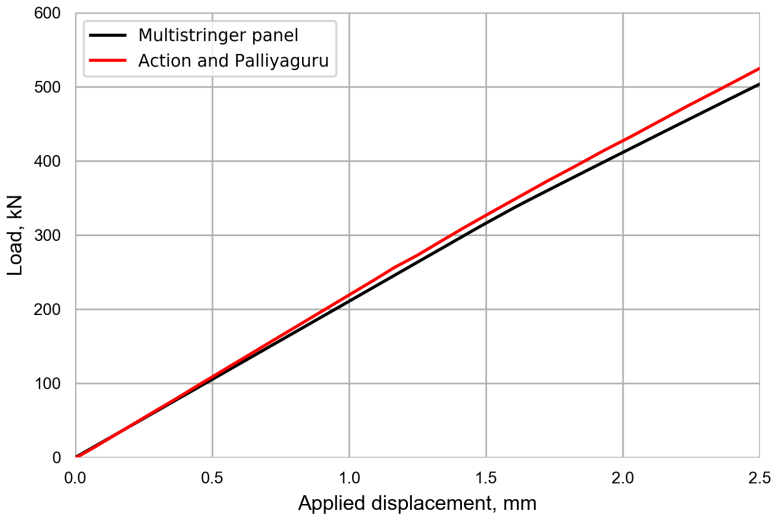

Figure 5.3: Comparison of the load-displacement curves of the multistringer panel model and the model developed by Action and Palliyaguru.

It can be seen that the curves match relatively well. The stiffness of the multistringer panel model is slightly smaller than the stiffness of the model developed by Action and Palliyaguru. This may be caused by several factors:

- The presence of the Teflon inserts in the model developed by Action and Palliyaguru [1]. The authors developed a model for a non-pristine panel. Along both sides of the central bay, underneath the stringer flanges, Teflon inserts were modelled.
- The inclusion of a damage model in [1]. Interlaminar damage at the skin-stringer interface was included in the model through the use of the Virtual Crack Closure Technique.
- The difference in the layup of the skin. In the layup of the skin in [1], the $+45$ and -45 plies are interchanged with respect to the layup used in the model developed here. The reason behind this is that a physical specimen of the multistringer panel is to be used in future work to validate the numerical predictions made in this research. In this physical panel, the $+45$ and -45 plies were switched. Therefore, in order to make the results of this research valid for validation purposes in future work, the skin layup of the physical panel is used here.
- The possible difference in the layup of the pad-up region and potting length. The layup of the pad-up regions and the length of the potting area were not specified in [1], so there may be differences between the models there as well.
- Small differences in the stringer geometry.
- Small differences in the mesh.
- Small differences in the material input parameters due to the conversion from US units to SI units.

However, considering the differences, the curves match relatively well. Next to that, it should be noted that even though the applied displacement was specified to be 4 mm, the load-displacement curves are shown only up until 2.5 mm. This is because, using the static Newton-Raphson solver, the analysis was not able to converge beyond 2.5 mm. This indicates that there is probably some instability happening at this point that could not be captured with this solver. This will be further investigated in subsection 5.3.3.

Figure 5.4 shows the load-displacement curves, with the buckling load of the central bay indicated. The buckling range defined by Action and Palliyaguru is compared to the critical buckling load obtained through the eigenvalue analysis described in section 5.2.

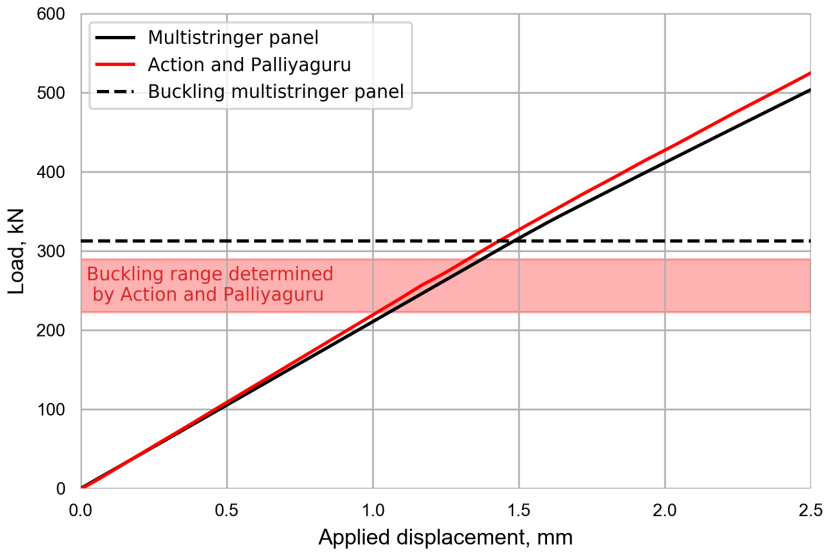

Figure 5.4: Comparison of the load-displacement curves of the multistringer panel model and the model developed by Action and Palliyaguru, including an indication of the load at which the central bay buckles.

The values of the buckling loads for each of the models can be seen in Table 5.1. In the model developed by Action and Palliyaguru, the central bay of the panel buckles earlier than in the model developed here. This makes sense, since the panel of Action and Palliyaguru has Teflon inserts underneath the stringer flanges in the central bay. This causes the central bay to buckle earlier than in a pristine panel.

Table 5.1: Comparison of the buckling load of the central bay of the multistringer panel and the model developed by Action and Palliyaguru.

	Buckling load [kN]
Multistringer panel	312.3
Action and Palliyaguru	222.4 - 289.1
Relative difference	40.4% - 8.0%

Figure 5.5 shows the load-displacement curves, with the buckling load of the outer bays of the models indicated. The values for the buckling load are determined by considering the non-linear buckling analysis results and are taken as the load at which the buckling mode shape in the outer bays starts to develop.

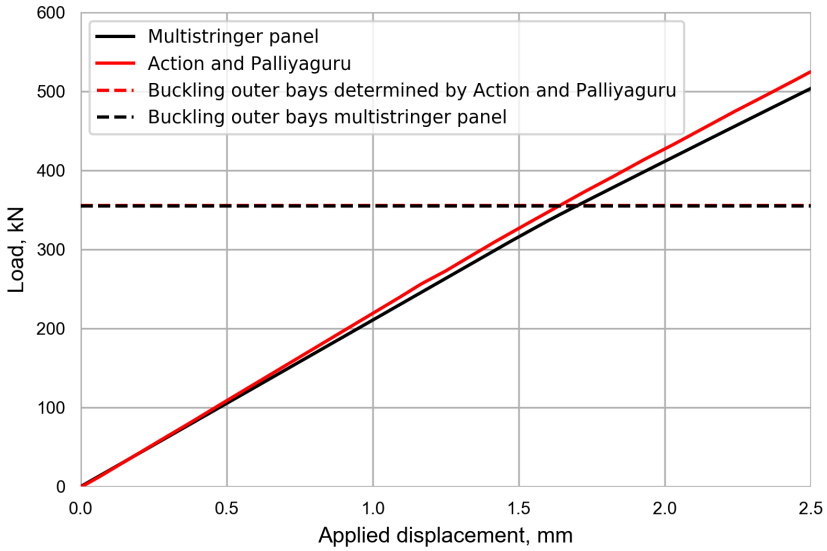

Figure 5.5: Comparison of the load-displacement curves of the multistringer panel model and the model developed by Action and Palliyaguru, including an indication of the load at which the outer bays buckle.

From the graph, it already becomes clear that the loads match very well. This is confirmed when looking at the values for the buckling load shown in Table 5.2. Since no Teflon inserts are included in the outer bays in either of the models, it makes sense that the outer bays buckle at approximately the same load.

Table 5.2: Comparison of the buckling load of the outer bays of the multistringer panel and the model developed by Action and Palliyaguru.

	Buckling load [kN]
Multistringer panel	355.2
Action and Palliyaguru	355.9
Relative difference	-0.2%

Then, a comparison is made in terms of the buckling mode shape at similar loads. Figure 5.6 shows the buckling shape of both of the models. Since the model developed here did not converge above a displacement of 2.5 mm, the buckling mode shape at a load of 555 kN could not be obtained. Nevertheless, it can be seen that both of the models buckle in the central bay first and in five halfwaves. This makes sense since the central bay is slightly larger than the

outer bays. At a higher applied displacement, the outer bays buckle in five halfwaves as well. Apart from that, the pre-buckling shape differs between the models. This can be explained by the presence of the Teflon inserts in the model developed by Action and Palliyaguru.

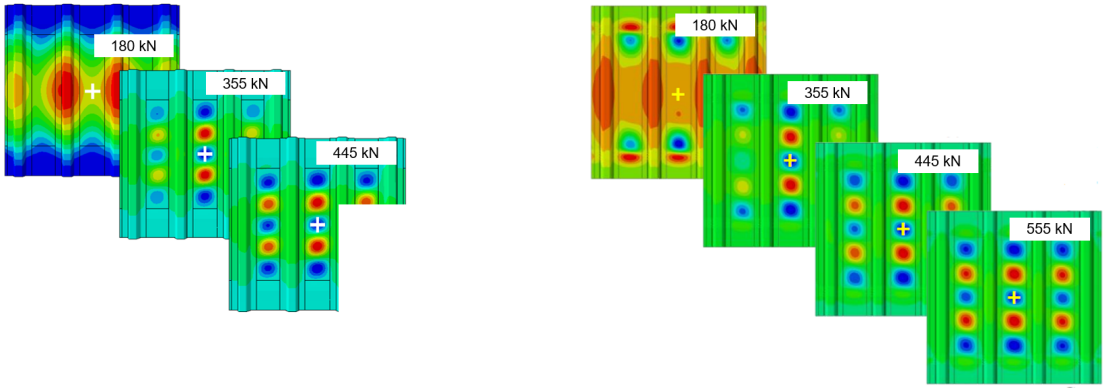

(a) Buckling shape of the multistringer panel.

(b) Buckling shape of the model developed by Action and Palliyaguru [1].

Figure 5.6: Comparison of the buckling shape of the multistringer panel and the model developed by Action and Palliyaguru.

Looking at the out-of-plane displacement of a single point, the curves in Figure 5.7 can be obtained. The point that is considered is a point in the center of the panel. This corresponds approximately with the middle of the central halfwave in the central bay and is indicated with a white cross in Figure 5.6.

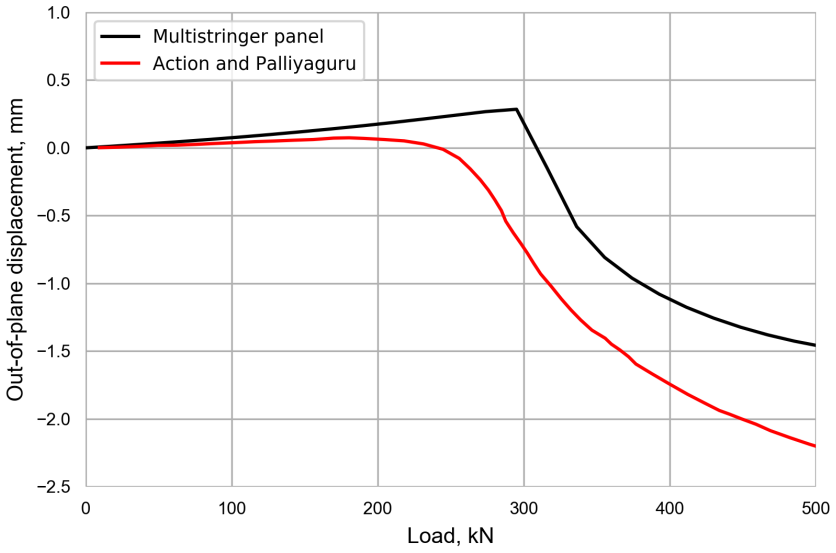

Figure 5.7: Comparison of the out-of-plane displacement of a point in the central bay of the multistringer panel and the model developed by Action and Palliyaguru.

This graph clearly shows that the model developed by Action and Palliyaguru buckles earlier than the model developed here. This is mainly due to the presence of the Teflon inserts. Next to that, after buckling, the model by Action and Palliyaguru shows a larger out-of-plane displacement at similar loads. This makes sense since interlaminar damage is included in this model. The results show that skin-stringer separation at the central bay leads to opening of the interface, allowing for the skin in the central bay to displace more than if the skin and stringers were rigidly tied together as is the case in the model developed here.

Evaluating these results, it can be said that, considering the known differences between the two models, the multistringer panel can be verified with the model developed by Action and Palliyaguru, since every discrepancy in the results could be accounted for. Therefore, this model can be used to determine the critical locations in the multistringer panel and for the development of single stringer specimens to simulate the behaviour in more detail at these critical locations.

5.3.2 Simplified Multistringer Panel Model

An effort is made to develop a simplified model, without padding and potting that is representative of the multistringer panel model. This way, the physical behaviour of the panel can be obtained with a simpler model. In order to find this simplified model, four aspects are considered:

1. The simplified model should have a similar buckling load and buckling displacement as the multistringer panel model. This is obtained through a linear eigenvalue analysis.
2. The simplified model should have a similar stiffness. The comparison with the multistringer panel is made by looking at the load-displacement curves obtained from a non-linear buckling analysis.
3. The simplified model should have a similar buckling mode shape in the central bay. The comparison with the multistringer panel model is made by looking at the contour plot of the out-of-plane displacements at similar applied displacement values. Since the central bay is slightly larger, the panel buckles there first. Therefore, it is likely that the critical location will be in the central bay as well. This is why only the buckling mode shape in the central bay is considered in the search of the simplified model.
4. The simplified model should have similar out-of-plane displacement values in the central bay. This is because the magnitude of the buckling halfwaves directly influences the damage initiation underneath the flanges. A comparison is made with the multistringer panel model through out-of-plane displacement vs. applied displacement plots obtained from a non-linear buckling analysis.

When all four of these requirements are fulfilled, a length parameter of the simplified model is obtained. To limit the range of considered lengths, only lengths larger than the free length and smaller than the panel length without potting are considered. This is visualized in Figure 5.8. This means that the minimum length is 490.22 mm and the maximum length is 657.86 mm.

In the simplified models, the top and bottom edges are constrained in the z-direction (out-of-plane). Furthermore, the bottom edge is additionally constrained in the x-direction (the

loading direction). To prevent rigid body motion, a single node on the bottom edge is constrained in the y-direction (the transverse direction). The other two edges are left free. The compression is applied through displacement control at the top edge of the panels. The methodology of finding the length of the simplified model, that satisfies all the criteria is as follows. First, the minimum, maximum and the length exactly in between those are considered. From those results, additional lengths are considered by always taking the middle between two already considered adjacent lengths.

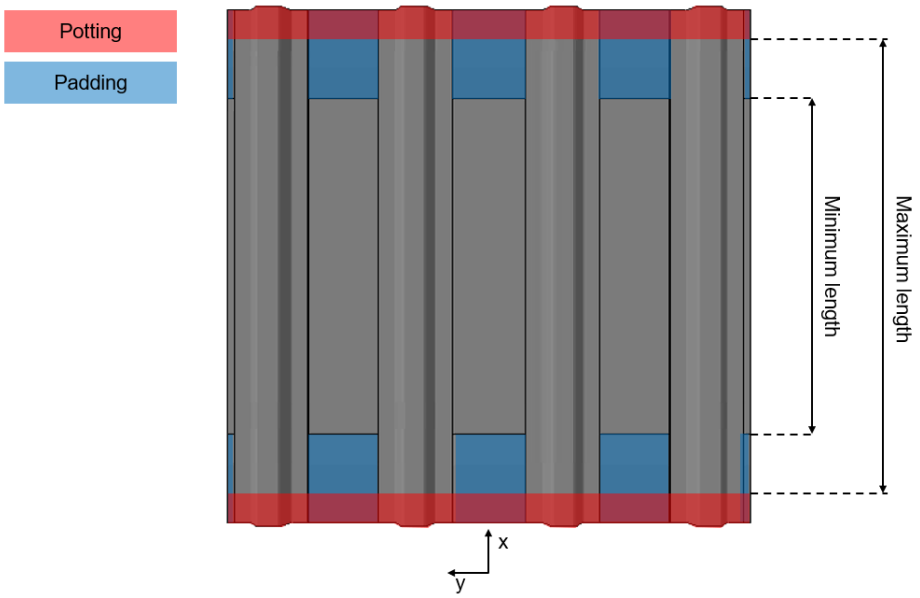

Figure 5.8: Schematic showing the range of lengths considered for a simplified model.

Doing so, a trend is discovered: the larger the length of the simplified model, the better the accuracy is in terms of critical buckling load, critical buckling displacement, stiffness and out-of-plane displacement. However, the smaller the length of the simplified model, the better the accuracy is in terms of the buckling mode shape. Since the buckling mode shape directly influences the critical locations and therefore the damage initiation and propagation, the requirement with respect to the buckling mode shape of the central bay is prioritized. After doing many iterations through the range of allowable lengths, the conclusions about the buckling mode shapes can be seen in Table 5.3.

Table 5.3: Buckling mode shapes in the bays of the simplified models.

Length range	Outer bays	Central bay
490.22 mm - 550 mm	5 halfwaves	5 halfwaves
550 mm - 585 mm	7 halfwaves	5 halfwaves
585 mm - 657.86 mm	7 halfwaves	7 halfwaves

Since the buckling mode shape of the central bay is driving here, the range of lengths is limited further: only panels with a length between 490.22 mm and 585 mm satisfy the buckling mode

shape criterion. Figure 5.9 shows the load-displacement curves of the considered simplified models, that satisfy the buckling mode shape requirement. Next to that, Figure 5.10 shows the out-of-plane displacement of a point at the central halfwave in the central bay in terms of the applied displacement of the considered models and the multistringer panel model.

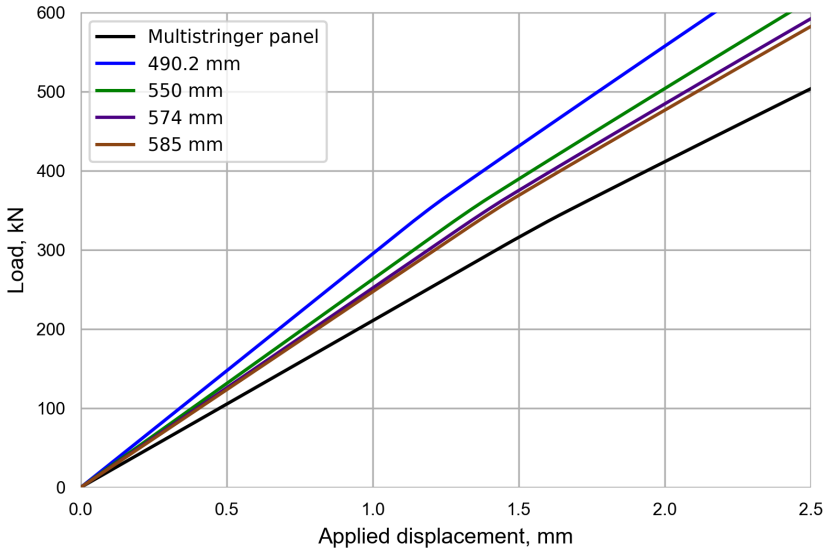

Figure 5.9: Comparison of the load-displacement curves of simplified models with the multi-stringer panel model.

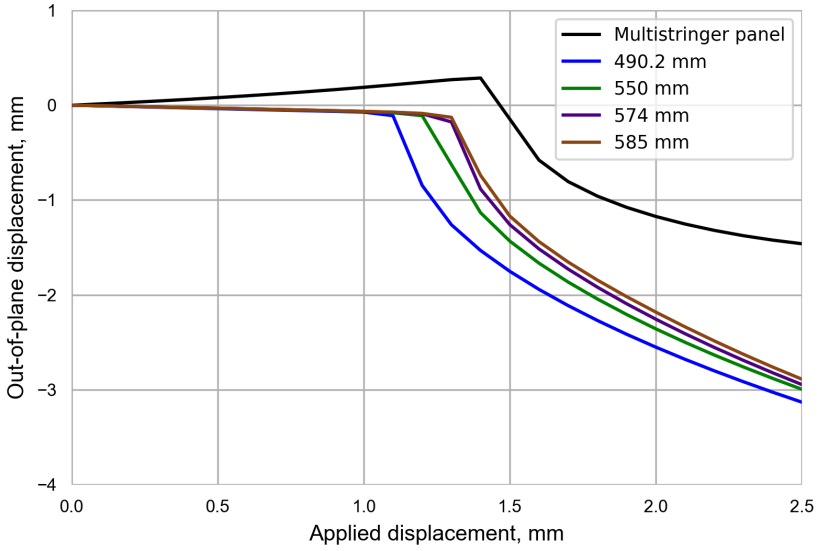

Figure 5.10: Comparison of the out-of-plane displacement of a point in the central bay of simplified models with the multistringer panel model.

From both of these graphs, it becomes clear that all of the considered simplified models deviate quite a lot from the multistringer panel model in terms of stiffness and magnitude of the out-of-plane displacement. According to Figure 5.9 and Figure 5.10, a panel with a length of 585 mm approaches the curves from the multistringer panel the best. In Table 5.4, the critical buckling load and displacement of the model of 585 mm can be seen in comparison to the multistringer panel model. The values reported in Table 5.4 are obtained through linear eigenvalue analyses.

Table 5.4: Comparison of the critical buckling load and displacement of a simplified model with a length of 585 mm and of the multistringer panel model.

	Critical buckling load [kN]	Critical buckling displacement [mm]
Multistringer panel	312.3	1.49
Simplified model - 585 mm	333.1	1.35
Relative difference	6.7%	-9.4%

Next to that, for the simplified model of 585 mm, a comparison is made with the multistringer panel model in terms of the buckling mode shape at similar applied displacements. This can be seen in Figure 5.11.

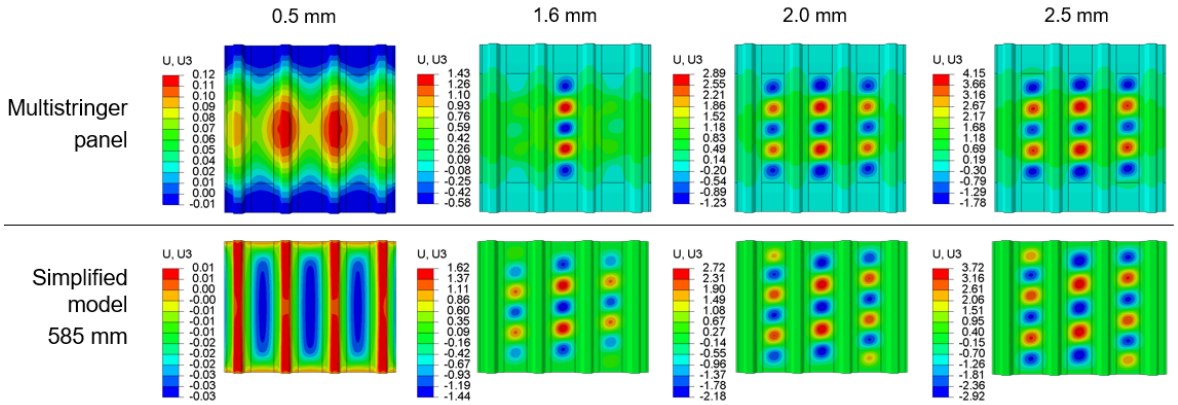

Figure 5.11: Comparison of the out-of-plane displacements at similar applied displacements of a simplified model with a length of 585 mm and of the multistringer panel model.

Even though, the critical buckling load, displacement and buckling mode shape of the central bay of the simplified model with a length of 585 mm match relatively well with the multistringer panel model, the stiffness and out-of-plane displacements are not accurate enough.

From these analyses, it becomes clear that it is not evident to find an equivalent simplified model as the pad-up regions redistribute the stress from the boundaries into the panel, affecting the panel behaviour as a whole. Therefore, it is decided that the multistringer panel model with padding and potting will be used for further analyses.

5.3.3 Dynamic Implicit Analysis

Now that the multistringer panel model has been verified and it has been decided to continue the analysis with the padded multistringer panel, rather than a simplified version of it, an effort is made to apply a displacement of 4 mm without convergence issues.

To do so, the analysis step is changed from a static Newton-Raphson step, to a non-linear dynamic implicit step. The dynamic implicit solver is much more stable than the Newton-Raphson solver. Even though it is a dynamic solver and the problem itself is not dynamic, quasi-static conditions can be enforced when using the dynamic implicit solver in Abaqus. The displacement is applied using velocity control. This means that a velocity of 4 mm/s is applied instantaneously to the top edge of the panel and is kept constant for a time period of 1 second. To ensure the solution accuracy, the results obtained from the dynamic implicit analysis are compared to the static Newton-Raphson results. A comparison of the load-displacement curves can be seen in Figure 5.12.

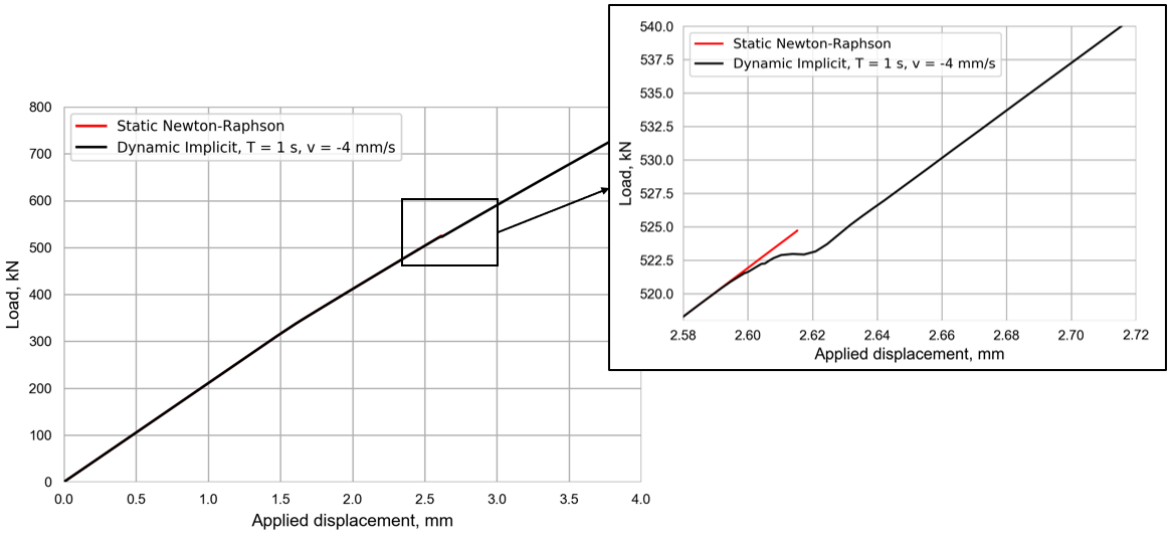

Figure 5.12: Comparison of the load-displacement curves of the multistringer panel using a Newton-Raphson analysis and a dynamic implicit analysis with a time period of 1 second and an applied velocity of -4 mm/s.

It can be seen that the curves match very well, indicating that the dynamic implicit analysis is able to provide an accurate solution. It can also be seen that the dynamic implicit analysis is capable of converging above a displacement of 2.5 mm. Zooming in on the region where the Newton-Raphson solver failed to converge, it can be observed that around an applied displacement of 2.6 mm, the slope of the curve decreases and the curve flattens until an applied displacement of approximately 2.62 mm is reached. After this point, the slope of the curve is recovered.

Considering the out-of-plane displacement of a single point at the center of the panel with respect to the applied load, shown in Figure 5.13, it can be seen that at the point where the Newton-Raphson analysis failed to converge, the dynamic implicit analysis shows that the negative out-of-plane displacement at this point suddenly changes to a positive displacement

of a higher magnitude. After this sudden change, the out-of-plane displacement becomes increasingly more positive as the load increases.

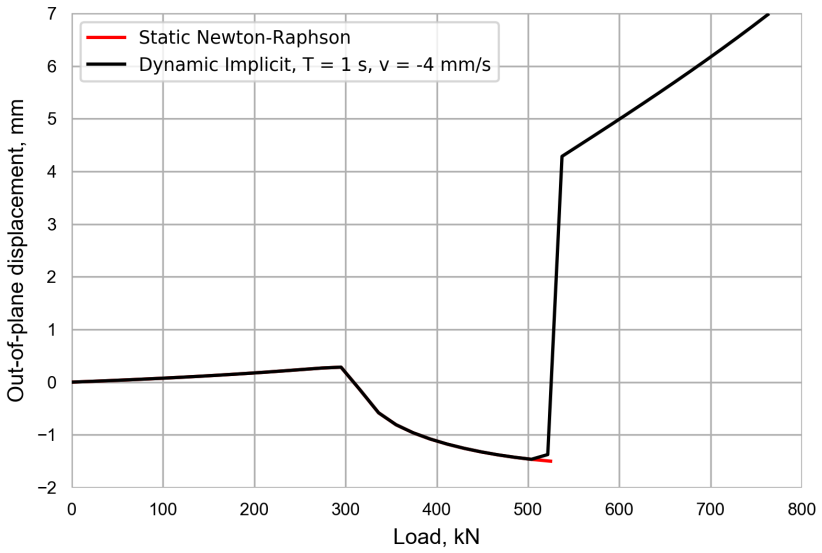

Figure 5.13: Comparison of the out-of-plane displacement of a point in the central bay of the multistringer panel using a Newton-Raphson analysis and a dynamic implicit analysis with a time period of 1 second and an applied velocity of -4 mm/s.

This indicates the presence of a mode jump, which is confirmed by looking at the contour plots in Figure 5.14. A mode jump can be defined as a sudden dynamic change to a higher mode shape of a structure that has already buckled. Some structures, when already buckled upon loading, contain multiple post-buckling equilibrium states. This means that the value of the total potential energy remains stationary; the stresses are in equilibrium and the strains are compatible. However, the structure is not necessarily stable when in equilibrium. While the load is increased, the equilibrium of the structure is maintained along a stable equilibrium path. However, for some values of the applied load, at a bifurcation point, the structure becomes unstable and the structure moves to a different deformation mode associated with a new post-critical equilibrium path to regain stability. A bifurcation point is defined as the intersection of two equilibrium paths [62]. This "move" is transient, meaning that it happens over a very short period of time. To capture this transient behaviour between the quasi-static parts, a solver is to be used that is able to capture this. That is why the dynamic implicit solver was able to capture the behaviour and the Newton-Raphson solver was not. Figure 5.14 shows that pre-buckling, the panel shortens and bulges outward slightly. At a displacement of approximately 1.5 mm, the central bay buckles into five buckling halfwaves. At a displacement of approximately 1.7 mm, the outer bays buckle as well into five halfwaves. This buckling mode shape is maintained until a displacement of approximately 2.6 mm is applied. At this point, the mode jump occurs and the buckling mode shape of all the bays suddenly changes from five to seven buckling halfwaves. For the remainder of the analysis, this mode shape is maintained. In the model of Action and Palliyaguru [1], no mode jump is observed because of the Teflon inserts along the central bay, which affect the buckling behaviour of the panel.

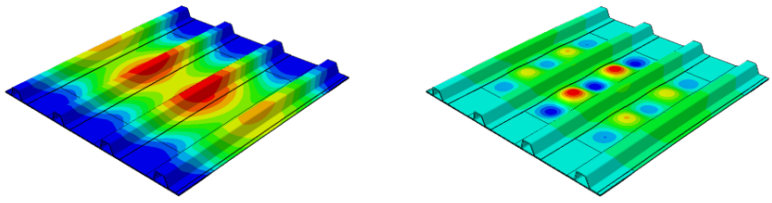

(a) 0.9 mm.

(b) 1.7 mm.

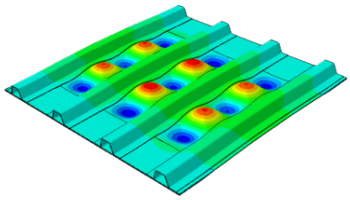

(c) 2.5 mm.

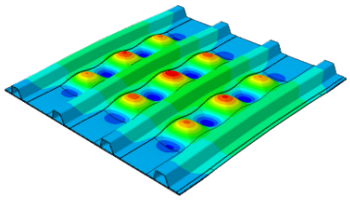

(d) 2.7 mm.

Figure 5.14: Buckling mode shape of the multistringer panel at different values of applied displacement, using a dynamic implicit analysis with a time period of 1 second and an applied velocity of -4 mm/s, deformation scale factor = 10.

Figure 5.15 shows the load-displacement curve obtained with the dynamic implicit analysis with the buckling loads and displacements of the bays, as well as the applied displacement at which the mode jump occurs.

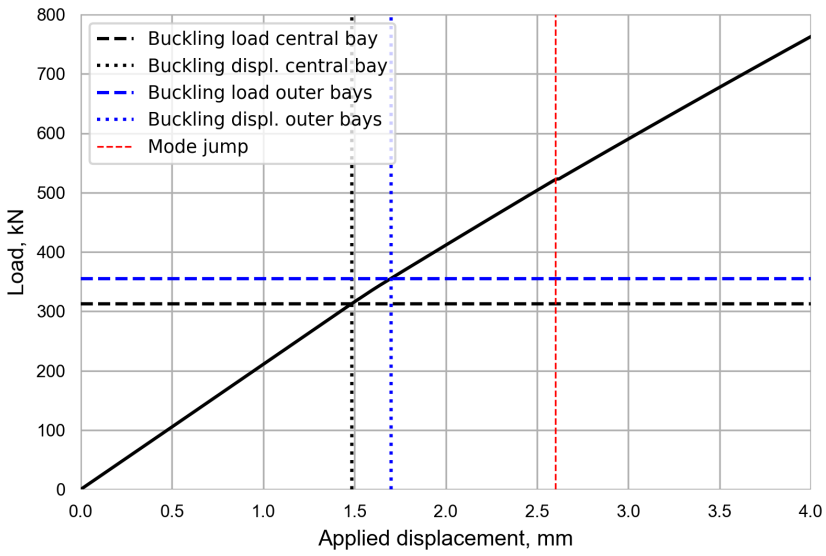

Figure 5.15: Load-displacement curve obtained with a dynamic implicit analysis, showing the critical buckling loads and displacements of all the bays and the displacement at which the mode jump occurs.

5.4 Sensitivity Analyses on the Multistringer Panel Model

In order to understand the influence of different parameters on the predictions of the multistringer panel model, three sensitivity studies have been performed. First of all, a sensitivity study considering the dynamic implicit parameters is performed. Then, a mesh sensitivity analysis is done and finally, an imperfection sensitivity study is performed. The results of the different models are compared to the multistringer panel model using the dynamic implicit solver, described in subsection 5.3.3.

5.4.1 Dynamic Implicit Sensitivity Analysis

A sensitivity study is performed on the parameters specified in the dynamic implicit step. This is done because, a change in those parameters can significantly improve the computational efficiency without losing too much of the solution accuracy. The influence of the length of the step time period and the applied velocity is investigated. For each of the considered models, the step time period and applied velocity are selected such that at the end of the step the total applied displacement is equal to 4 mm. The following models are considered:

Table 5.5: Different models used in the dynamic implicit sensitivity analysis.

Model	Step time period [s]	Applied velocity [mm/s]
Multistringer panel model	1	−4
Model 1	2	−2
Model 2	0.5	−8
Model 3	4	−1
Model 4	0.25	−16

A comparison in terms of solution accuracy and computational efficiency is made. The solution accuracy is defined as how well the load-displacement curve and out-of-plane displacement at a single point in the center of the panel match with the results of the original model. The computational efficiency is expressed in terms of the total CPU time. Looking at the load-displacement curves shown in Figure 5.16, it can be seen that all of the curves match very well with the original multistringer panel model. However, considering the out-of-plane displacement at a single point at the center of the panel, shown in Figure 5.17, it can be seen that all of the models match well with the original model, except for model 4. In this model, a step time period of 0.25 seconds and a velocity of 16 mm/s are used. It can be seen that the panel buckles in the opposite direction of the original model and the other considered models and does not experience a mode jump. The model gradually changes from five buckling halfwaves in the bays to seven buckling halfwaves. Therefore, it can be said that the solution accuracy for model 4 is lost. However, the solution accuracy for the other models is maintained.

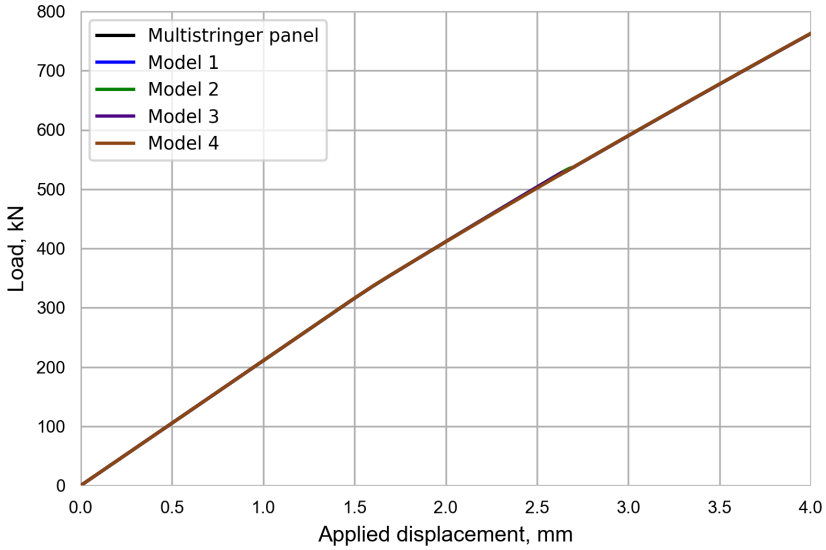

Figure 5.16: Comparison of the load-displacement curves of the multistringer panel model and the different models considered in the dynamic implicit sensitivity study.

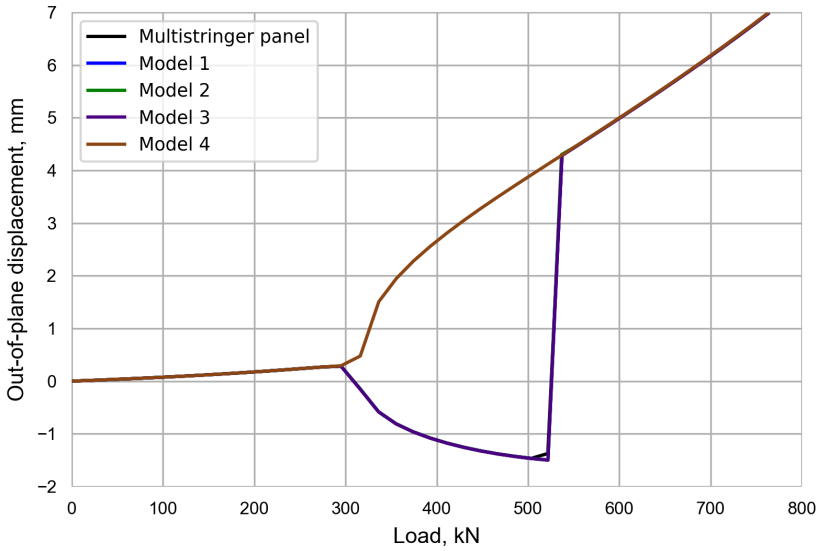

Figure 5.17: Comparison of the out-of-plane displacement of a single point at the center of the panel of the multistringer panel model and the different models considered in the dynamic implicit sensitivity study.

A comparison of the total CPU time of the models is made in Table 5.6. For each of the models, 10 of the following CPUs were used: Intel(R) Xeon(R) CPU E5-2660v3.

Table 5.6: Comparison of the total CPU time required to complete the analysis for the multistringer panel model and the different models considered in the dynamic implicit sensitivity study.

	Total CPU [hrs]	Relative difference
Multistringer panel	15.07	-
Model 1	21.90	45.3%
Model 2	14.95	-0.8%
Model 3	29.32	94.6%
Model 4	4.95	-67.2%

With an increase in velocity and consequently a decrease in step time period, the total CPU time decreases and vice versa. The relative difference in CPU time between the multistringer panel model and model 1 is large. This is the result of applying half of the original velocity. However, when comparing the multistringer panel with model 2, in which the original velocity is doubled, the decrease in CPU time is very small, merely -0.8%. Therefore, it seems that decreasing the applied velocity significantly increases the CPU time, while increasing the velocity influences the CPU time way less. An exception to this trend is model 4. Here, a velocity of -16 mm/s is applied, which is four times the original velocity of -4 mm/s. The difference in CPU time is -67.2%, which is quite significant. However, when looking at the out-of-plane displacement curve of a single point shown in Figure 5.17, it can be observed that this lower CPU time is mainly caused by the fact that there is no mode jump in this model. Since a mode jump is a dynamic instability, Abaqus requires more iterations and increments to capture it. The decrease in CPU time is therefore due to the lower number of increments required. It can be concluded that the solution accuracy for all the models is maintained, except for model 4. It would be most efficient to use model 2 instead of the original model. However, the difference in accuracy and CPU time between these two is so small, that using one over the other will not make a big impact on the results and the computational efficiency.

5.4.2 Mesh Sensitivity Analysis

In order to evaluate the effect of the mesh size on the solution accuracy and the computational efficiency, the multistringer panel is compared to a model with a finer mesh and a model with a coarser mesh. As described in section 5.1, the mesh of the multistringer panel model is uniform with square elements with an approximate size of 2.54 mm by 2.54 mm. A comparison of the mesh size and total number of elements between the models can be seen in Table 5.7.

Table 5.7: Comparison of the mesh size of the multistringer panel model and the models considered in the mesh sensitivity analysis.

Model	Element size [mm x mm]	Total elements [-]	Relative difference
Multistringer panel	2.54 x 2.54	297209	-
Coarse model	3.0 x 3.0	230182	-22.6%
Fine model	2.0 x 2.0	450094	51.4%

A comparison is made in terms of load-displacement curve, out-of-plane displacement of a single point and the total CPU time. From Figure 5.18, it becomes clear that the load-displacement curves match well between the models.

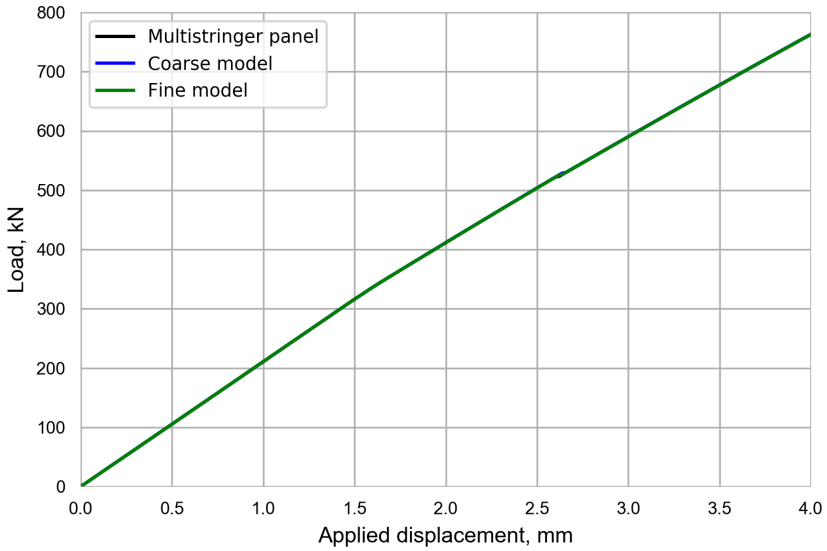

Figure 5.18: Comparison of the load-displacement curves of the multistringer panel model and the different models considered in the mesh sensitivity study.

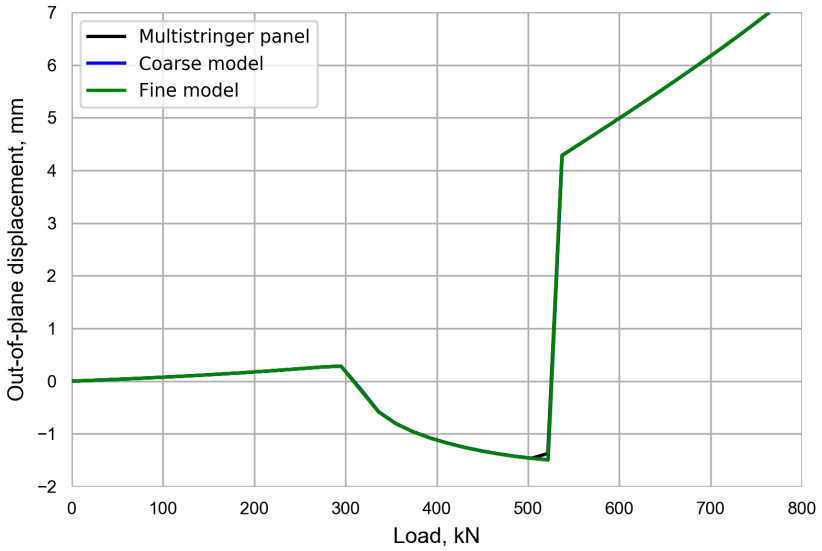

Figure 5.19: Comparison of the out-of-plane displacement of a single point at the center of the panel of the multistringer panel model and the different models considered in the mesh sensitivity study.

Next to that, the out-of-plane displacement at the center point and the buckling mode shape also matches well between the models, see Figure 5.18. This confirms that the mesh used in the original model was sufficiently fine to provide accurate results and that using a slightly coarser mesh does not lead to a loss in solution accuracy.

Finally, considering the total CPU time, it can be seen in Table 5.8 that the total number of elements in a model affects the CPU time considerably. An increase in number of elements, therefore a finer mesh, leads to an increase in total CPU time and vice versa. For these analyses, 10 of the following CPUs were used: Intel(R) Xeon(R) CPU E5-2660v3.

Table 5.8: Comparison of the total CPU time required to complete the analysis for the multistringer panel model and the different models considered in the mesh sensitivity study.

	Total CPU [hrs]	Relative difference
Multistringer panel	15.07	-
Coarse model	11.54	-23.4%
Fine model	27.08	79.7%

5.4.3 Imperfection Sensitivity Analysis

A sensitivity analysis with respect to geometric imperfections is performed. The imperfections that are applied are scaled eigenmodes of the multistringer panel, obtained from the linear eigenvalue analysis, see section 5.2. On one hand, the effect of the magnitude is investigated by applying the first eigenmode as an imperfection with different amplitudes: 0.1 mm, -0.1 mm and 1.0 mm. On the other hand, the effect of different eigenmodes with the same amplitude is studied. The first, second and third buckling eigenmodes of the multistringer panel are applied as geometric imperfections with a magnitude of 0.1 mm. An overview of the models can be seen in the table below, Table 5.9.

Table 5.9: Comparison of the geometric imperfections applied in each of the models considered in the imperfection sensitivity analysis.

Model	Eigenmode [-]	Amplitude [mm]
Multistringer panel	-	-
M1 0.1	First eigenmode	0.1
M1 -0.1	First eigenmode	-0.1
M1 1.0	First eigenmode	1.0
M2 0.1	Second eigenmode	0.1
M3 0.1	Third eigenmode	0.1

Looking at the load-displacement curves of the models, shown in Figure 5.20, it can be seen that neither the amplitude nor the mode shape of the imperfection has a significant effect. The load-displacement curves of the models match well with the original panel model, indicating that the global stiffness of the panel is not significantly affected by geometric imperfections.

This is because the eigenmodes of the multistringer panel are mostly in the central bay. Therefore, by applying a scaled eigenmode, the panel behaviour is only partially affected.

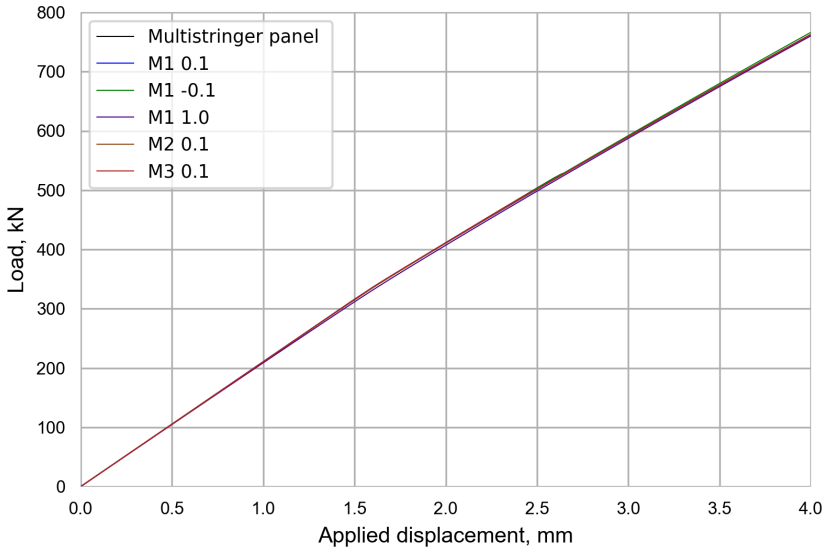

Figure 5.20: Comparison of the load-displacement curves of the multistringer panel model and the different models considered in the imperfection sensitivity study.

Considering the out-of-plane displacements of the models at an applied displacement of 2.2 mm, when the buckling shape is fully developed in all of the bays, it can be seen that the applied geometric imperfection significantly affects the buckling mode shape in the central bay, see Figure 5.21. This is very important to keep in mind, as a different buckling mode shape can change the critical locations; the locations were skin-stringer separation may initiate.

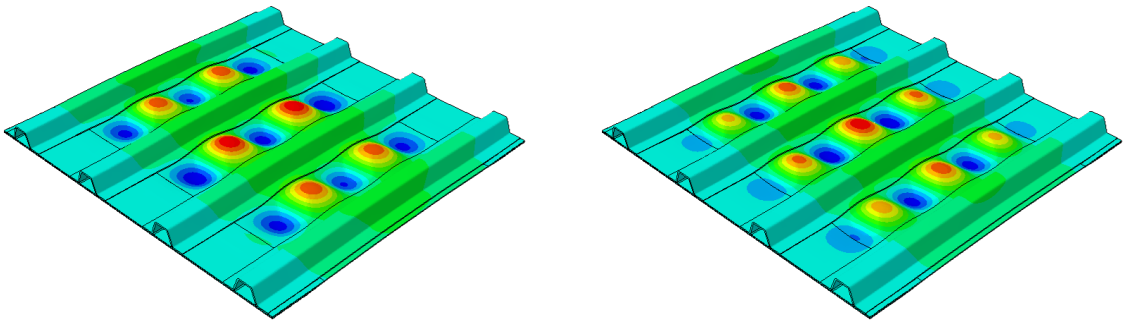

(a) No imperfections.

(b) First eigenmode with an amplitude of 0.1 mm.

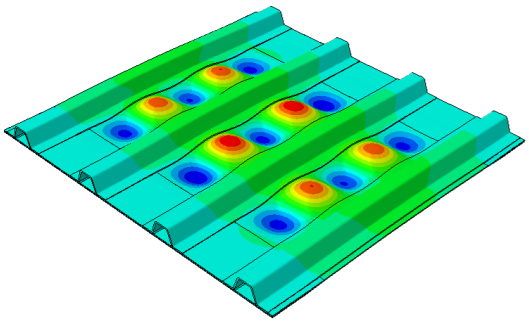

(c) First eigenmode with an amplitude of -0.1 mm.

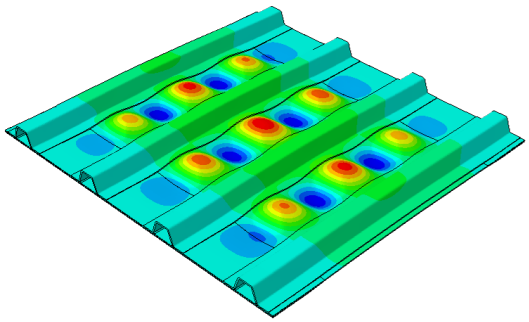

(d) First eigenmode with an amplitude of 1.0 mm.

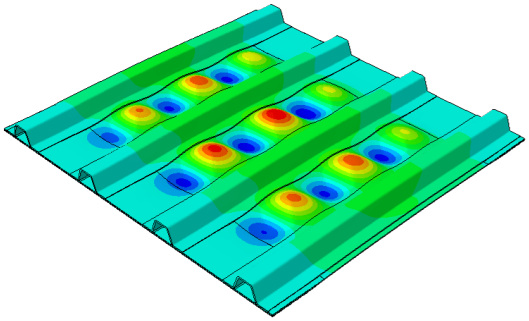

(e) Second eigenmode with an amplitude of 0.1 mm.

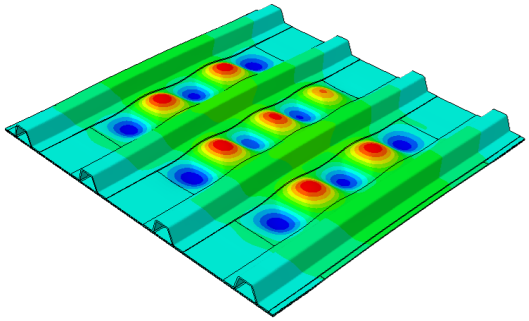

(f) Third eigenmode with an amplitude of 0.1 mm.

Figure 5.21: Comparison of the buckling shape of the multistringer panel and the models considered in the imperfection sensitivity analysis at an applied displacement of 2.2 mm, deformation scale factor = 10.

Chapter 6

From the Multistringer Panel to Single Stringer Specimens

In this chapter, the critical locations where skin-stringer separation is expected to occur are identified on the multistringer panel. Based on the study by Kootte et al. [32], structural sub-elements are designed to represent these critical regions. The buckling mode shape of the multistringer panel is enforced on the sub-elements to perform detailed damage analyses. Doing so, the computational, manufacturing and testing expenses are reduced compared to the analysis and testing of the multistringer panel itself. The critical regions correspond to locations where maximum skin bending and maximum skin twisting occur. At locations of maximum bending, the skin and stringer will separate mainly in mode I, while at the location of maximum twisting, it is expected that skin-stringer separation occurs in a combination of mode II and mode III. Based on the deformation of the multistringer panel in these regions, single stringer specimens can be sized and a transverse loading configuration can be determined such that the buckling mode shape in the critical regions is enforced on the single stringer specimens. For the critical region corresponding to maximum bending, a seven point bending (7PB) specimen can be designed, in which a mode I skin-stringer separation is promoted. For the region where maximum twisting occurs, a four point twisting (4PT) specimen can be designed, in which a mode II+III separation is promoted.

6.1 Critical Locations of the Multistringer Panel

The critical regions are identified based on the post-buckling deformation of the panel. First, the region where the out-of-plane displacement of the skin is minimum is investigated. This is where maximum skin bending occurs. The skin buckles away from the stringer, promoting skin-stringer separation. The separation is mostly dominated by opening of the interface, mode I, and to a lesser extend by in-plane shearing of the interface, mode II. Another region where skin-stringer separation may occur is at the inflection point of a buckling wave [25, 32, 63, 64]. Here, the skin twists, promoting a shearing separation, mode II (in-plane) and

mode III (out-of-plane), at the skin-stringer interface. This kind of separation can be more critical than the mode I dominated separation in panels where the bending stiffness mismatch of the skin and stringer is low [32]. In this section, both the region of minimum out-of-plane displacement and the region of maximum skin twisting are identified and verified.

As explained in chapter 5, the multistringer panel buckles at an applied displacement of approximately 1.5 mm. In all of the bays, five buckling halfwaves develop. However, at an applied displacement of approximately 2.6 mm, the multistringer panel experiences a mode jump, in which the buckling mode of all the bays suddenly changes from five to seven buckling halfwaves. This sudden change makes the determination of the critical locations challenging. To demonstrate this, the minimum out-of-plane displacement of the multistringer panel is considered throughout the non-linear buckling analysis in Figure 6.1. It can be seen that, throughout the analysis, the location where the minimum occurs, changes.

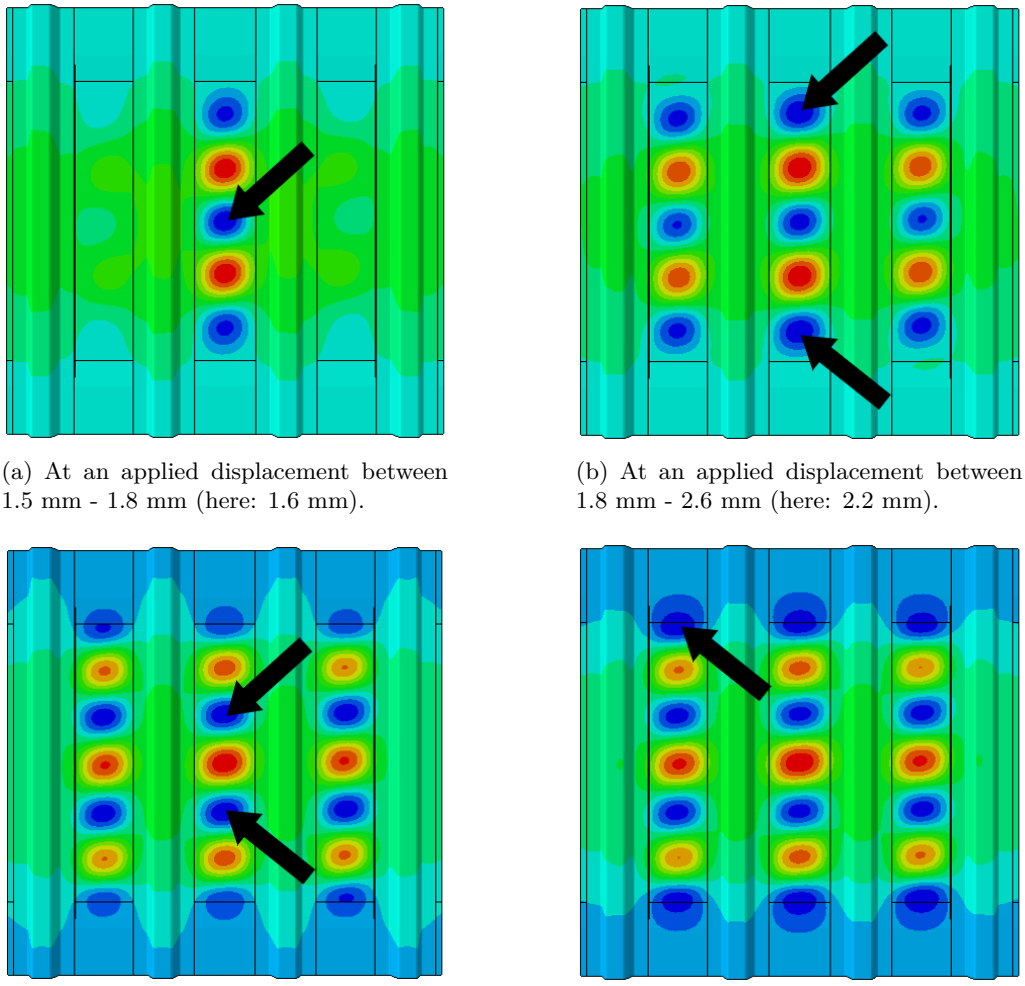

(a) At an applied displacement between 1.5 mm - 1.8 mm (here: 1.6 mm).

(b) At an applied displacement between 1.8 mm - 2.6 mm (here: 2.2 mm).

(c) At an applied displacement between 2.6 mm - 3.1 mm (here: 2.7 mm).

(d) At an applied displacement > 3.1 mm (here: 3.5 mm).

Figure 6.1: Location of the minimum out-of-plane displacement of the skin in the multistringer panel throughout the non-linear buckling analysis.

Between an applied displacement of 1.5 mm and 1.8 mm, the minimum out-of-plane displacement is located in the central bay, at the central buckling halfwave, as shown in Subfigure 6.1(a). However, between an applied displacement of 1.8 mm and 2.6 mm, right before the mode jump, the location of the minimum changes from the center to the buckling halfwaves near the pad-up regions of the skin, see Subfigure 6.1(b). Then, the mode jump occurs and between an applied displacement of 2.6 mm and 3.1 mm, the location of the minimum changes to the buckling halfwaves next to the center, as can be seen in Subfigure 6.1(c). Finally, at an applied displacement greater than 3.1 mm, the minimum out-of-plane displacement is near the pad-up regions in the outer bays, see Subfigure 6.1(d). This clearly demonstrates that determining the critical locations of the multistringer panel is not straight-forward.

First of all, the boundary regions are ignored. It is assumed that the minima near the pad-up regions are the result of boundary effects and the stress redistribution caused by the pad-up regions and potting. Therefore, to determine the critical locations in the multistringer panel, only the central part of the panel, unaffected by boundary effects, is considered. Nevertheless, there are still two possible scenarios that remain. Either, the skin-stringer separation initiates before the mode jump, meaning that the buckling mode shape before the mode jump (five halfwaves in all the bays) is critical, or, skin-stringer separation initiates after the mode jump and then the buckling mode shape after the mode jump (seven halfwaves in all the bays) is critical. Before the critical locations can be determined and the single stringer specimens can be designed, it must be found out which buckling mode shape is critical. Intuitively, it can be said that some damage will occur during the mode jump, due to the transient nature of this instability. However, if damage has already initiated before the mode jump, the initial buckling mode shape of five buckling halfwaves is more critical. Here, it is assumed that skin-stringer separation initiates before the mode jump. Therefore, only the buckling mode shape of the multistringer panel before the mode jump will be considered when determining the critical locations. In Figure 6.2, the critical buckling mode shape of five buckling halfwaves, with the minimum out-of-plane displacement at the center of the panel, can be seen. Since the regions affected by boundary effects are ignored, only the non-shaded part in this figure is considered for the determination of the critical locations.

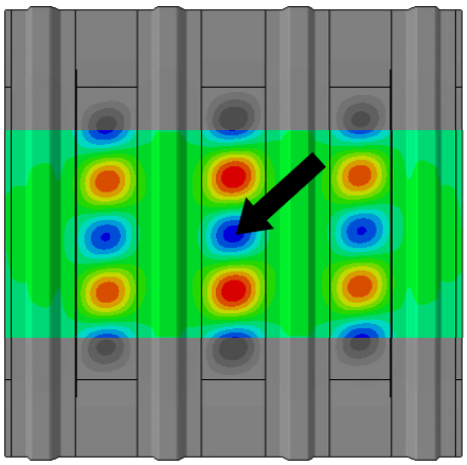

Figure 6.2: The assumed critical buckling mode shape before the mode jump with an indication of the location of the minimum out-of-plane displacement.

As mentioned before, at locations where bending of the skin is maximum, skin-stringer separation is expected mainly in mode I. Furthermore, at locations where the skin twists, skin-stringer separation is expected in a combination of mode II and mode III. Therefore, to determine where skin-stringer separation may initiate, the location of the minimum out-of-plane displacement and the location of the inflection point need to be identified. To do so, the boundary regions are ignored and the buckling mode shape in the range of 1.5 mm - 2.6 mm applied displacement is considered.

The out-of-plane displacements of the skin along the stringer flange edge are considered, as this is where skin-stringer separation will initiate. The location of the minimum out-of-plane displacement is obtained by taking the first derivative of the out-of-plane displacement with respect to the location along the stringer flange edge. To pinpoint the minimum, the location where the sign of the first derivative changes from a negative value to a positive value is found. Similarly, to find the inflection point, the location where the second derivative of the out-of-plane displacement with respect to the location along the stringer flange edge changes sign, is obtained. It is important to take into account that as the magnitude of the buckling mode increases at higher applied displacements, the location of the minimum and the inflection point may change. Therefore, the out-of-plane displacements along the stringer flange edge for the entire range of applied displacements need to be considered. This can be seen in Figure 6.3. It becomes clear that in the range of 1.5 mm - 2.6 mm applied displacement, the location of the minimum stabilizes to a value of 371 mm. At an applied displacement of 2.6 mm, there seems to be a shift to the left in the buckling mode shape, causing the location of the minimum to move towards the left as well. However, as this is right before the mode jump, the buckling mode shape at this displacement is ignored in the determination of the critical location, assuming that this shift is a precursor of the mode jump.

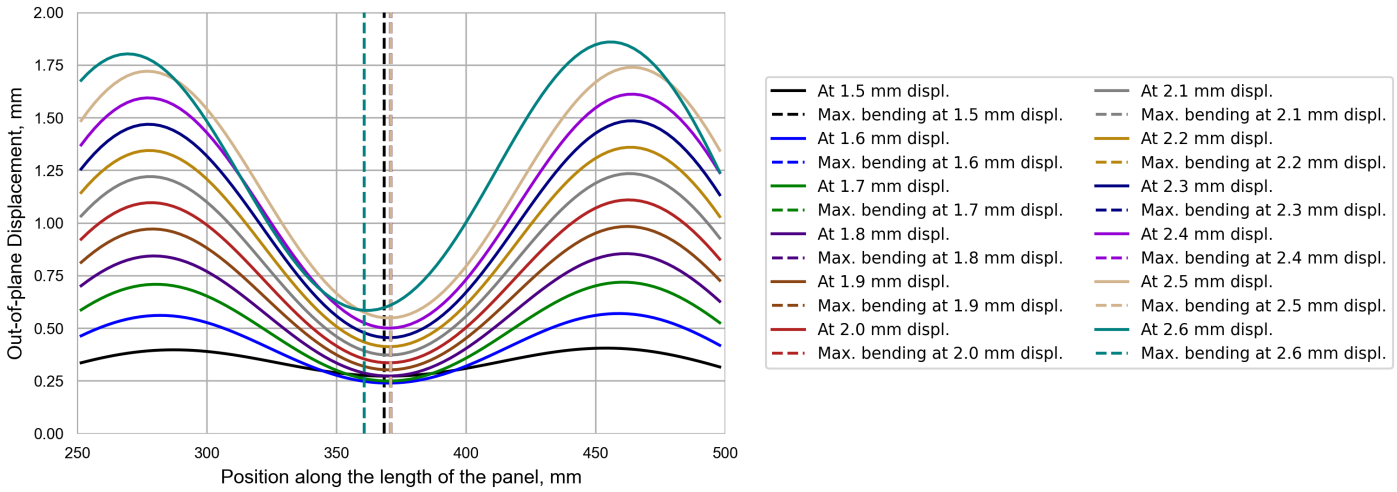

Figure 6.3: Out-of-plane displacements of the skin of the multistringer panel along the stringer flange edge at different applied in-plane displacement values to determine the location of maximum skin bending.

Similarly, in Figure 6.4, the location of the inflection point for every considered applied displacement value is indicated. Here, it can be seen that the location of the inflection point stabilizes to a value of 419 mm. The buckling mode shape at an applied displacement of 2.6

mm is ignored here as well, as it is assumed to be influenced by the mode jump.

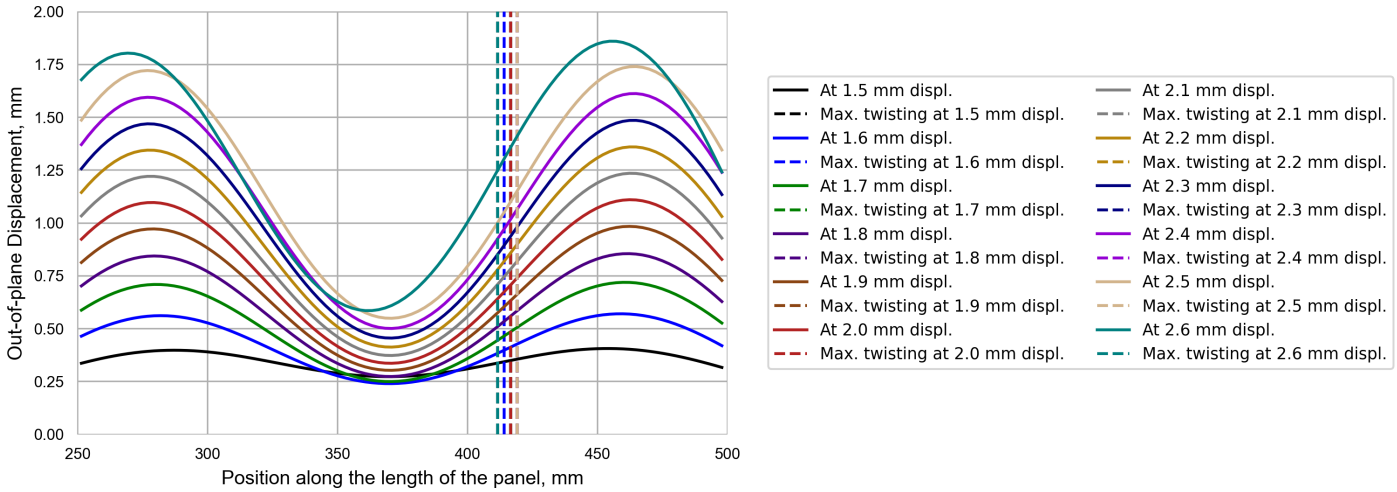

Figure 6.4: Out-of-plane displacements of the skin of the multistringer panel along the stringer flange edge at different applied in-plane displacement values to determine the location of maximum skin twisting.

With this analysis, the critical location for maximum skin bending and maximum skin twisting are determined. The critical location for maximum skin bending is at 371 mm along the panel length and the critical location for maximum skin twisting is at 419 mm along the panel length. Furthermore, it is verified that these locations remain critical in the considered range of applied displacements. To size the 7PB and 4PT specimen, the buckling mode shape at an applied displacement at which skin-stringer separation is expected to occur in the multistringer panel, must be considered. It is assumed that skin-stringer separation initiates only after all bays have buckled. Furthermore, due to the difference in material and layup between the skin and the stringer flanges, it is assumed that there is a bending mismatch between the two. This indicates that it is likely that the mode I dominated separation occurring at locations of maximum bending is more critical than the combined mode II and mode III separation occurring at the buckling wave inflection points. However, it also becomes clear that at applied displacements larger than 2.1 mm, the location of the minimum and the location of the inflection point remain approximately the same, as well as the buckling mode. Therefore, for the sizing of the 7PB specimen, the buckling mode shape at an applied displacement of 2.2 mm is used, as at this displacement the buckling mode shape in all of the bays has fully developed and the location of the minimum has stabilized. For the sizing of the 4PT specimen, the buckling mode shape at an applied displacement of 2.5 mm is used. Similar as for the 7PB specimen, at this displacement all of the bays are fully buckled and the location of the inflection point has stabilized. A higher applied displacement value compared to the 7PB specimen is selected, as it is expected that skin-stringer separation at the inflection point will be non-critical and will initiate only after damage has already initiated at the location of maximum skin bending. It should be emphasized that this is an approximation. After sizing and placing the indenters in an optimal configuration, it should be verified whether the obtained specimen size and loading configuration can accurately represent the buckling deformation of the multistringer panel in the range of 1.5 mm - 2.6 mm applied displacements.

6.2 Design of the Single Stringer Specimens

Using the buckling mode shape of the multistringer panel near the critical locations, a critical region in the multistringer panel and the corresponding single stringer specimen are sized, and the positions of the indenters are determined. The single stringer specimen needs to be such that the interaction between the post-buckling shape and the skin-stringer separation at the critical location is accurately represented.

6.2.1 Methodology

The method developed by Kootte et al. [32] is used to determine the size of the critical regions in the multistringer panel and of the single stringer specimens, as well as the positions of the indenters, such that the out-of-plane deformation of the specimens represents the out-of-plane deformation in the critical regions of the multistringer panel as well as possible.

First, the size of the critical regions and the specimens is determined based on the out-of-plane displacements of the skin in the multistringer panel near the critical locations. Doing so, it is important that the critical location is included entirely and that the size is large enough to remove any undesired boundary effects. Then, numerical models for the 7PB and 4PT specimens are set up. Both models contain a skin with a single stringer. The layup of the skin and stringer are the same as for the multistringer panel, see section 3.1. The mesh of the single stringer specimens is uniform and is slightly finer than the mesh of the multistringer panel model, to avoid convergence issues related to the contact interaction between the skin and the indenters. The mesh is approximately 2 mm x 2 mm everywhere. The skin, interior wrap and overwrap are meshed with SC8R elements, while the noodle region is meshed with C3D8R elements. The skin and stringer are tied together using a tie constraint and no cohesive elements and/or other damage models are included.

Two types of indenters are distinguished: supporting indenters and loading indenters. The former are positioned underneath the specimen, at the skin side, while the latter apply a transverse displacement to the top of the specimen, at the stringer side. The supporting indenters remain stationary throughout the analyses. The loading indenters are free to displace along the z-direction (out-of-plane) to apply the transverse displacement.

Then, a Python tool developed by Kootte et al. [32] is used to determine the optimal position of the supporting and loading indenters. First, the out-of-plane displacements in the critical regions of the multistringer panel are obtained. Then, the tool iterates through different loading and supporting indenter positions and sets up an input file for each configuration. The displacement applied to the loading indenters is determined based on the out-of-plane displacements of the multistringer panel: the single stringer specimen is positioned such that it hypothetically overlaps with the critical region of the multistringer panel and depending on the position of the loading points, the corresponding out-of-plane displacement at these points in the multistringer panel are taken as the applied displacement value. To do so, it is first ensured that the point corresponding to the center of the single stringer specimen in the multistringer panel is at zero displacement. After completing the analysis, the out-of-plane displacements of the single stringer specimens are compared to the out-of-plane displacements of the corresponding region in the multistringer panel. A shape error is calculated and the

configuration with the lowest shape error is taken as the optimal. The shape error for each configuration is calculated using the Residual Sum of Squares (RSS), see Equation 6.1.

$$RSS = \sum_{i=1}^{n} \Big(y_i - f(x_i) \Big)^2 \tag{6.1}$$

Here, y_i corresponds to the out-of-plane displacement of a single point in the multistringer panel, while $f(x_i)$ is a linearly interpolated function of the out-of-plane displacement in the single stringer specimens. By doing so, the mesh of the single stringer specimen does not need to match the mesh of the multistringer panel. The configuration corresponding to the minimum value of the RSS is then determined to be the optimal configuration.

6.2.2 Seven Point Bending Specimen

The out-of-plane displacements in the region near maximum bending are approximated by a single stringer specimen in a 7PB configuration. Specifically, this means that the specimen is loaded by two loading indenters at the top side of the specimen (the stringer side), while being supported by five indenters at the bottom side of the specimen (the skin side). First, the size of the 7PB specimen and the corresponding critical region in the multistringer panel are determined based on the buckling mode shape of the multistringer panel near the critical location. Then, using the methodology described in subsection 6.2.1, the optimal positions of the loading and supporting indenters are determined, such that the out-of-plane displacements in the critical region of the multistringer panel are accurately reproduced on the single stringer specimen.

Sizing of the Seven Point Bending Specimen

The buckling mode shape at an applied in-plane displacement of 2.2 mm is considered for the sizing of the 7PB specimen. At this displacement, the buckling mode shape has fully developed in all of the bays and the location of the minimum out-of-plane displacement has stabilized to a value of $x = 371$ mm.

In Figure 6.5, the out-of-plane displacements of the skin of the multistringer panel at $x = 371$ mm, along the width of the panel, can be seen (Subfigure 6.5(a)), as well as the out-of-plane displacements of the skin of the multistringer panel along the stringer flange edge (Subfigure 6.5(b)). The size of the 7PB specimen and the critical region in the multistringer panel are based on these displacements. For the sizing, it is important that the critical area is fully captured. Furthermore, the indenters should not be placed within 20 mm of the edges of the specimen. This is to avoid stress concentrations there. This is important to consider for the sizing of the 7PB specimen since the five supporting indenters are fixed at the same height. This means that placing the corner indenters at points corresponding to the maxima of the out-of-plane displacement (as seen in Subfigure 6.5(b)) is not an option, because then the central supporting indenter cannot be at the same height as the corner indenters. Therefore, the corner indenters should be placed near locations corresponding to the inflection points in the multistringer panel. Here, the relative displacement with respect to the point corresponding to the central support is small. The loading indenters however,

can be placed at points corresponding to the minima of the out-of-plane displacement. All of this needs to be taken into account when sizing the critical region and the 7PB specimen.

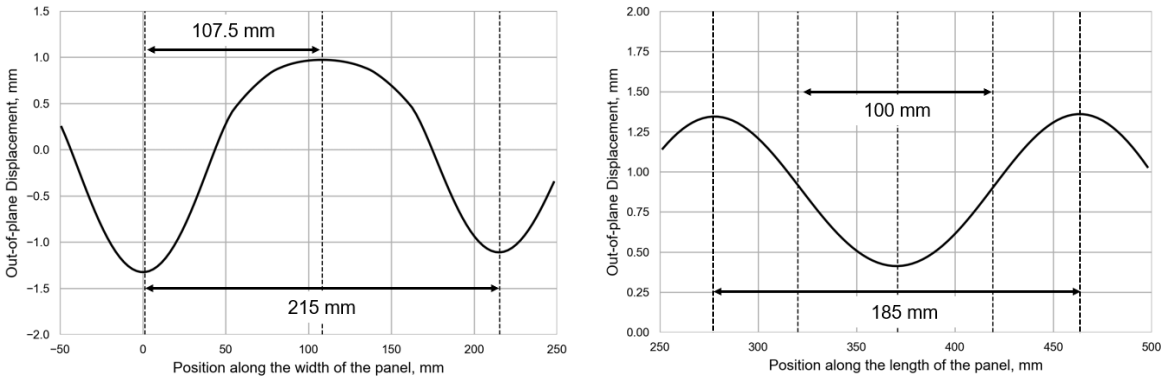

(a) Along the y-direction at the location of maximum bending.

(b) Along the stringer flange edge.

Figure 6.5: Out-of-plane displacements of the skin of the multistringer panel at an applied in-plane displacement of 2.2 mm, used for the sizing of the critical region and the 7PB specimen.

Considering the width (along the y-direction), the loading indenters can be positioned as far as the minima on each side of the stringer in the multistringer panel. In Subfigure 6.5(a), it is shown that the distance between the minima on either side of the stringer is 215 mm. As mentioned before, the indenters cannot be placed within 20 mm from the free edges. Therefore, 20 mm of width is added on each side. This results in a final width of the 7PB specimen of 255 mm. For the length (along the x-direction), different options can be considered. Considering Subfigure 6.5(b), it can be seen that the distance between the inflection points in the multistringer panel is approximately 100 mm. Next to that, the distance between the maxima of the out-of-plane displacement is approximately 185 mm. Two different lengths are considered. First, a length of 140 mm is considered (7PB/v1). This comes from the requirement that the supporting indenters should be placed near points corresponding to the inflection points in the multistringer panel and at least 20 mm away from the free edges. Since the distance between the inflection points is approximately 100 mm, this leads to a length of 140 mm. Another possibility is taking the length such that the maxima of the out-of-plane displacements are also included. This is to ensure that any possible influence of these regions on the deformation of the specimen is taken into account. As mentioned before, the supporting indenters cannot be placed at points corresponding to the maxima. Therefore, there is no need to add an additional 40 mm in length. This leads to a length of 185 mm (7PB/v2).

So, the final dimensions of 7PB/v1 are 140 mm x 255 mm. The critical region in the multistringer panel corresponding to this can be seen in Subfigure 6.6(a). The final dimensions of 7PB/v2 are 185 mm x 255 mm. The critical region in the multistringer panel corresponding to this can be seen in Subfigure 6.6(b).

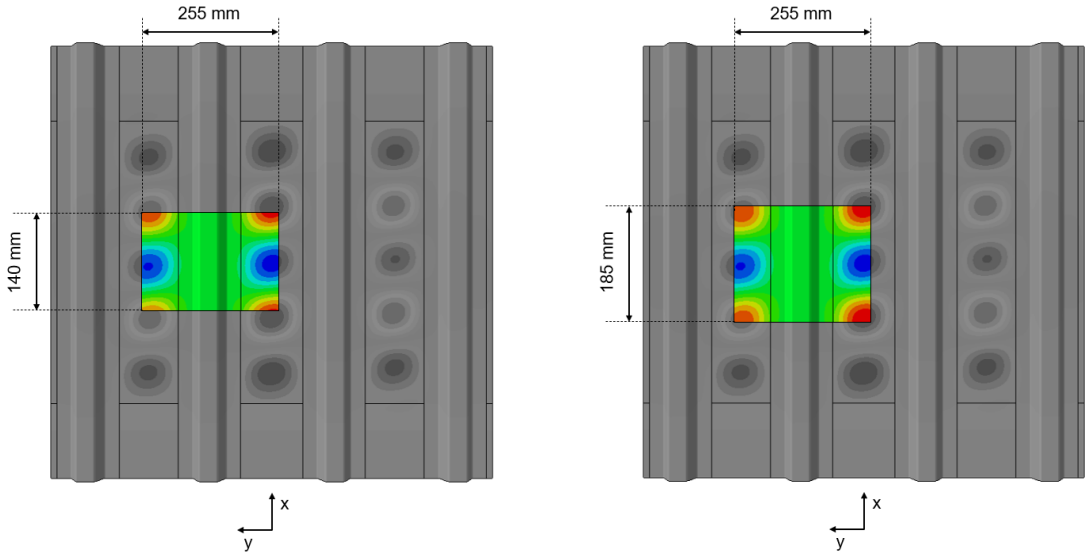

(a) 7PB/v1: 140 mm x 255 mm.

(b) 7PB/v2: 185 mm x 255 mm.

Figure 6.6: The critical region of the multistringer panel that will be captured by the 7PB specimen.

Indenter Positions of the Seven Point Bending Specimen

After the 7PB model is set up, the Python tool iterates through different indenter positions to try to minimize the shape error between the 7PB specimen and the critical region in the multistringer panel. Four different variables are defined when considering the location of the indenters on the 7PB specimen. Considering Figure 6.7, it can be seen that the position of the supporting indenters in the corners of the specimen are dictated by the variables S_x and S_y. The position of the loading indenters are dictated by the variables L_x and L_y.

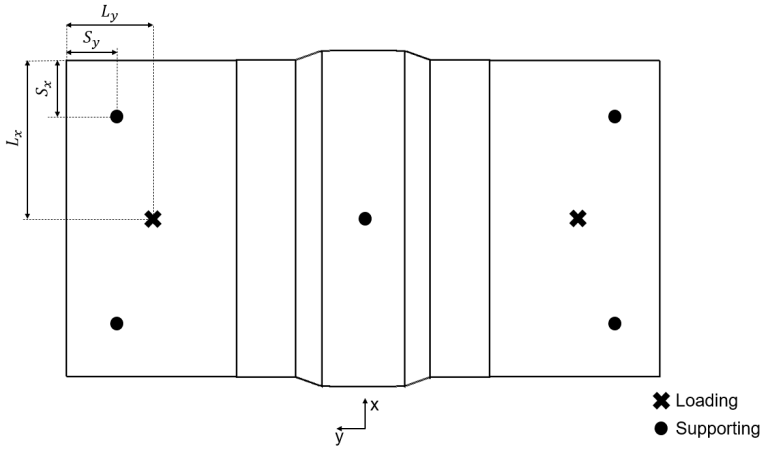

Figure 6.7: 7PB configuration and definitions of the position variables.

To limit the number of possible indenter configurations, several constraints are applied to the

variables:

- The supporting corner indenters are placed symmetrically about both symmetry axes of the specimen.
- Similarly, the loading indenters are also placed symmetrically about both axes. This means that $L_x = \frac{140}{2} = 70$ mm for 7PB/v1 or $L_x = \frac{185}{2} = 92.5$ mm for 7PB/v2.
- The central supporting indenter is placed exactly in the center of the specimen.
- The indenters should not be positioned within 20 mm from all edges. This means $S_x, S_y, L_y \geq 20$ mm.
- The supporting indenters should be placed near points corresponding to the inflection points in the multistringer panel. Therefore, for 7PB/v1, $S_x \approx 20$ mm. For 7PB/v2, $S_x \approx 42.5$ mm.
- The indenters cannot be placed within 15 mm from the stringer flange edge, to avoid premature opening of the skin-stringer interface.

Once the indenter positions are set, a displacement is applied to the loading indenters that is equal to the out-of-plane displacement of the skin in the multistringer panel at the corresponding location. To calculate the shape error, an area of interest is defined. This is the area of the 7PB specimen and the critical region of multistringer panel that will be used in the calculation of the RSS. The effect of the size of this area on the results is investigated. Intuitively, it can be said that a larger area of interest will give a greater shape error because of the free edge effect in the single stringer specimen. Since the edges of the specimen are unconstrained, the displacements of the specimen beyond the corner indenters are unconstrained, resulting in the free edge effect. The free edge effect is shown in Figure 6.8.

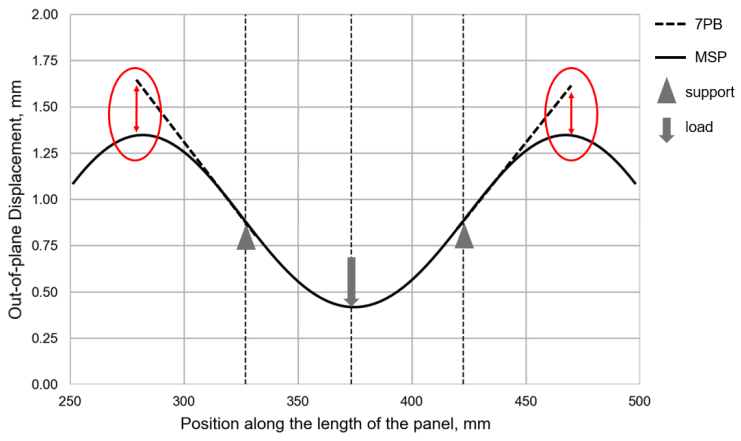

Figure 6.8: Demonstration of the free edge effect in the 7PB specimen.

The solid black curve shows the out-of-plane displacements of the skin of the multistringer panel along the stringer flange edge. The dotted black curve shows the out-of-plane displacements of the skin of a 7PB specimen along the stringer flange edge. The supporting indenters are placed at the inflection points, while the loading indenter is placed at the location of maximum skin bending. It can clearly be seen that beyond the supporting indenters, the free edges are unconstrained and show a larger displacement compared to the multistringer panel. Due to the free edge effect, it is certain that a shape error will exist there. This indicated in red. It is expected that including the free edges into the shape error calculation, will results in a misrepresentation of the out-of-plane

displacement in the region between the corner indenters, which is the most critical region for skin-stringer separation. It should be noted that this figure is for illustrative purposes only and that the curve depicted here for the 7PB specimen is fictional. Including the free edges into the area of interest will intuitively increase the overall shape error between the 7PB specimen and the critical region of the multistringer panel. Nevertheless, this needs to be verified. Therefore, a smaller and a larger area of interest are considered for 7PB/v1.

The small area of interest extends from inflection point to inflection point. The width is taken from the minimum to the center of the specimen. The reason why not the entire width is considered in the area of interest is because of the lack of symmetry in the multistringer panel. The central bay buckles earlier than the outer bays due to its larger size and therefore, develops a buckling mode shape of higher magnitude than the outer bays. However, in the 7PB specimen, a symmetric deformation is enforced on each side of the stringer. To remove the shape error that would result from this, only half of the critical region and the 7PB specimen is considered in the area of interest. Furthermore, 20 mm from the edge is also excluded from the width of the area of interest. This is because in the critical region in the multistringer panel, the skin there will deflect upward again, while in the 7PB specimen this is not the case since the edge is free. The larger area of interest has the same width, but extends over the entire length of the specimen. This way, the free edges are included.

The specimen 7PB/v1 with a smaller area of interest is referred to as 7PB/v1/a, while the specimen with a larger area of interest is referred to as 7PB/v1/b. The critical region of 7PB/v1/a and 7PB/v1/b in the multistringer panel and their corresponding areas of interest can be seen in Figure 6.9.

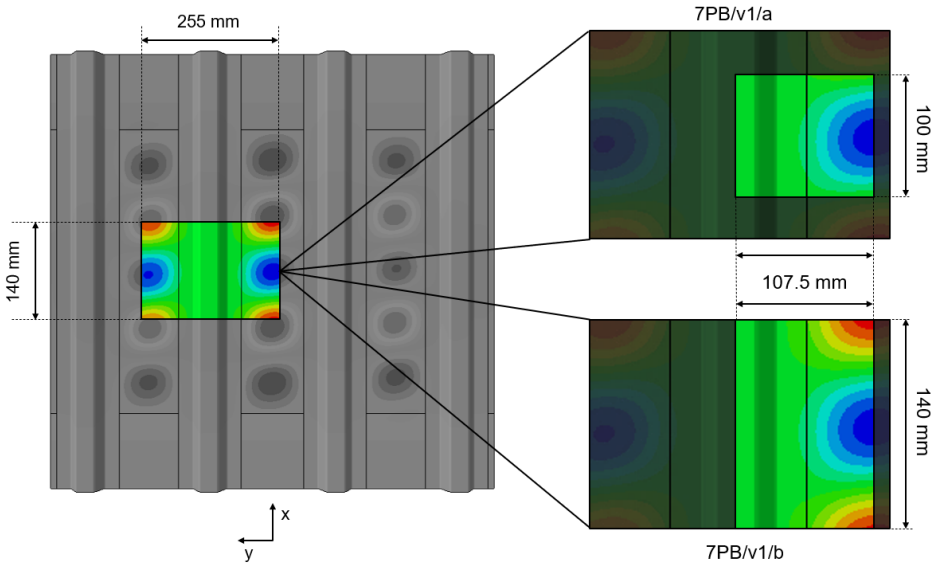

Figure 6.9: The area of interest for the shape comparison with the 7PB specimens, 7PB/v1/a and 7PB/v1/b.

By comparing the results obtained with 7PB/v1/a and 7PB/v1/b, the effect of the size of the area of interest on the results can be derived. For 7PB/v2, only one area of interest is considered, namely the smaller one. This specimen is referred to as 7PB/v2/a. This way, the size of the area of interest is the same for 7PB/v1/a and 7PB/v2/a, making the effect of the specimen size on the results clear. The critical region of 7PB/v2/a in the multistringer panel and its corresponding area of interest can be seen in Figure 6.10.

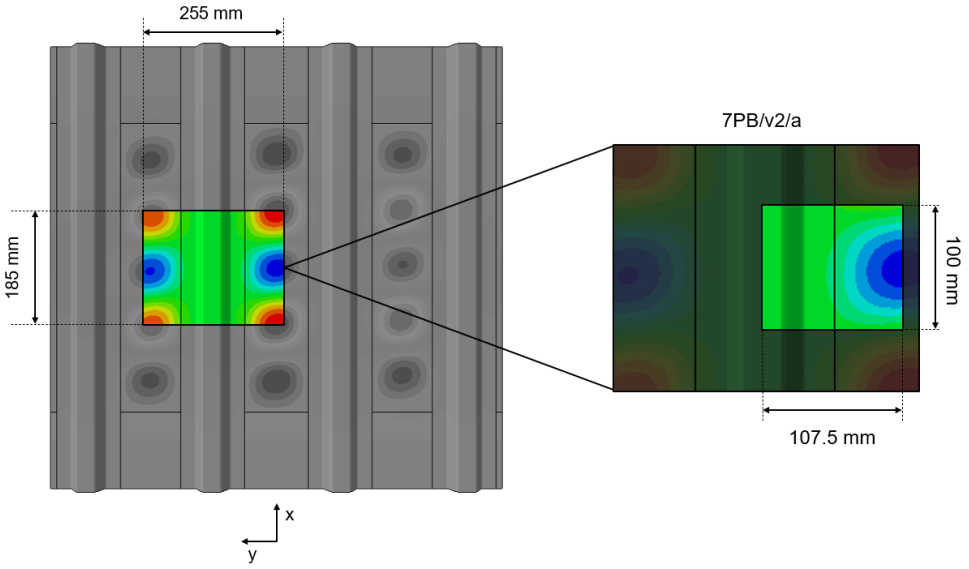

Figure 6.10: The area of interest for the shape comparison with the 7PB specimen, 7PB/v2/a.

An overview of the dimensions of the considered specimens and areas of interest (AoI) can be seen in Table 6.1.

Table 6.1: Considered 7PB specimen designs.

7PB specimen	Length (x) [mm]	Width (y) [mm]	AoI length (x) [mm]	AoI width (y) [mm]
7PB/v1/a	140	255	100	107.5
7PB/v1/b	140	255	140	107.5
7PB/v2/a	185	255	100	107.5

For each of these, the Python tool iterates through possible indenter configurations. The configuration with the lowest shape error (RSS) between the area of interest of the 7PB specimen and the corresponding area of interest of the multistringer panel is selected as the optimal configuration. The absolute magnitude of the RSS is irrelevant, as with a higher number of datapoints involved in the calculation, the value of the RSS increases. This means that with a finer mesh or a larger area of interest, the magnitude of the shape error increases. The relative magnitude is of importance here; the lowest RSS corresponds to the loading configuration that can best represent the buckling mode shape of the multistringer panel in the area of interest. Therefore, the values of the RSS for each of the optimal configurations obtained with the specimens considered in Table 6.1, cannot be directly compared. To make

a valid comparison, the RSS values have to be normalized with respect to the number of datapoints involved in calculation. Only then, the different optimal configurations can be compared and the best performing one can be selected. The optimal indenter configuration for each of the options considered for the 7PB specimen can be seen in Table 6.2. For each, the normalized RSS (NRSS) value is also given.

Table 6.2: Optimal indenter configuration for each of the considered 7PB specimens with their corresponding normalized shape error.

7PB specimen	S_x [mm]	S_y [mm]	L_x [mm]	L_y [mm]	RSS [-]	# datapoints [-]	NRSS [-]
7PB/v1/a	23	25	70	33	360	172000	0.0021
7PB/v1/b	23	32	70	35	806	240800	0.0033
7PB/v2/a	45.3	42	92.5	37	426	172000	0.0025

The contour plots of the 7PB specimens as compared to the critical region in the multistringer panel for the optimal configurations can be seen in Figure 6.11 and Figure 6.12. The contour plots are shown at an applied in-plane displacement of 2.2 mm.

As expected, specimen 7PB/v1/a has the lowest normalized RSS and can thus best represent the deformation in the critical region of the multistringer panel. This is also demonstrated in Figure 6.11.

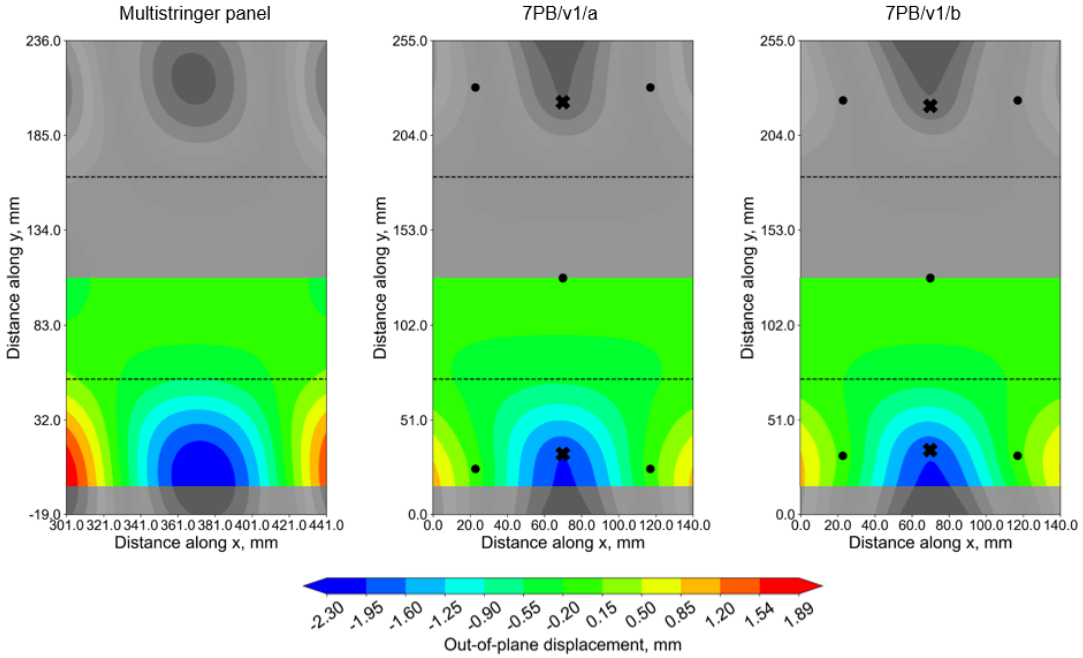

Figure 6.11: Contour plot comparison between the critical region in the multistringer panel at an applied displacement of 2.2 mm and the considered 7PB specimens, 7PB/v1/a and 7PB/v1/b.

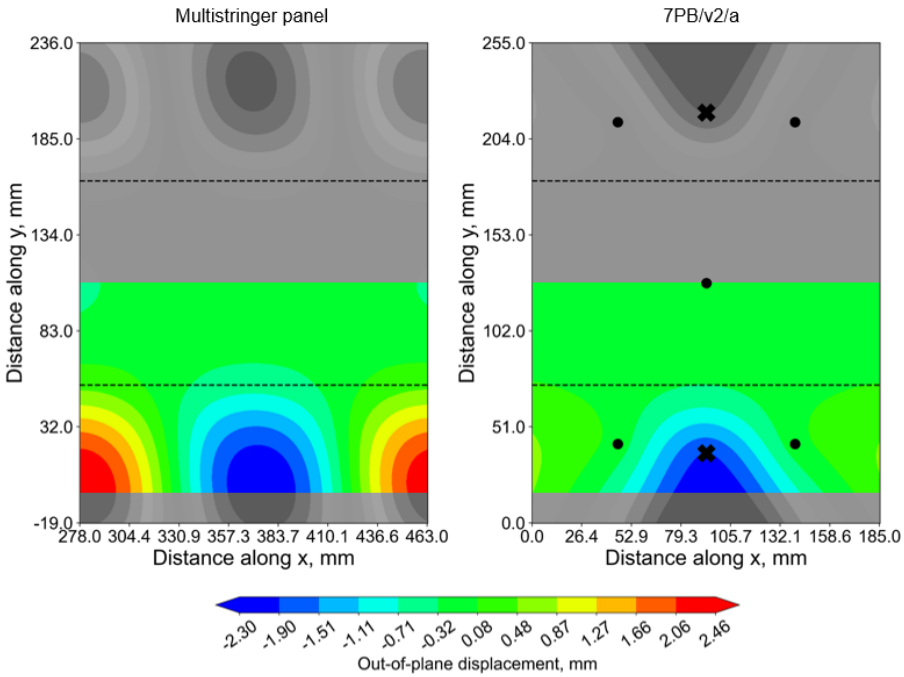

Figure 6.12: Contour plot comparison between the critical region in the multistringer panel at an applied displacement of 2.2 mm and the considered 7PB specimen, 7PB/v2/a.

To confirm this further, the out-of-plane displacements of the skin along the stringer flange edge for each of the considered options, in comparison with the multistringer panel are shown in Figure 6.13.

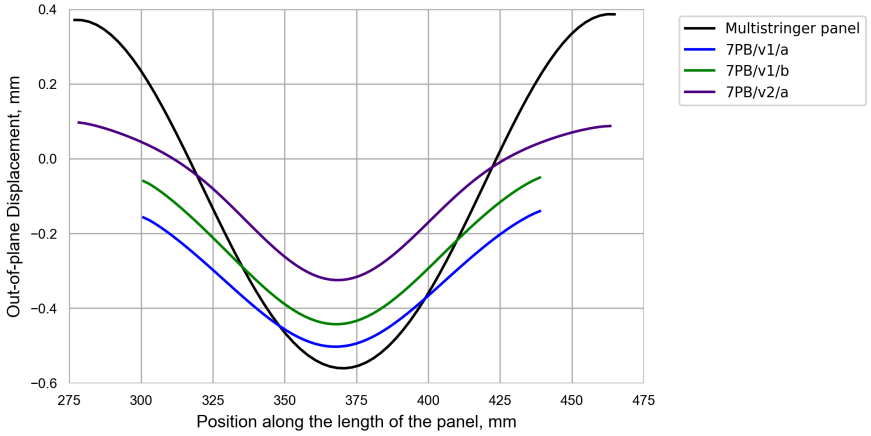

Figure 6.13: Out-of-plane displacements of the skin along the stringer flange edge in the multistringer panel and the considered 7PB specimens.

All of these curves are plotted such that the zero reference point is the same; the point in each corresponding to the central supporting indenter is set to zero out-of-plane displacement. This way, a valid comparison can be made. It is important that the deformation of the multistringer panel is well represented in this region, since this is where skin-stringer separation will initiate.

From the graph, it is confirmed that 7PB/v1/a matches the best with the multistringer panel. By comparing the results of 7PB/v1/a and 7PB/v1/b, the effect of the size of the area of interest can be found. From the results, it can be seen that by including the free edges in the area of interest, the out-of-plane displacements in between the corner indenters are not well represented as shown in Figure 6.13 for 7PB/v2/a. However, by excluding the free edges, as was done in 7PB/v1/a, the out-of-plane displacements match better with what is observed in the multistringer panel. From this, it can be concluded that including the free edges in the shape error calculation will only increase the shape error and will not lead to an accurate representation of the deformation in the multistringer panel near the critical location. Next to that, by comparing 7PB/v1/a and 7PB/v2/a, the effect of the specimen size on the results can be seen. The area of interest has the same size here and the normalized RSS values are close. However, considering the contourplot shown in Figure 6.12 and the out-of-plane displacements of the skin along the stringer flange edge in Figure 6.13, it is clear that the larger specimen 7PB/v2/a does not match well with the multistringer panel. Due to the larger unconstrained region beyond the corner indenters, the free edge effect is more pronounced. Therefore, it is decided that 7PB/v1/a matches best with the multistringer panel in the critical region.

However, a difference in out-of-plane displacement of the skin at the stringer flange edge still exists between 7PB/v1/a and the multistringer panel, considering Figure 6.13, that could lead to discrepancies in the damage initiation and propagation between the two. The difference could be caused by the way that the loading configuration of the 7PB specimen is determined. By minimizing the shape error within the area of interest and consequently by finding a loading configuration based on this, the deformation of the skin along the stringer flange edge could still be misrepresented since the shape error is calculated over a relatively large area. The displacements of the skin there are especially important as these directly drive the skin-stringer separation. An effort can be made to reduce this difference between the curves and improve the design of the 7PB specimen such that it is better representative of the multistringer panel. Therefore, the indenter positions of the 7PB specimen are redetermined using an area of interest that is solely focused on the skin at the stringer flange edge, see Figure 6.14. This way, it is ensured that the displacements there match with the multistringer panel.

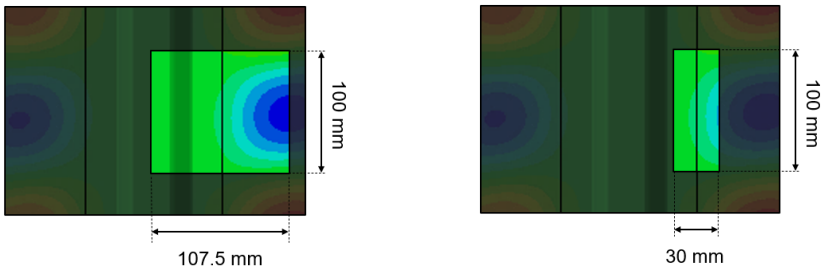

(a) Original area of interest. (b) New area of interest.

Figure 6.14: Comparison of the new area of interest and the original area of interest for the determination of the indenter positions of the 7PB specimen.

For the new 7PB specimen, an area of interest of 100 mm x 30 mm is used, centered at the stringer flange edge. In Subfigure 6.14(a), the original area of interest that was used to

obtain the indenter positions of 7PB/v1/a can be seen. In Subfigure 6.14(b), the new area of interest, only focusing on the skin at the stringer flange edge can be seen. Following the procedure described previously, the new indenter positions can be obtained; the Python tool iterates through different indenter configurations and selects the one for which the Residual Sum of Squares between the 7PB specimen and the multistringer panel, within the area of interest, is minimized. It should be noted that the size of the area of interest is the only aspect that changes. The new 7PB specimen is still designed based on the multistringer panel at an applied in-plane displacement of 2.2 mm, since this is what was initially assumed and the exact point of damage initiation is unknown. The following indenter positions for the new 7PB specimen are obtained, see Table 6.3. The original indenter positions are also reported for comparison purposes. It can be seen that both the loading and supporting indenters have been placed significantly closer to the stringer flange edge than before.

Table 6.3: Comparison of the original indenter positions with the newly obtained indenter positions using a smaller area of interest on the 7PB specimen.

7PB specimen	S_x [mm]	S_y [mm]	L_x [mm]	L_y [mm]
Original	23	25	70	33
New	23	42	70	47

Looking at the out-of-plane displacements of the skin along the stringer flange edge, at an applied in-plane displacement of 2.2 mm, in Figure 6.15, it can be seen that the new 7PB specimen matches better with the multistringer panel than the original 7PB specimen (7PB/v1/a). This shows the effectiveness of using a smaller area of interest to represent the out-of-plane displacements of the skin along the stringer flange edge.

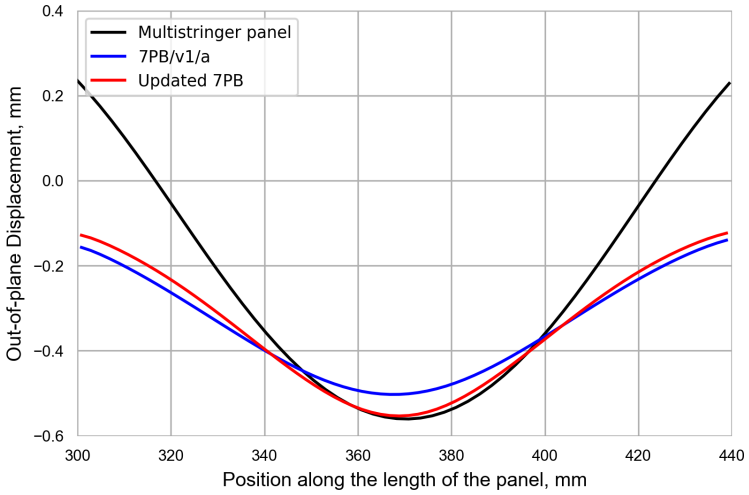

Figure 6.15: A comparison of the out-of-plane displacements of the skin at the stringer flange edge of the new 7PB specimen, the original 7PB specimen and of the multistringer panel at an applied in-plane displacement of 2.2 mm.

A sensitivity analysis is performed to see the effect of using an even smaller area of interest

to obtain the loading configuration of the 7PB specimen. To do so, an area of interest of 100 mm x 10 mm, focused on the skin at the stringer flange edge is used. In Figure 6.16, the out-of-plane displacements of the skin there can be seen for the multistringer panel, the new 7PB specimen and the 7PB specimen with the decreased area of interest, at an applied in-plane displacement of 2.5 mm. From the figure, it is confirmed that the shape of the skin of the new 7PB specimen matches quite well with the multistringer panel. However, for the 7PB specimen using the decreased area of interest, it becomes clear that the shape of the skin is "sharper" towards the minimum; the width of the curve near the minimum is reduced. This will lead to an overprediction of the damage propagation rate and inaccuracies with respect to the shape of the damage front. Furthermore, this sharpness of the skin towards the minimum will only become worse as the applied displacement is increased.

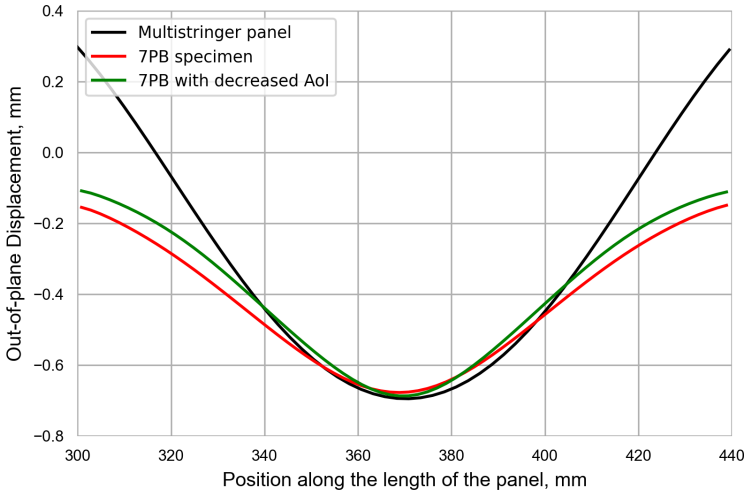

Figure 6.16: Comparison of the shape of the skin at the stringer flange edge for different 7PB specimens and the multistringer panel as a sensitivity analysis on the size of the area of interest.

The sensitivity analysis shows the importance of selecting an appropriate size of the area of interest used in the determination of the loading configuration; it must be small enough such that the out-of-plane displacements of the skin at the stringer flange edge are accurately represented, but large enough to avoid inaccuracies in terms of the shape of the skin near the minimum.

To verify that this new 7PB configuration is able to represent the shape of the multistringer panel at different applied in-plane displacements in the considered range (1.5 mm - 2.6 mm), a comparison between the 7PB specimen and the multistringer panel is also made at a displacement of 1.5 mm, 2.0 mm and 2.5 mm. The contour plots are compared in Figure 6.17. From this, it becomes clear that the overall deformation shape of the 7PB specimen does not match very well with the deformation seen in the multistringer panel. This makes sense since the shape error between the 7PB specimen and the multistringer panel is calculated within an area of interest, which is only a limited part of the specimen and corresponding critical region.

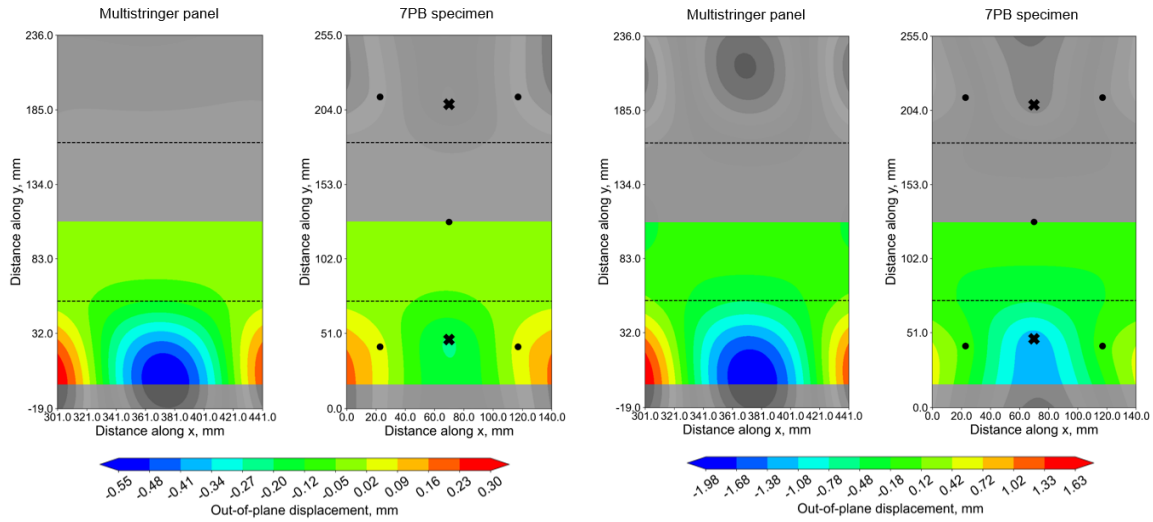

(a) At an applied in-plane displacement of 1.5 mm.

(b) At an applied in-plane displacement of 2.0 mm.

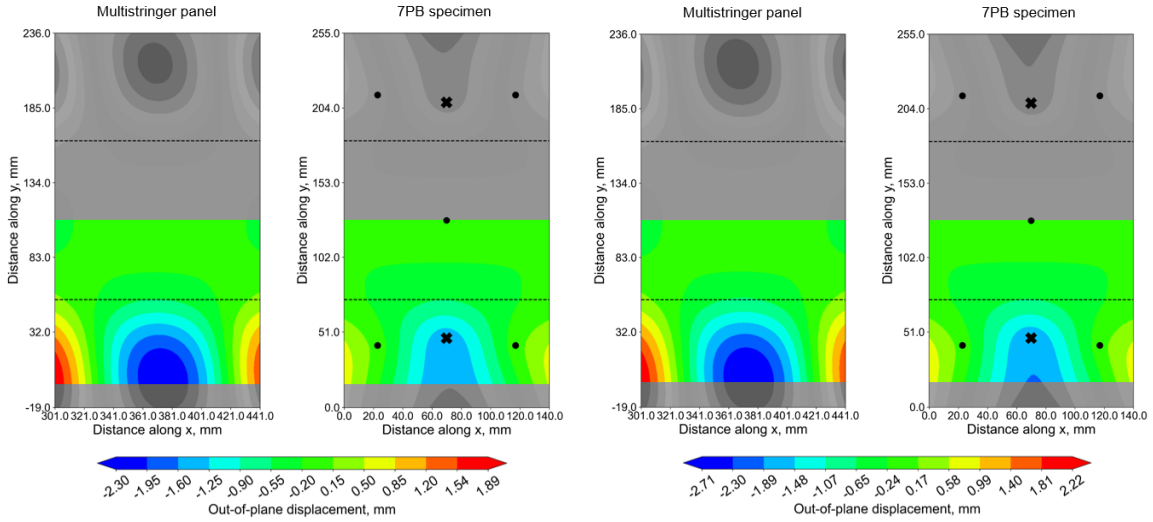

(c) At an applied in-plane displacement of 2.2 mm.

(d) At an applied in-plane displacement of 2.5 mm.

Figure 6.17: Contour plot comparison between the 7PB specimen and the critical region in the multistringer panel throughout the considered range of applied in-plane displacements.

However, considering the out-of-plane displacements of the skin along the stringer flange at the same applied in-plane displacements, shown in Figure 6.18, it can be seen that the 7PB specimen and the multistringer panel match quite well throughout the considered range. It is more important for damage initiation and damage propagation that the out-of-plane displacements along this edge match well than that the overall out-of-plane displacements of the entire 7PB specimen match with the multistringer panel. From the graphs, it can be seen that at an applied in-plane displacement of 1.5 mm, the curves do not match very well. However, it is unlikely that skin-stringer separation will initiate right after buckling, so the difference between the curves there is acceptable.

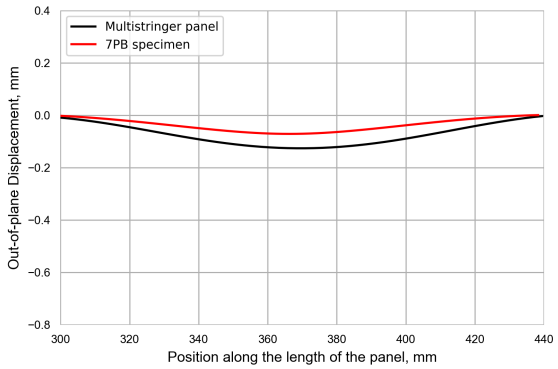

(a) At an applied in-plane displacement of 1.5 mm.

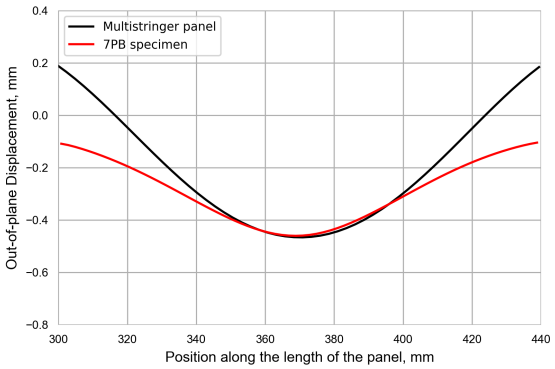

(b) At an applied in-plane displacement of 2.0 mm.

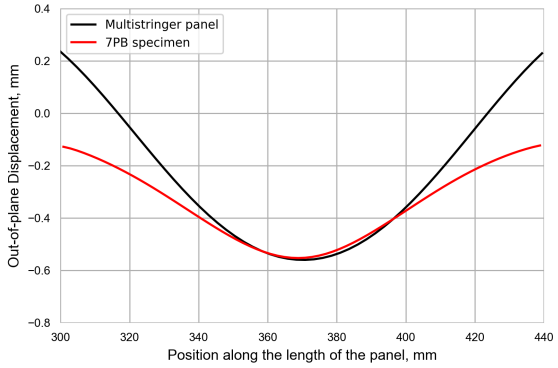

(c) At an applied in-plane displacement of 2.2 mm.

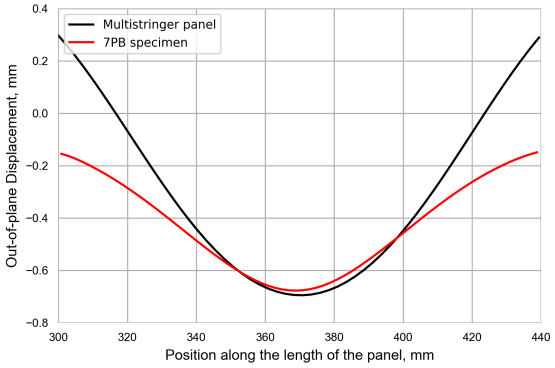

(d) At an applied in-plane displacement of 2.5 mm.

Figure 6.18: Comparison of the out-of-plane displacements of the skin at the stringer flange edge between the 7PB specimen and the critical region in the multistringer panel throughout the considered range of applied in-plane displacements.

This verifies that the 7PB specimen is capable of representing the mode shape of the multi-stringer panel in the considered range of applied in-plane displacements. Therefore, the final size of the 7PB specimen is 140 mm x 255 mm, with the indenter configuration shown in Table 6.3, denoted by "new 7PB specimen". Finally, it can also be concluded that a smaller area of interest than initially assumed needs to be considered to obtain the optimal loading configuration. Here, the area of interest of 100 mm x 30 mm used for the new 7PB specimen was obtained through trial and error.

6.2.3 Four Point Twisting Specimen

The out-of-plane displacements in the region near the inflection point are approximated by a single stringer specimen in a 4PT configuration. Specifically, this means that the specimen is loaded by two loading indenters at the top side of the specimen (the stringer side), while being supported by two indenters at the bottom side of the specimen (the skin side). First, the size of the 4PT specimen is determined based on the buckling mode shape of the multistringer

panel near the critical location. Then, the optimal position of the loading and supporting indenters are determined, such that the out-of-plane displacements in the critical region of the multistringer panel are accurately reproduced on the 4PT specimen.

Sizing of the Four Point Twisting Specimen

The buckling mode shape of the multistringer panel at an applied in-plane displacement of 2.5 mm is considered for the sizing of the critical region and the 4PT specimen. At this displacement, the buckling mode shape has fully developed in all of the bays and the location of the inflection point has stabilized to a value of $x = 419$ mm. Due to the bending mismatch between the skin and stringer, damage at the inflection point will probably not be critical and will therefore initiate later than damage at the location of maximum bending. In Figure 6.19, the out-of-plane displacements of the skin of the multistringer panel at $x = 371$ mm along the panel width can be seen in Subfigure 6.19(a). The out-of-plane displacements along the stringer flange edge near the inflection point can be seen in Subfigure 6.19(b). The size of the 4PT specimen and of the critical region in the multistringer panel are based on these.

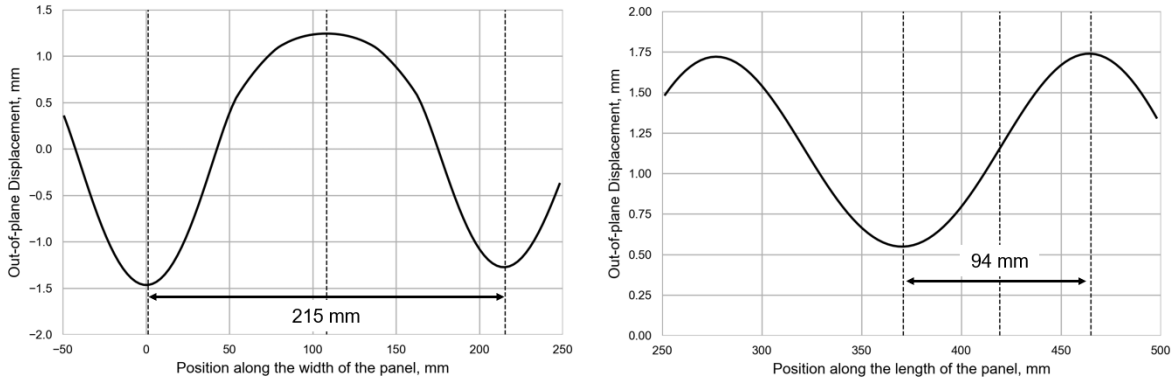

(a) Along the y-direction at the location of maximum bending.

(b) Along the stringer flange edge.

Figure 6.19: Out-of-plane displacements of the skin of the multistringer panel at an applied in-plane displacement of 2.5 mm, used for the sizing of the critical region and the 4PT specimen.

Considering the width (along the y-direction), the loading indenters can be placed as far as the minima on each side of the stringer. Considering Subfigure 6.19(a), the width is determined to be 255 mm, similarly as in the 7PB specimen. The length is taken to be equal to a buckling halfwave, extending from the extrema adjacent to the inflection point in the multistringer panel. Considering Subfigure 6.19(b), it can be seen that this distance is approximately equal to 94 mm. No additional 40 mm is added in length. This is because the indenters will not be placed at points corresponding to the extrema. The reasoning behind this is made clear by looking at Figure 6.20. In Subfigure 6.20(a), the current length of the 4PT specimen is highlighted. As mentioned before, the indenters should be placed at least 20 mm away from the edges. Doing so, it can be seen that the slope of the skin in between the indenters matches well with the slope of the skin in the multistringer panel. In Subfigure 6.20(b), the specimen length is increased by 40 mm, to place the indenters at the extrema. Clearly, the slope of the

skin in between the indenters does not match well with the multistringer panel. Therefore, it is decided to not place the indenters at the extrema and consequently, to not increase the length of the specimen by 40 mm.

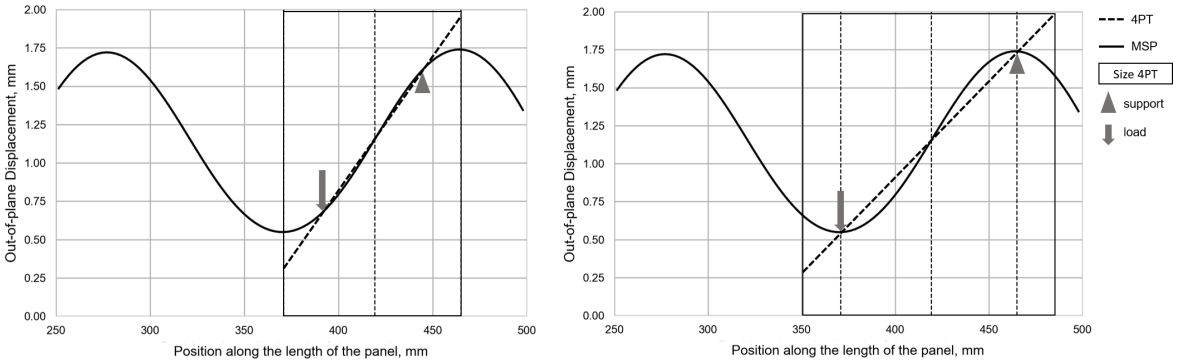

(a) 4PT specimen of length 94 mm.

(b) 4PT specimen of length 134 mm with the indenters at the extrema.

Figure 6.20: Illustration showing why the indenters of the 4PT specimen should not be placed at points corresponding to the extrema of the out-of-plane displacements of the skin in the multistringer panel.

So, the final dimensions of the 4PT specimen are 94 mm x 255 mm. The critical region of the multistringer panel corresponding to this specimen is shown in Figure 6.21.

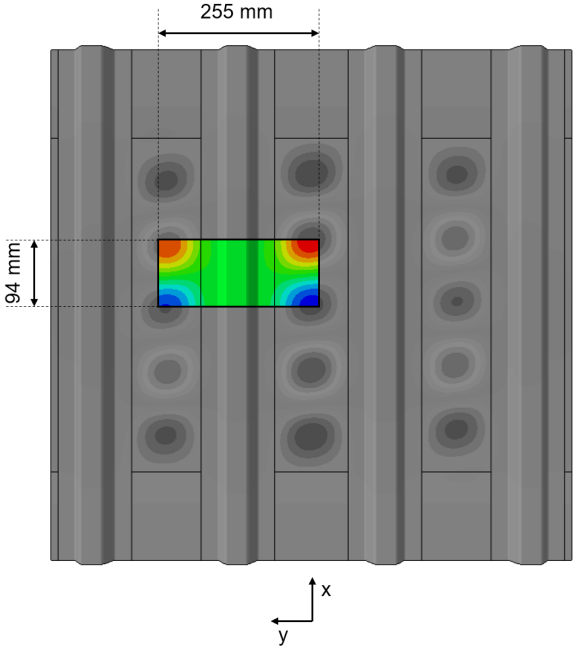

Figure 6.21: The critical region of the multistringer panel that will be captured by the 4PT specimen.

Indenter Positions of the Four Point Twisting Specimen

After the 4PT model is set up, the Python tool iterates through different indenter positions to try and minimize the shape error between the 4PT specimen and the critical region on the multistringer panel. Two different variables are defined when considering the location of the indenters on the 4PT specimen. The positions of all indenters are defined by the variables S_x and S_y, as can be seen in Figure 6.22.

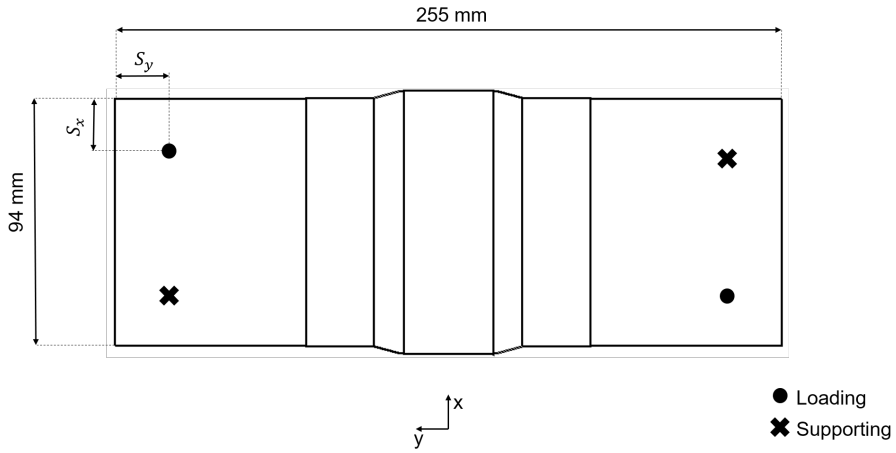

Figure 6.22: 4PT configuration and definitions of the position variables.

As with the 7PB specimen, some constraints are applied to the variables:

- The loading and support points are equidistant from the edges, hence only two free variables, S_x and S_y.
- The indenters should be located at least 20 mm from all edges. This means $S_x, S_y \geq 20$ mm.
- The indenters cannot be placed within 15 mm from the stringer flange edge.

Once the indenters are positioned, a displacement is applied equal to the difference in out-of-plane displacement between the points in the multistringer panel corresponding to the loading and supporting indenter. This is because in the 4PT model, the supporting indenters remain stationary, while the loading indenters are displaced. Similar as to the 7PB specimen, an area of interest is defined to calculate the shape error. From the results of the 7PB analyses, it becomes clear that the free edges should not be included in the area of interest. The free edge effect becomes apparent in the regions of the single stringer specimen beyond the indenters. For the 7PB specimen, the locations of the corner indenters were more or less set at the inflection points, so the area of interest extended from the inflection point to the inflection point. However, in this case, the positions of the indenters along the specimen length are not known beforehand. Therefore, the entire length of the specimen is included in the area of interest. Next to that, for the 7PB specimen, it was also shown that to accurately represent the out-of-plane displacements of the skin along the stringer flange edge (these directly drive damage initiation and propagation and therefore need to be well simulated on

the 4PT specimen), a smaller width of the area of interest, only focused on the skin along that edge, should be used in the determination of the loading configuration. Furthermore, the width should be as narrow as possible such that the out-of-plane displacements of the skin at the stringer flange edge are captured well, but it should also be wide enough to avoid inaccuracies in terms of the shape of the skin near the, in this case, inflection point. Therefore, an area of interest of 94 mm x 10 mm is obtained through trial and error and is used to determine the positions of the loading and supporting indenters in the 4PT specimen, see Figure 6.23.

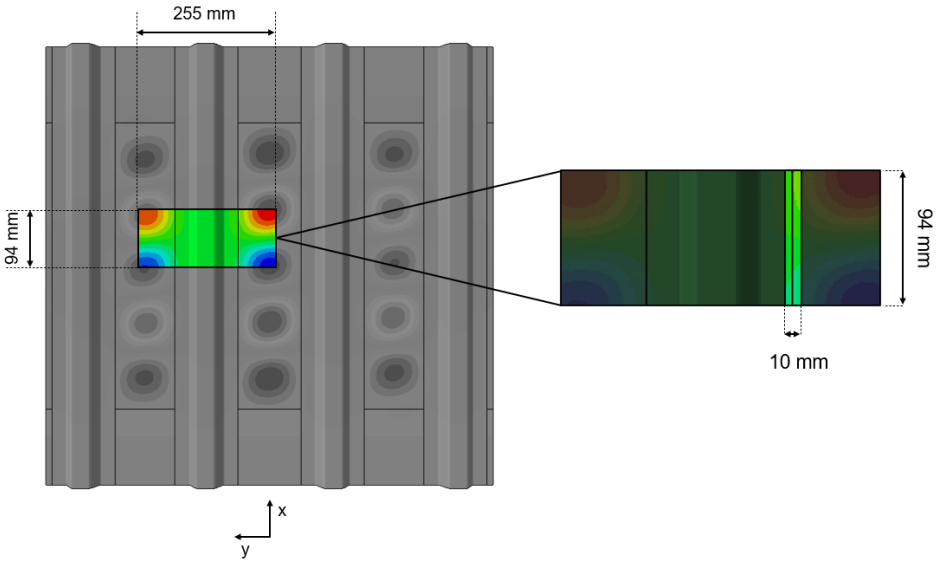

Figure 6.23: The area of interest for the shape comparison with the 4PT specimen.

Iterating through the indenter positions, the configuration with $S_x = 20$ mm and $S_y = 57$ mm leads to the lowest RSS. The contour plot of the optimal 4PT specimen as compared to the multistringer panel can be seen in Subfigure 6.24(d). To verify that this configuration is able to represent the shape of the multistringer panel at different applied displacement values in the considered range (1.5 mm - 2.6 mm), a comparison between the contour plots is also made at a displacement of 1.5 mm, 2.0 mm and 2.2 mm. This can be seen in Figure 6.24. From this, it becomes clear that the overall deformation shape of the 4PT specimen does not match very well with the critical region in the multistringer panel.

However, considering the out-of-plane displacements of the skin along the stringer flange at the same applied in-plane displacements, shown in Figure 6.25, it can be seen that the 4PT specimen and the multistringer panel match quite well throughout the considered range. Initially, right after buckling, the curves do not match well. However, it is unlikely that skin-stringer separation will happen right after buckling. The offset between the curves in the other plots can be explained by the fact that it is impossible for the curves to overlap exactly due to the transverse loading of the 4PT specimen and the in-plane loading of the multistringer panel. However, despite the small offset in out-of-plane displacements, the curves demonstrate that the slope of the skin around the inflection point is accurately represented.

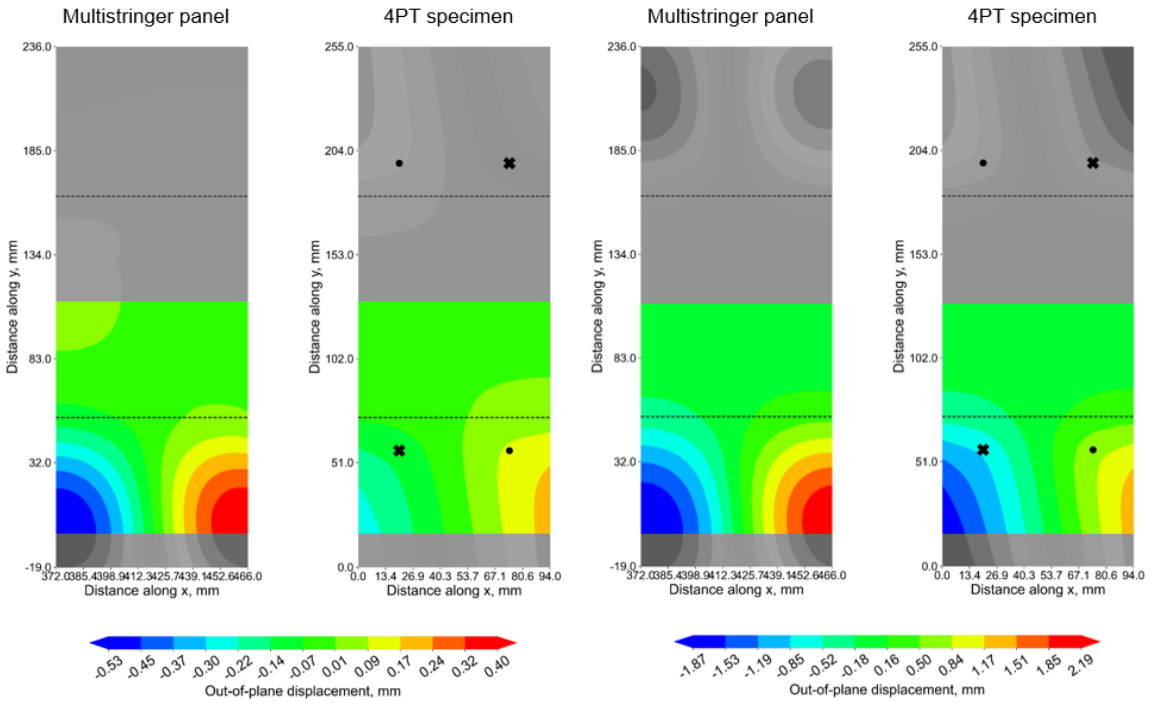

(a) At an applied displacement of 1.5 mm.

(b) At an applied displacement of 2.0 mm.

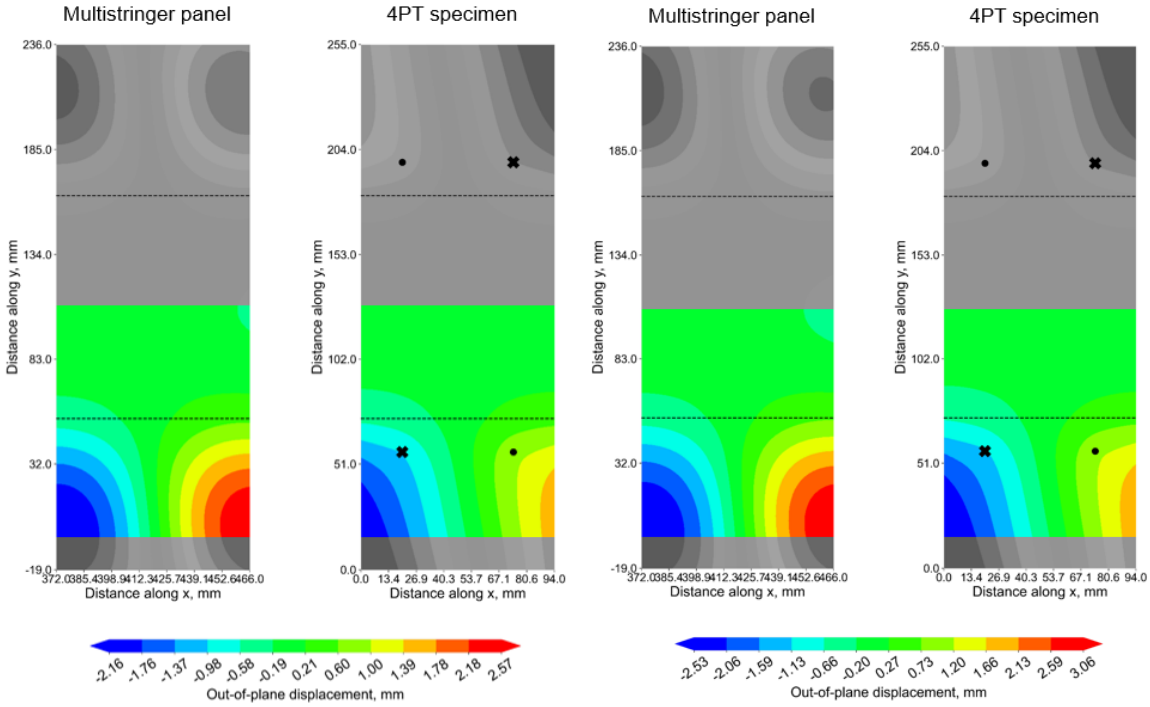

(c) At an applied displacement of 2.2 mm.

(d) At an applied displacement of 2.5 mm.

Figure 6.24: Contour plot comparison between the 4PT specimen and the critical region in the multistringer panel throughout the considered range of applied in-plane displacements.

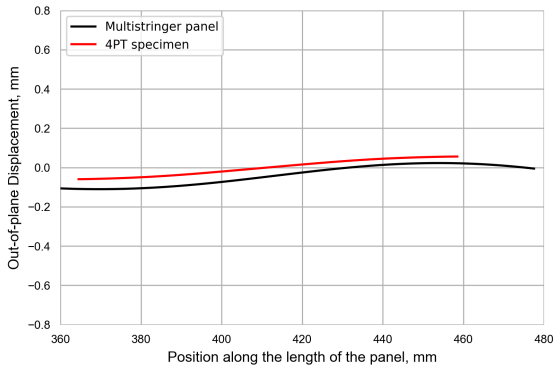

(a) At an applied in-plane displacement of 1.5 mm.

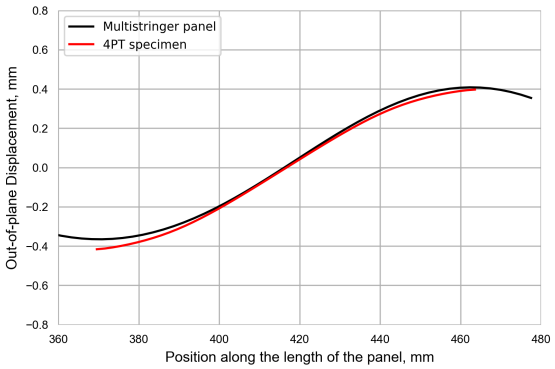

(b) At an applied in-plane displacement of 2.0 mm.

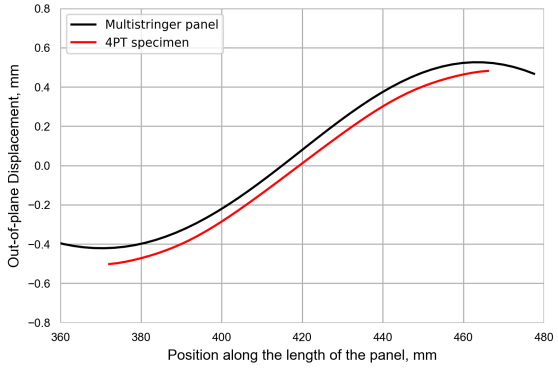

(c) At an applied in-plane displacement of 2.2 mm.

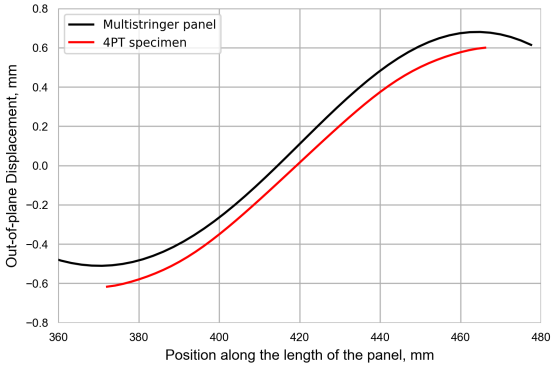

(d) At an applied in-plane displacement of 2.5 mm.

Figure 6.25: Comparison of the out-of-plane displacements of the skin at the stringer flange edge between the 4PT specimen and the critical region in the multistringer panel throughout the considered range of applied in-plane displacements.

Therefore, this verifies that the 4PT specimen is capable of representing the mode shape of the multistringer panel in the considered range of applied in-plane displacements.

Chapter 7

Skin-Stringer Separation

In chapter 6, a 7PB and 4PT specimen were designed. An optimal loading configuration was determined based on the minimum shape error between the single stringer specimens and the corresponding critical region in the multistringer panel. To verify that these single stringer specimens exhibit the same damage behaviour as the multistringer panel in compression, detailed analyses are performed on the 7PB and 4PT specimens. In these analyses, damage models are included to obtain the initiation and propagation of skin-stringer separation in the single stringer specimens. Next, the damage in the multistringer panel is obtained through a model of the multistringer panel with cohesive elements along the central bay and the single stringer specimens are verified with the results obtained from the multistringer panel.

7.1 Skin-Stringer Separation in the Seven Point Bending Specimen

The 7PB specimen, designed in chapter 6, is modelled in detail to verify that it can accurately represent the behaviour of the multistringer panel in the critical region near the location of maximum bending and to obtain a prediction of the damage propagation within the 7PB specimen.

7.1.1 Geometry

The 7PB specimen consists of a skin and single stringer. The stringer dimensions are as described in section 3.1. The dimensions of the skin are determined in chapter 6. The skin has a length of 140 mm and a width of 255 mm. The stringer spans the entire length of the skin. The specimen dimensions can be seen in Figure 7.1.

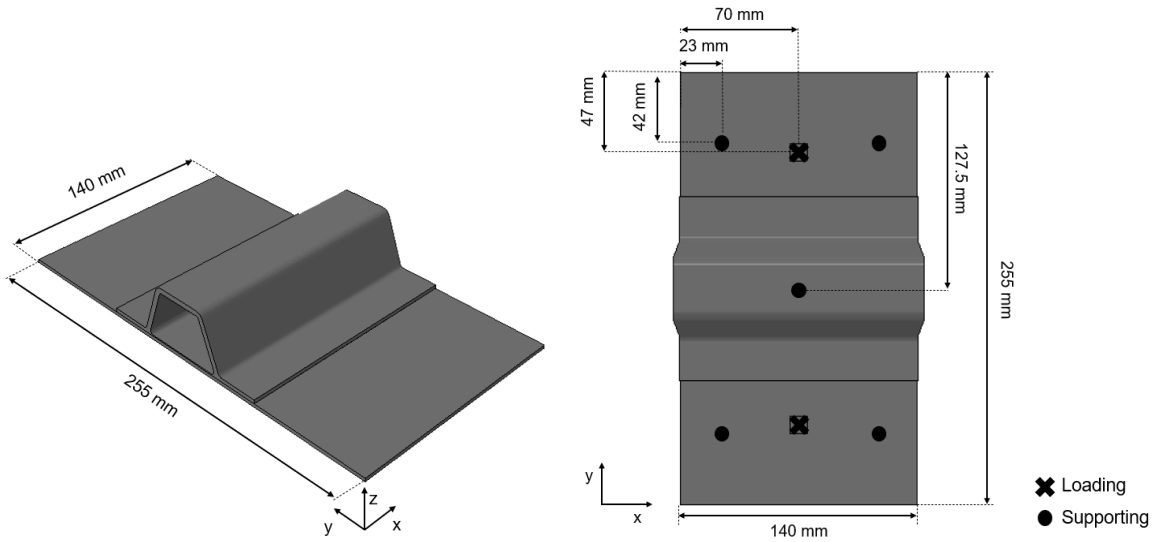

(a) Dimensions. (b) Indenter positions.

Figure 7.1: Geometry of the 7PB specimen used for detailed damage analyses.

As mentioned in section 3.1, the skin is made out of a tape material, while the stringer is made out of a fabric material. The lamina properties can be found in Table 3.1. The noodle regions are filled with an epoxy material.

Seven indenters are used to enforce the deformation onto the specimen. In section 6.2.2, the position of the loading and supporting indenters are determined. The two loading indenters are placed central along the length of the specimen; 70 mm from the transverse edges (along x) and 47 mm from the longitudinal edges (along y). The central bottom indenter is placed exactly in the center of the skin; 70 mm from the transverse edges and 127.5 mm from the longitudinal edges. Finally, the remaining four bottom indenters are placed symmetrically in each corner, namely 23 mm from the transverse edges and 42 mm from the longitudinal edges. The indenter positions can be seen in Subfigure 7.1(b).

Metallic shims are placed onto the skin at the locations where the top indenters apply the load. The shims are assumed square with the following dimensions; 10 mm x 10 mm x 0.25 mm. These are included to ensure that no damage is created due to the load introduction and to distribute the stress concentration underneath the top indenters.

7.1.2 Finite Element Model

A finite element model is created in Abaqus to simulate the behavior of the specimen.

Mesh

Similarly as for the baseline model in chapter 4, the mesh of the stringer is refined in two directions. The mesh becomes more refined towards the center of the stringer to ensure a fine mesh and that the elements there have an aspect ratio of approximately equal to one, since it is expected that damage initiates there, at the location of maximum bending.

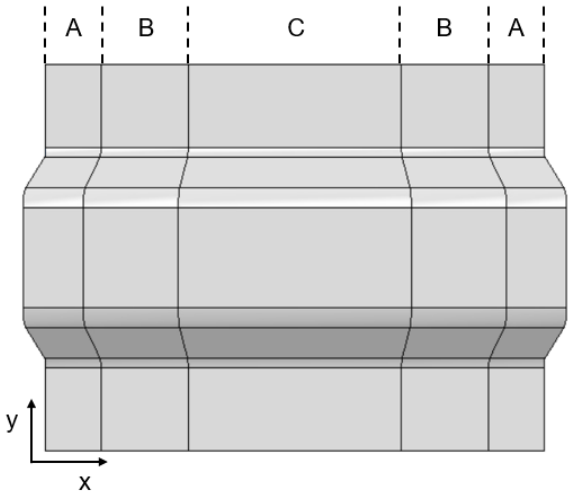

Figure 7.2: Regions of the stringer of the 7PB specimen with different mesh sizes.

The outer portions of the stringer are more coarsely meshed, since these are less important for damage initiation. The mesh is refined gradually from the coarser mesh at the stringer ends to the finer mesh at the central part. Looking at Figure 7.2, this means that in the parts indicated with the letter *A*, the mesh is relatively coarse. The mesh is more refined in *B* and finally, the elements in the part indicated with *C* have an aspect ratio approximately equal to one. The stringer flanges are refined in the transverse direction (along y) as well. This is to ensure a sufficient amount of elements in the cohesive zone.

An overview of the mesh size in each part can be seen in Table 7.1. The mesh sizes are determined based on the sensitivity analysis in chapter 4.

Table 7.1: Mesh sizes along the stringer length in the detailed model of the 7PB specimen.

Region	Length [mm]	Element size along y [mm]	Element size along x [mm]	Aspect ratio [-]
Region A	15.5	0.25	1.0	4
Region B	24.5	0.25	0.5	2
Region C	60	0.25	0.25	1

The noodle regions of the stringer are finely meshed, to accurately capture the behaviour of the noodle throughout the analysis. An element size of approximately 0.15 mm is used there. Furthermore, the mesh in the lower radii of the stringer is such that it matches with the noodle regions. The mesh of the noodle can be seen in Figure 7.3.

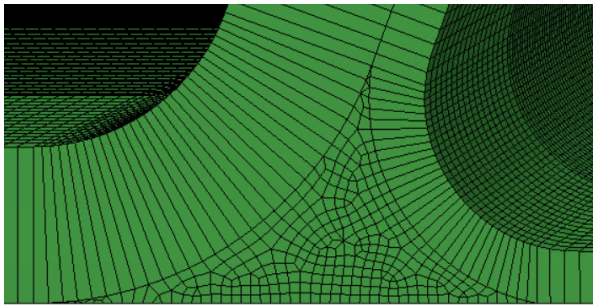

Figure 7.3: Mesh in the noodle regions of the 7PB specimen.

The mesh of the skin matches the mesh of the stringer in the regions where they overlap. The remainder of the skin is more coarsely meshed along the y-direction, such that at the skin edges, a mesh size of 1 mm is used, which gradually decreases to 0.25 mm underneath the stringer flanges. Furthermore, the parts of the skin directly underneath the top indenters are finely meshed and match the mesh of the shims there. As mentioned before, the shims are 10 mm x 10 mm, but on the skin, an area of 15 mm x 15 mm is used to gradually refine the mesh of the skin to match the mesh of the shims. Finally, one element is used through the thickness of the skin and the stringer.

Between the skin and stringer, underneath the flanges, a cohesive strip is inserted. This strip has a width equal to the width of the flanges and a length equal to 109 mm (covering regions B and C in Figure 7.2). This length is such that the free edge effect is excluded. Beyond the corner indenters, the behaviour of the specimen is unconstrained. Placing cohesive elements there may lead to damage initiation near the edges due to boundary effects, which would result in discrepancies with the multistringer panel predictions. The corner indenters are placed 23 mm away from the edges, along the x-direction. In Figure 7.4, the indenter is indicated by a black dot. However, the cohesive elements extend until 15.5 mm from the edges. This is to avoid a change in mesh size at the exact location where the indenters come into contact with the skin. Doing so may result in convergence issues. Therefore, the ends of the cohesive strips exceed the corner indenters by 7.5 mm, which comes from the skin surface of 15 mm x 15 mm used in the contact interaction with the indenters. The length of the cohesive strip is such that the entire contact surface is included. This can all be seen in Figure 7.4. It should be noted that this figure is for illustrative purposes only and is not to scale. The cohesive strips have a very small thickness of 10^{-5} mm as an approximation of zero-thickness cohesive elements. The mesh of the cohesive strips matches the mesh of the skin and stringer.

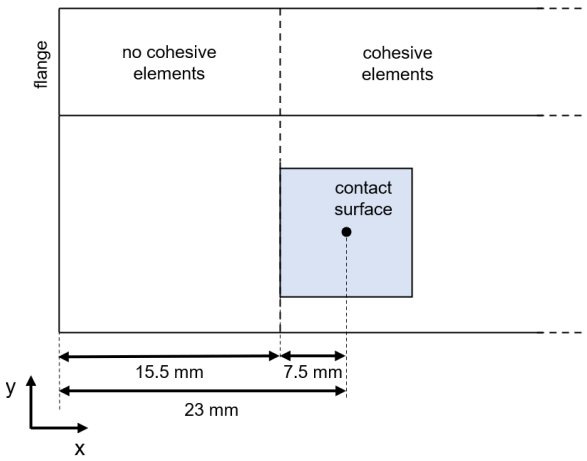

Figure 7.4: Illustration showing the reasoning behind the cohesive strip length in the 7PB specimen.

The skin, interior wrap and overwrap are meshed using SC8R elements. The noodle regions are hex-dominated with C3D8 elements, but contain C3D6 elements in its corners to complete the mesh. The shims are meshed using C3D8R elements and the cohesive strips consist of COH3D8 elements.

The final mesh of the 7PB specimen can be seen in Figure 7.5. The finite element model

consists of approximately 1150000 nodes and 770000 elements.

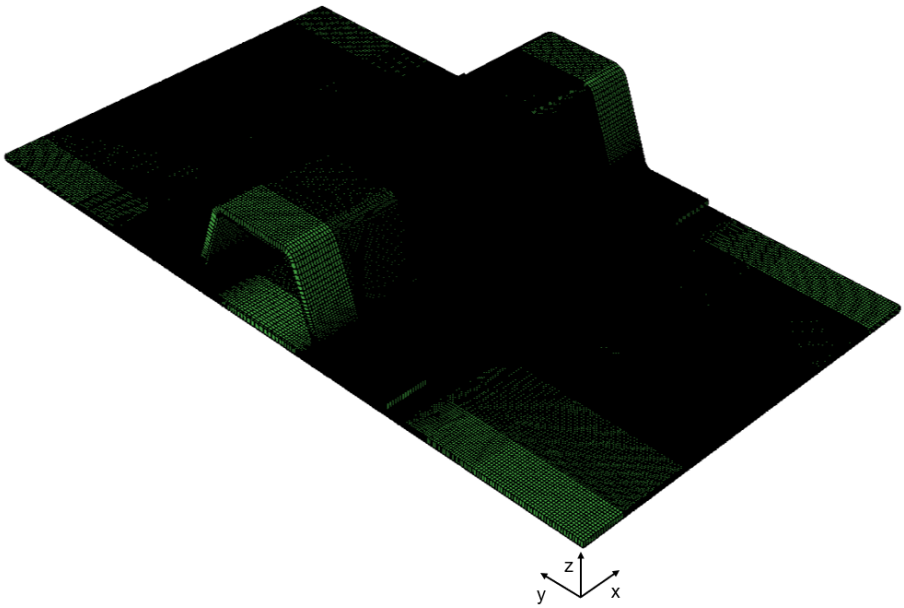

Figure 7.5: Mesh of the 7PB specimen used for detailed analyses.

Material Definition

For the composite parts, the layups specified in section 3.1 are assigned to the SC8R elements of each part. The ply properties can be found in Table 3.1.

A trilinear cohesive law, through the superposition of two bilinear cohesive laws, based on the cohesive base and the tape/fabric bridging properties is used for the cohesive elements. The properties can be found in previous chapters, but are summarized below for the ease of the reader, see Table 7.2.

Table 7.2: Cohesive properties used in the 7PB specimen model [31].

	K_I [N/m^3]	K_{II} [N/m^3]	G_{Ic} [kJ/m^2]	G_{IIc} [kJ/m^2]	σ_c [MPa]	τ_{IIc} [MPa]	η_{BK} [-]
Cohesive base	$4.89e^{13}$	$3.53e^{13}$	0.240	0.739	62.29	92.95	2.07
Tape/fabric bridging	$5.43e^{12}$	$8.14e^{12}$	0.350	2.102	6.89	20.67	3

Numerically, the superposition is achieved by duplicating the layer of cohesive elements such that the new layer shares nodes with the original layer. The first law is then assigned to the original layer and the second law to the duplicated layer. For both, the quadratic stress criterion is used to predict damage initiation, while the B-K criterion is used to predict damage propagation. A trilinear cohesive law is chosen over a bilinear cohesive law to ensure that the R-curve effect is taken into account in the analysis. The tape/fabric bridging properties are used over the structural bridging properties for the second bilinear law. From literature, it

becomes clear that both these bridging laws are successful in capturing the R-curve effect that is observed in tests, but both still show discrepancies with experimental results [31]. Therefore, it is not straightforward to determine which one is "better". In this thesis, the tape/fabric bridging properties are used in the detailed models of the single stringer specimens and in the verification model, to remain consistent. If the models developed in this thesis are validated with tests in future research, they should also be run with the structural bridging properties, to see which properties are required to predict the experimental response of the specimens the best.

The noodle regions and shims are assigned elastic isotropic materials, of which the material properties have been reported in Table 4.4.

Contact, Constraints and Boundary Conditions

All parts are assembled in a 7PB configuration. The indenters are built as rigid surfaces and are positioned as described in subsection 7.1.1. A surface-to-surface contact interaction is defined between the indenters and the skin or the shims. A friction coefficient of 0.333 is used in the interaction to account for interrelated shear and normal forces, associated with contact. Small sliding is defined for the contact pairs to limit the computational effort required to complete the analysis. The indenters are specified as the master surfaces, while the skin or shims are specified as the slave surfaces. For each contact pair, a skin surface of 15 mm x 15 mm is defined. The cohesive strips are tied to the stringer flanges and the skin. The parts of the skin and stringer that are free of cohesive elements are directly tied together. The shims are tied to the skin as well. Finally, the supporting indenters are fixed in place; they are constrained in all directions. The loading indenters are also fixed, but are left free to displace along the z-direction.

Analyses

A non-linear dynamic implicit step is defined. During this step, a downward displacement of 15 mm is applied to the top indenters at a rate of 25 mm/s. Quasi-static conditions are enforced, to ensure that the dynamic implicit solver approaches the problem as a quasi-static problem.

7.1.3 Discussion of the Results

The results of the 7PB specimen are discussed in terms of the load-displacement curve, damage damage initiation, damage location and damage propagation. It should be noted that in this thesis, damage initiation is defined as the point at which the damage variable of the cohesive elements becomes equal to one for the first time.

The load-displacement curve of the 7PB specimen can be seen in Figure 7.6. The point of damage initiation is also indicated in the plot. It becomes clear that the 7PB specimen maintains load-carrying capabilities after damage first initiates. The 7PB specimen only shows some unstable behaviour (load drops) when the damage has already propagated significantly.

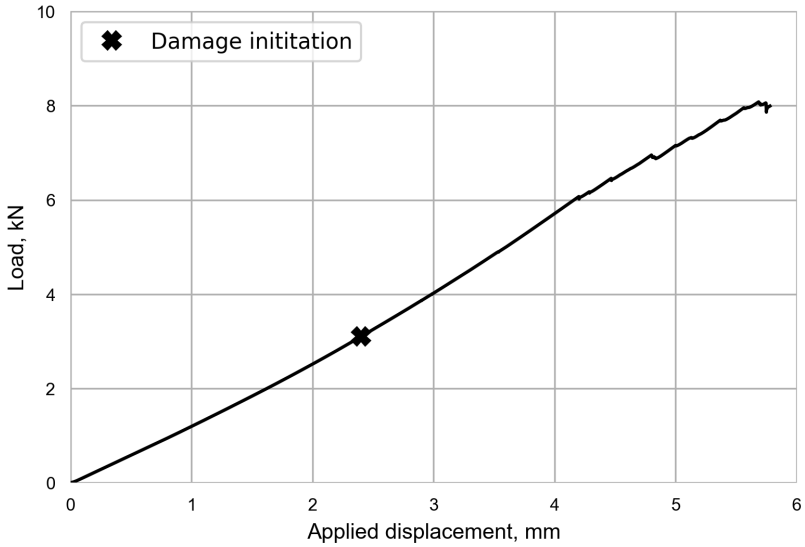

Figure 7.6: The load-displacement curve of the 7PB specimen.

The applied out-of-plane displacement at which damage initiates in the 7PB specimen is equal to 2.35 mm. The damage initiation occurs in the center of the specimen, at the location of the minimum out-of-plane displacement, which is consistent with what is expected in the 7PB specimen. In Figure 7.7, the deformed 7PB specimen is shown at the applied displacement just after damage initiation (2.4 mm). Isolating one of the cohesive strips, it can be confirmed that damage has initiated in its center, which corresponds to the location of maximum skin bending.

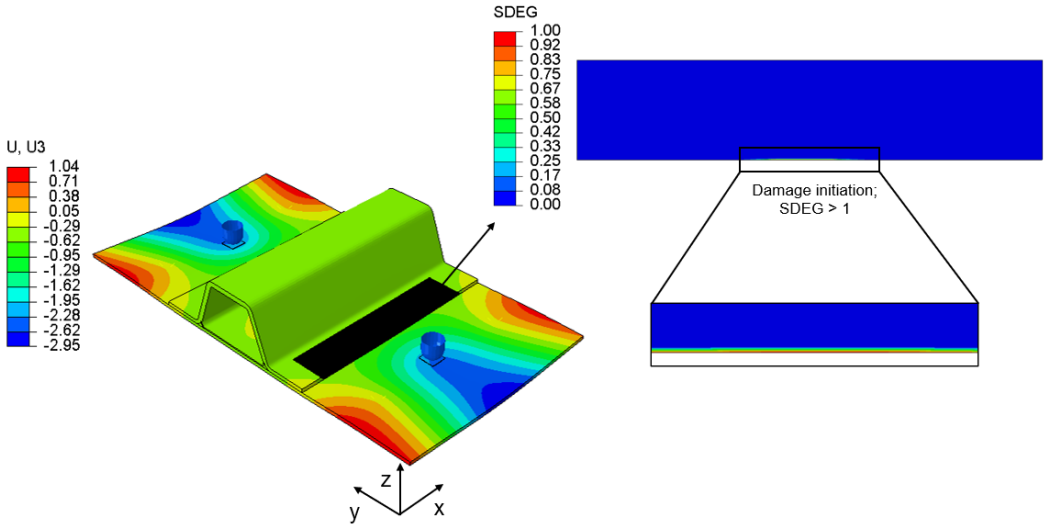

Figure 7.7: Location of damage initiation in the 7PB specimen.

In Figure 7.8 the damage propagation of the 7PB specimen can be seen. The damage just before reaching the noodle region is only considered here. Since there are no cohesive elements

underneath the noodle region and the interior wrap, the damage front will not be realistic anymore after the damage has reached the noodle region.

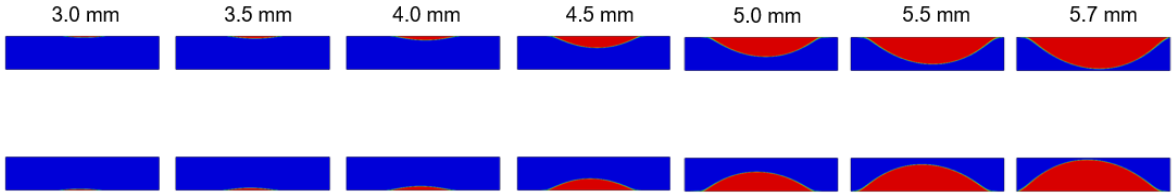

Figure 7.8: Damage propagation in the 7PB specimen.

With this in mind, it can be seen that after damage initiation, the damage propagates in an elliptical shape towards the noodle region. Initially, the damage propagates at a relatively slow rate. Then, from an applied displacement of 4.0 mm onwards, the damage propagates at a higher rate than initially observed and the damage front moves towards the noodle region in a more unstable manner. The jumps in the damage front at higher applied displacements can clearly be linked to the load drops that can be seen in the load-displacement curve, shown in Figure 7.6, at displacements higher than 4.0 mm. The damage reaches the noodle region at an applied displacement between 5.7 and 5.8 mm.

In Figure 7.9, the mode mixity of the cohesive elements can be seen. As mentioned in chapter 2, in a cohesive law, one can distinguish between a damage initiation criterion (when the cohesive elements start to degrade) and a damage evolution criterion (when the critical fracture toughness is exceeded). In this case, for damage initiation, the quadratic stress criterion was used, while the B-K criterion was used for the damage evolution. Both are applied to mixed mode problems.

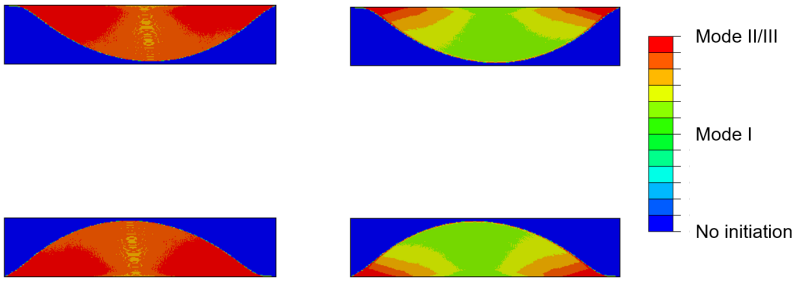

(a) Damage initiation. (b) Damage evolution.

Figure 7.9: Mode mixity of the cohesive elements in the 7PB specimen.

In Subfigure 7.9(a), the mode mixity of the cohesive elements when the damage initiation criterion is met, can be seen, while in Subfigure 7.9(b), the mode mixity of the cohesive elements when the damage evolution criterion is met, can be seen. The mode mixity ratio is defined as $1 - \frac{G_I}{G_T}$, in which $G_T = G_I + G_{II} + G_{III}$. So, when the damage initiates or propagates purely in mode I, the mode mixity ratio is equal to zero. On the other hand, when the damage initiates or propagates in a shearing mode (mode II/III), the mode mixity ratio is equal to 1. When damage has not initiated yet, the mode mixity ratio is equal to -1 [59]. It should be noted that no distinction can be made between mode II and mode

III here. In Figure 7.9, it can be seen that damage initiates mostly in the shearing modes. However, considering the damage evolution, it can be seen that the skin-stringer separation at the location of maximum bending is mostly in pure mode I, while the damage propagation towards the edges is caused by shearing. This confirms that the skin-stringer separation at the location of maximum bending is mode I dominated.

Finally, the behaviour of the noodle in the 7PB specimen is considered. No damage model has been incorporated in the noodle region. However, a look is taken at the stress and strain distribution in the noodle region throughout the analysis. The exact epoxy resin properties are unknown, so for this analysis, it is assumed that the noodle regions are filled with the resin used in the composite material of the skin and stringer, namely Hexply 8552 Epoxy. The relevant and known properties of this resin can be seen in Table 7.3 and are obtained from the corresponding product data sheet by Hexcel.

Table 7.3: Hexply 8552 Epoxy properties [65].

	Tensile strength [MPa]	Tensile modulus [GPa]	Tensile strain [%]
HexPly 8552 Epoxy	121	4.67	1.7

First, a look is taken at the stress and strain distributions in the noodle region at an applied displacement of 5.7 mm, when the damage has just not reached the noodle. The maximum tensile, compressive and shear stresses are derived, as well as the maximum tensile, compressive and shear strains. Then, the tensile strength and strain assumed for the noodle material (see Table 7.3) are used to determine whether tensile failure could occur in the noodle region. Considering the properties shown in Table 7.3, the behaviour of the epoxy cannot be assumed purely linear elastic. Therefore, both the tensile strength and tensile strain are considered to assess whether tensile failure could occur. The stress and strain distributions can be seen seen in Figure 7.10.

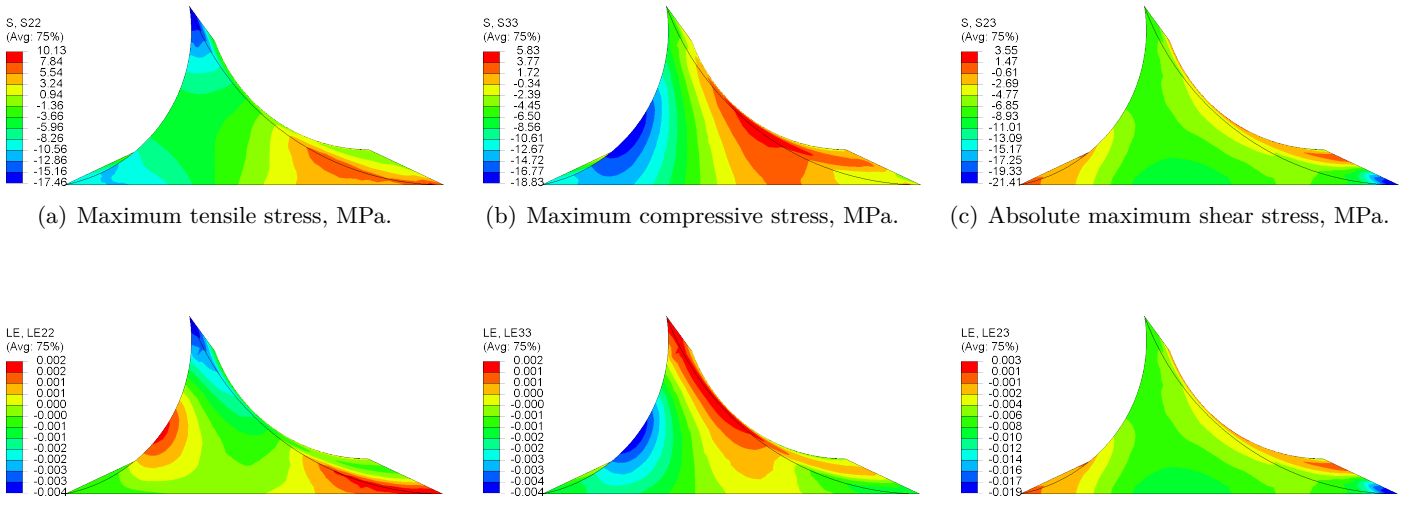

(a) Maximum tensile stress, MPa. (b) Maximum compressive stress, MPa. (c) Absolute maximum shear stress, MPa.

(d) Maximum tensile strain, -. (e) Maximum compressive strain, -. (f) Absolute maximum shear strain, -.

Figure 7.10: Stress and strain distributions in the noodle region of the 7PB specimen.

Here, the cross-sectional view of the noodle region is such that the z-axis is pointing upwards and the y-axis is pointing to the left. Only one of the noodle regions is considered, since the stress and strain distributions of the other noodle region will be more or less symmetric. The maximum of the stresses and the strains all occur approximately halfway along the specimen length, at $x \approx 70$ mm, which is consistent with the location of the maximum skin bending. In Subfigure 7.10(a) and Subfigure 7.10(d), it can be seen that the maximum tensile stress and strain are concentrated at the noodle corner towards the stringer flange edge and are in the y-direction. The maximum compressive stress and strain, shown in Subfigure 7.10(b) and Subfigure 7.10(e) respectively, are concentrated at the interface with the interior wrap, but are in the z-direction. Finally, considering the absolute maximum shear stress and strain in Subfigure 7.10(c) and Subfigure 7.10(f), it is observed that these are concentrated in the noodle corner towards the stringer flange edge. Typically, damage initiates at stress and strain concentrations, so if at any point during the analysis, the resin material allowables shown in Table 7.3 are exceeded, damage will probably occur at these locations. Based on the assumed noodle properties, it can be concluded that if damage occurs in the noodle region, it will probably occur at the location of maximum bending, so halfway along the length of the 7PB specimen. Furthermore, using the assumed tensile properties, shown in Table 7.3, a first assessment can be made to evaluate if tensile failure could occur in the 7PB specimen before the damage reaches the noodle region. Comparing the maximum tensile stress and tensile strain with the material allowables, it can be seen that no tensile failure occurs before the damage reaches the noodle region. Nothing can be said about possible compressive or shear failure of the noodle region, since only tensile properties could be obtained. Furthermore, the properties are assumptions, so even though the results of this analysis may indicate that failure occurs, this is not necessarily the case in reality. However, it can give a first indication of the noodle behaviour in the 7PB specimen. To get a more complete and accurate image of the damage behaviour of the noodle region, the exact noodle material properties should be obtained. Furthermore, a damage model should be included for the noodle regions in the Abaqus model. Finally, cohesive elements should also be placed at the skin-noodle interface (at least there), to see whether there is an influence of the noodle region on the damage propagation.

7.2 Skin-Stringer Separation in the Four Point Twisting Specimen

The 4PT specimen, designed in chapter 6, is modelled in detail to verify that the 4PT specimen can accurately represent the behaviour of the multistringer panel in the critical region near the location of maximum twisting.

7.2.1 Geometry

The skin of the 4PT specimen has a length of 94 mm and a width of 255 mm. The stringer spans the entire length of the skin. The specimen can be seen in Figure 7.11.

Four indenters are used to enforce the deformation onto the specimen. In subsection 6.2.3, the position of the loading and supporting indenters are determined. All indenters are placed equidistant from the skin edges; 20 mm along the x-direction from the transverse edges and 57 mm along the y-direction from the longitudinal edges. The exact indenter positions are

shown in Subfigure 7.11(b). Metallic shims are placed on the skin at the locations where the indenters come into contact with the skin. The shims used here are the same as the ones used for the 7PB specimen.

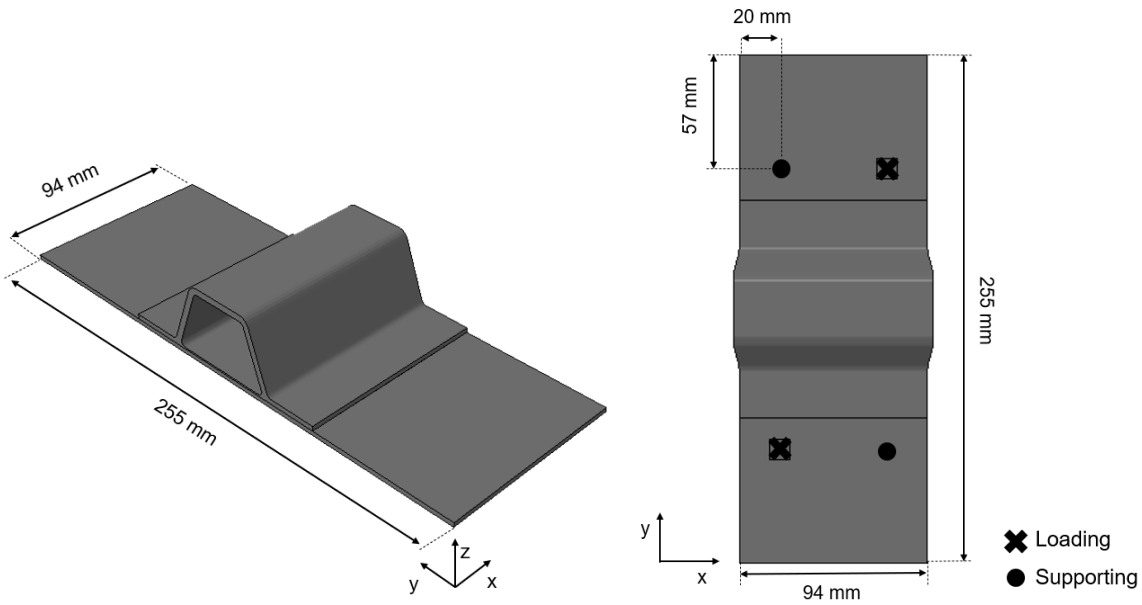

(a) Dimensions. (b) Indenter positions.

Figure 7.11: Geometry of the 4PT specimen used for detailed damage analyses.

7.2.2 Finite Element Model

A finite element model is created in Abaqus to simulate the behaviour of the 4PT specimen.

Mesh

Here, the mesh of the stringer is also refined in two directions. The mesh is more refined towards the central part of the stringer since damage initiation is expected to occur at the inflection point. Considering Figure 7.12, the parts indicated with the letter A are therefore more coarsely meshed than the part indicated with the letter B.

An overview of the mesh size in each part of the stringer can be seen in Table 7.4.

Table 7.4: Mesh sizes along the stringer length in the detailed model of the 4PT specimen.

Region	Length [mm]	Element size along y [mm]	Element size along x [mm]	Aspect ratio [-]
Region A	12.5	0.25	1.0	4
Region B	69	0.25	0.25	1

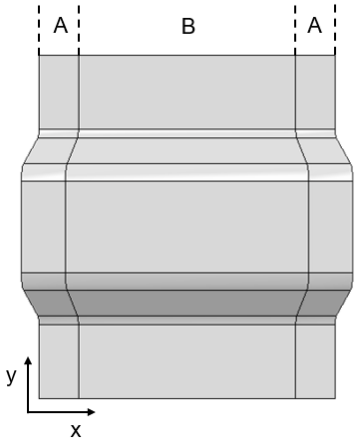

Figure 7.12: Regions of the stringer of the 4PT specimen with different mesh sizes.

The noodle regions and consequently the lower radii of the stringer are meshed as in the 7PB specimen, see Figure 7.3. The cohesive strips are placed underneath the stringer flanges and have a width equal to the flange width and a length of 69 mm, covering region B in Figure 7.12. This is to ensure the exclusion of the free edges. The exact length is determined as described for the 7PB specimen. The same element types are used for the different parts of the specimen as described for the 7PB specimen. The final mesh of the 4PT specimen can be seen in Figure 7.13. Here, it can also clearly be observed how the entire contact surface underneath the indenters is included in the region where cohesive elements are implemented. The finite element model consists of approximately 930000 nodes and 625000 elements.

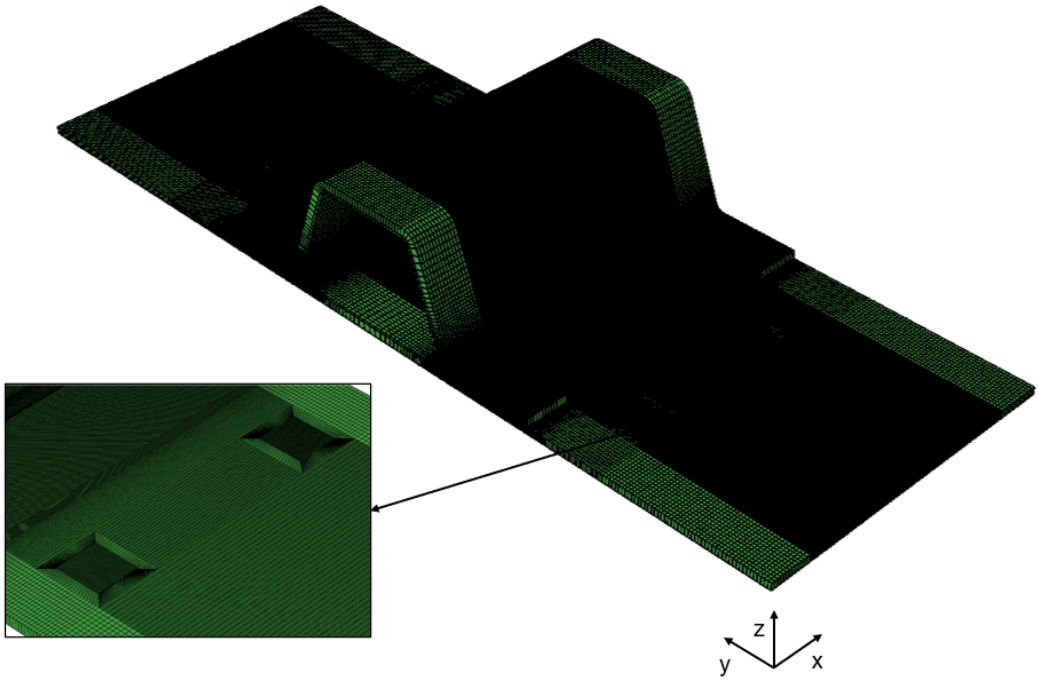

Figure 7.13: Mesh of the 4PT specimen used for detailed analyses.

Material Definition

For the 4PT specimen, the same material definitions are applied to the different parts as specified for the 7PB specimen.

Contact, Constraints and Boundary Conditions

All parts are assembled in a 4PT configuration, reported in subsection 7.2.1. A surface-to-surface contact interaction is defined between the indenters and the shims, similarly as in the 7PB specimen. The cohesive strips are tied to both the skin and stringer and in the regions where there are no cohesive elements, the skin and stringer are rigidly tied together. Finally, the supporting indenters remain fixed throughout the analysis, while the loading indenters are free to displace along the z-direction.

Analyses

A non-linear dynamic implicit step is defined, in which a downward displacement of 15 mm is applied to the loading indenters at a rate of 25 mm/s. Quasi-static conditions are enforced.

7.2.3 Discussion of the Results

The applied out-of-plane displacement at which damage initiates in the 4PT specimen is equal to 2.55 mm. In Figure 7.14, the deformed 4PT specimen can be seen, right after damage initiation (2.6 mm).

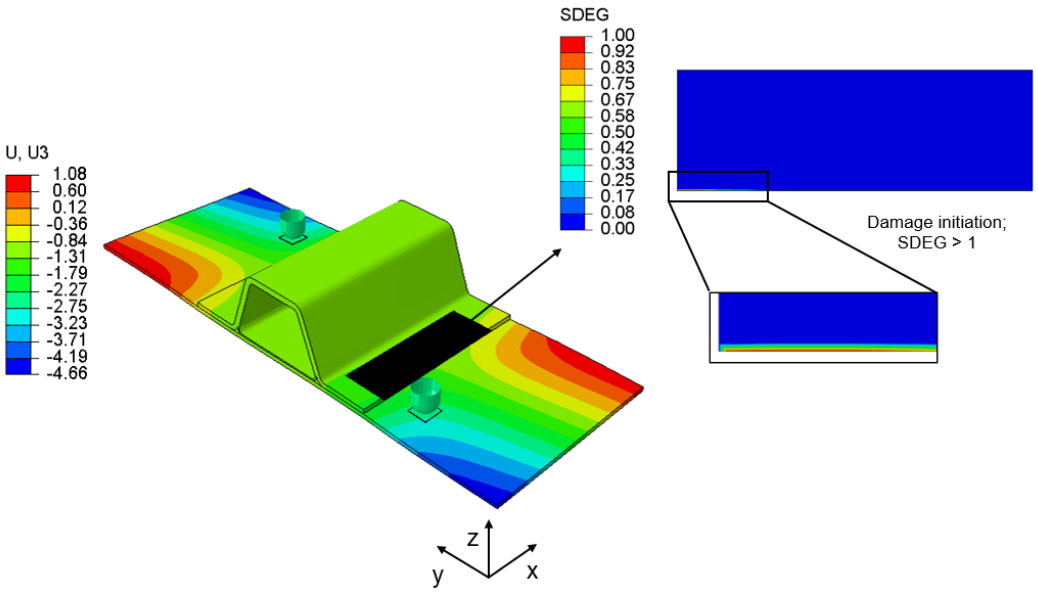

Figure 7.14: Location of damage initiation in the 4PT specimen.

In the isolated cohesive strip, it is shown that damage initiates in the corner near the loading indenter. This is inconsistent with what is expected in the 4PT specimen. In the 4PT

specimen, the inflection point of the buckling halfwave is halfway along the specimen length. Therefore, in this specimen, it is expected that damage initiates at its center, at the inflection point, due to twisting of the skin. However, this is not the case. The damage initiating at the edges shows that skin-stringer separation at the inflection point is non-critical. It initiates there because of the skin pulling away from the stringer, rather than because of skin twisting, which shows that the skin-stringer separation at the location of maximum bending is more critical. Since only the most critical skin-stringer separation is of importance in this thesis, the 4PT specimen will not be discussed further.

7.3 Skin-Stringer Separation in the Multistringer Panel

To verify that the damage occurring in the single stringer specimens subjected to transverse loading is representative of the damage in the multistringer panel in compression, a damage model for the multistringer panel is developed. Cohesive elements are included in the multistringer panel along the central bay. The panel is compressed up until an applied displacement of 2.6 mm, such that only the damage behaviour of the multistringer panel before the mode jump is obtained.

The multistringer panel, as described in section 3.1 is modelled. Similar as in the multistringer analysis in chapter 5, the pad-up region and potting are included. Next to that, each part of the panel is modelled with the elements specified in subsection 5.1.2 and the same material definitions are assigned to the elements. As opposed to the model developed in chapter 5, two cohesive strips are implemented underneath the stringer flanges next to the central bay. The reason that the cohesive elements are only included in this area is because the central bay is slightly larger than the outer bays, which means that damage will probably initiate there. By only placing cohesive elements along the central bay, the total number of elements in the model is limited and the computational expenses of running the model can be reduced compared to placing cohesive elements underneath all of the stringer flanges.

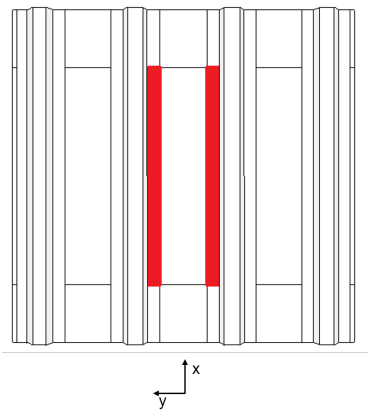

Figure 7.15: Cohesive strips along the central bay in the multistringer panel model.

The cohesive strips extend from pad-up region to pad-up region, as can be seen in Figure 7.15. As demonstrated in subsection 4.3.1, it is of utmost importance that the mesh of the cohesive strips is sufficiently fine to obtain accurate numerical predictions related to the damage initiation and propagation. There, it was shown that in the regions where the skin pulls away from the stringer, so where mode I skin-stringer separation is promoted, a mesh size of approximately 0.25 mm was sufficient for this panel. Furthermore, the elements in these kinds of regions perform best when they have an aspect ratio approximately equal to one. To limit the number of cohesive elements, the cohesive strips are partitioned and the mesh is such that in areas where the skin pulls away from the stringer, the elements are small and square, while in areas where the skin pushes towards the stringer, the mesh is coarser since it is not expected that skin-stringer separation occurs there.

In Figure 7.16, the out-of-plane displacements of the central bay just before the mode jump can be observed. This contour plot is used to partition the cohesive strips. The analysis will run up until an applied displacement of 2.6 mm. This way, the mesh of the cohesive strips does not need to be refined entirely to account for the change in buckling mode shape after the mode jump.

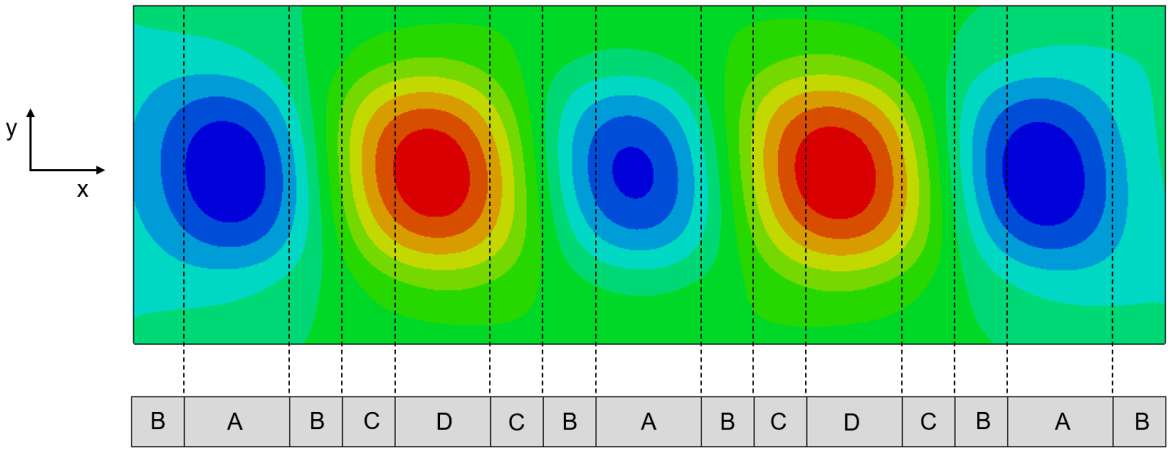

Figure 7.16: Partitions of the cohesive strips according to the out-of-plane displacements of the central bay in the multistringer panel before the mode jump.

Underneath the contour plot of the central bay in Figure 7.16, a partitioned cohesive strip can be seen. The mesh in each part of the cohesive strip is different according to the out-of-plane displacements in the central bay. An overview of the mesh size in each part can be seen in Table 7.5. It should be noted that these sizes are determined based on the mesh sensitivity analysis performed on the 7PB baseline model in chapter 4. The model is set up such that the mesh of the skin and stringers match the cohesive mesh in the regions where they overlap.

Table 7.5: Mesh sizes along the cohesive strip length for the multistringer panel model containing cohesive elements.

Region	Length [mm]	Element size along y [mm]	Element size along x [mm]	Aspect ratio [-]
Region A	50	0.25	0.25	1.0
Region B	25	0.25	0.50	2.0
Region C	25	0.25	1.0	4.0
Region D	45.1	0.25	1.96	7.84

In the central bay, the skin is meshed such that the element size gradually decreases from 1 mm in the center to 0.25 mm underneath the stringer flanges along the y-direction. This is to prevent a sudden change in element size at the stringer flange edge, as the displacements of the skin there are important for damage initiation. The finite element model contains approximately 3600000 nodes and 2200000 elements.

A trilinear cohesive law, through the superposition of two bilinear cohesive laws, based on

the cohesive base and the tape/fabric bridging properties is used for the cohesive elements, similar as for the 7PB and 4PT specimens. The properties can be found in Table 7.2.

The top and bottom edge of the panel, in the region where potting is located, are constrained for out-of-plane translation. The bottom edge is restricted along the x-direction and a single point on the bottom edge is additionally restricted along the y-direction, to avoid rigid body motion. The other edges are left free. Finally, a dynamic implicit analysis is used to apply an in-plane displacement of 2.6 mm at a rate of 2.6 mm/s to the top edge of the panel.

From the results, it becomes clear that damage initiates before the mode jump, which validates the previously made assumption that the buckling mode shape before the mode jump is critical. In Figure 7.17, the contour plot of the multistringer panel is shown in which the part of the cohesive strip that lies within the critical region near the location of maximum bending is isolated. On the righthand side of Figure 7.17, the contour plot of the isolated cohesive strip is shown at damage initiation. It is observed that damage initiation occurs at an applied displacement of 2.6 mm at the location of maximum skin bending (or the minimum out-of-plane displacement). It should be noted that even though this validates the assumption that damage initiates before the mode jump, very little damage has occurred at the end of the analysis; only one cohesive element in the direction transverse to the longitudinal edge of the cohesive strip has completely failed. It can also be observed that there is no damage near the critical inflection point. This proves that the skin-stringer separation at the inflection point, due to skin twisting, is not critical.

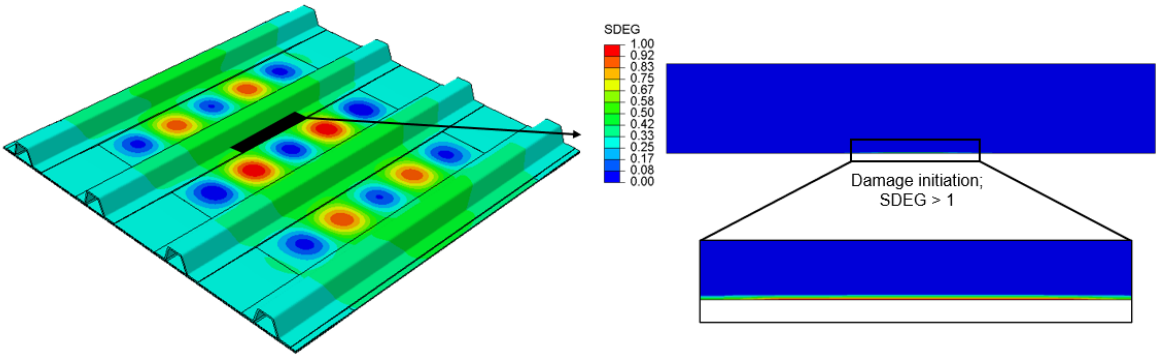

Figure 7.17: Damage initiation in the multistringer panel.

The load-displacement curve of the multistringer panel is shown below, in Figure 7.18, indicating the applied displacement at which damage initiation is observed.

The results of this analysis can be used to verify the 7PB specimen. The 4PT specimen cannot be verified, because no damage occurs at the inflection point in the multistringer panel before the mode jump. Furthermore, the 7PB specimen cannot be verified in terms of damage propagation, since the damage initiates right before the mode jump in the multistringer panel, and therefore, no damage propagation is observed.

Figure 7.18: The load-displacement curve of the multistringer panel with an indication of the applied displacement at which damage initiation is observed.

7.4 Verification of the Seven Point Bending Specimen

The 7PB specimen is verified with the results from the multistringer panel model developed in section 7.3.

The applied out-of-plane displacement value at which damage initiation occurs in the 7PB specimen was obtained in subsection 7.1.3 and can be seen in Table 7.6. Next to that, to confirm that the 7PB specimen obtained with a decreased area of interest is better representative of the multistringer panel in terms of damage initiation, the applied displacement at which damage initiates in the 7PB specimen, indicated with 7PB/v1/a in chapter 6, is also reported. The model for the 7PB/v1/a specimen was set up in the same way as the current model. The only difference is the indenter configuration. A comparison in indenter configuration between the 7PB/v1/a specimen and the current 7PB specimen can be seen in Table 6.3.

Table 7.6: Comparison of the out-of-plane displacement at which damage initiation occurs in the 7PB specimen model and the multistringer panel model.

	Displacement at initiation [mm]
7PB specimen model	2.35
Multistringer panel model	2.04
Relative difference	15.2%

Table 7.7: Comparison of the out-of-plane displacement at which damage initiation occurs in the 7PB/v1/a specimen and the multistringer panel model.

	Displacement at initiation [mm]
7PB/v1/a specimen model	3.7
Multistringer panel model	2.57
Relative difference	44.0%

Also reported in this table is the corresponding out-of-plane displacement value of the multistringer panel for damage initiation. This value is determined by taking the difference between the out-of-plane displacement of the points in the multistringer panel corresponding to the central supporting indenter and the loading indenter. The location of these points in the multistringer panel and their corresponding out-of-plane displacement values are obtained based on the loading configuration of the 7PB specimen, at an applied in-plane displacement of 2.6 mm (damage initiation in the multistringer panel). Figure 7.19 can be used to explain how the out-of-plane displacement value of the multistringer panel, shown in Table 7.6, is obtained. First, in Subfigure 7.19(a), the 7PB specimen can be seen on the right, with the supporting and loading indenters indicated. On the left of this subfigure, the corresponding critical region of the multistringer panel at an applied in-plane displacement of 2.6 mm can be seen. By hypothetically overlapping these two, the points in the critical region in the multistringer panel coinciding with the central supporting indenter and the loading indenter can be found. This is illustrated in Subfigure 7.19(a). The red dot and red cross are the points in the multistringer panel that correspond to the central support and the loading indenter in the 7PB specimen. In Subfigure 7.19(b), the out-of-plane displacements of the skin in the multistringer panel are plotted along the full black line shown in the contourplot of the critical region in Subfigure 7.19(a). In this plot, the points corresponding to the central support and loading indenter are also indicated. Using this plot, the individual out-of-plane displacement values for both of these points can be obtained. Doing so, the out-of-plane displacement of the point corresponding to the central indenter is equal to 1.28 mm. The out-of-plane displacement of the point corresponding to the loading indenter is equal to -0.76 mm. Taking the relative difference between these values results in an out-of-plane displacement of 2.04 mm. As shown in Table 7.6, this is equal to the corresponding out-of-plane displacement in the multistringer panel at damage initiation.

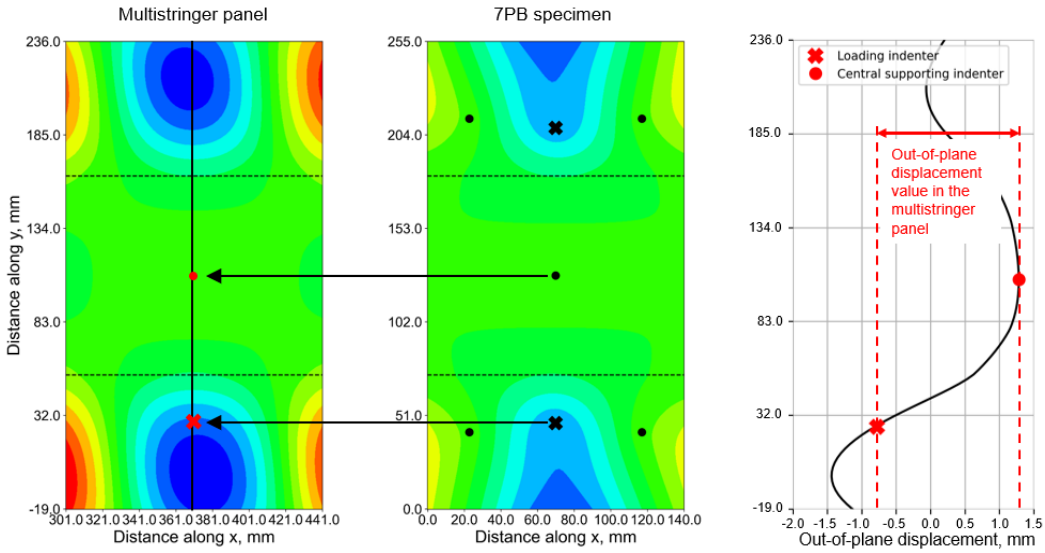

(a) Finding the points in the multistringer panel corresponding to the central supporting and loading indenter in the 7PB specimen.

(b) Deformation of the skin along the width of the panel.

Figure 7.19: Illustration showing how the out-of-plane displacement value in the multistringer panel is obtained.

Considering the values shown in Table 7.6 and in Table 7.7, it can be seen that the relative difference in out-of-plane displacement value for damage initiation between the current 7PB specimen and the multistringer panel is significantly smaller than the difference between the 7PB/v1/a specimen and the multistringer panel. This confirms that a correct representation of the out-of-plane displacements of the skin along the stringer flange edge is important to obtain a single stringer specimen that can predict skin-stringer separation in a multistringer panel and that a smaller area of interest is required in the shape error calculation to obtain the loading configuration of this single stringer specimen.

The difference of 15.2% that still exists between the multistringer panel and the 7PB specimen can be attributed to the fact that for the design of the 7PB specimen, it was assumed that skin-stringer separation in the multistringer panel would initiate at an in-plane applied displacement of 2.2 mm. However, the results of the multistringer panel model show that damage initiates at a higher applied in-plane displacement of 2.6 mm. Even though it was shown in Figure 6.18 that the 7PB specimen matches relatively well with the multistringer panel, in the range of in-plane displacements 1.5 mm - 2.6 mm, the deformation of the 7PB specimen will inevitably match less well with the multistringer at an applied in-plane displacement of 2.6 mm, because it was not designed at this displacement. The difference could be reduced by redoing the design of the 7PB specimen based on the deformations in the multistringer panel at an applied in-plane displacement of 2.6 mm, but this would invalidate the purpose of using single stringer specimens to simulate the behaviour of the panel. The goal of this methodology is to obtain the damage behaviour of the panel through the single stringer specimens, without having to model the multistringer panel model in detail.

In Figure 7.20, the out-of-plane displacements of the skin along the stringer flange edge of the current 7PB specimen, the 7PB/v1/a specimen and the multistringer panel, at damage initiation, can be seen. For each of these, damage initiation occurs:

- At an applied out-of-plane displacement of 2.35 mm, for the new 7PB specimen.
- At an applied out-of-plane displacement of 3.7 mm, for the 7PB/v1/a specimen.
- At an applied in-plane displacement of 2.6 mm, for the multistringer panel.

In this plot, the point in the individual specimens corresponding to the central supporting indenter is used as the zero reference point. This way, a valid comparison can be made. From the figure, it can be seen that the overall shape of the skin in the 7PB/v1/a specimen matches quite well with the multistringer panel at damage initiation, but there is an offset in out-of-plane displacement. Considering the current 7PB specimen, it becomes clear that the difference in out-of-plane displacements with the multistringer panel is significantly decreased compared to the 7PB/v1/a specimen. Next to that, the overall shape of the skin at the stringer flange edge matches well with the multistringer panel. A small difference still exists, which could again be attributed to the fact that the 7PB specimen is designed based on the multistringer panel at an applied in-plane displacement of 2.2 mm instead of 2.6 mm. However, the effectiveness of using an area of interest focused at the skin along the stringer flange edge is proven with this analysis. This way, a more representative 7PB specimen can be obtained without having to know the exact point of damage initiation in the multistringer panel beforehand.

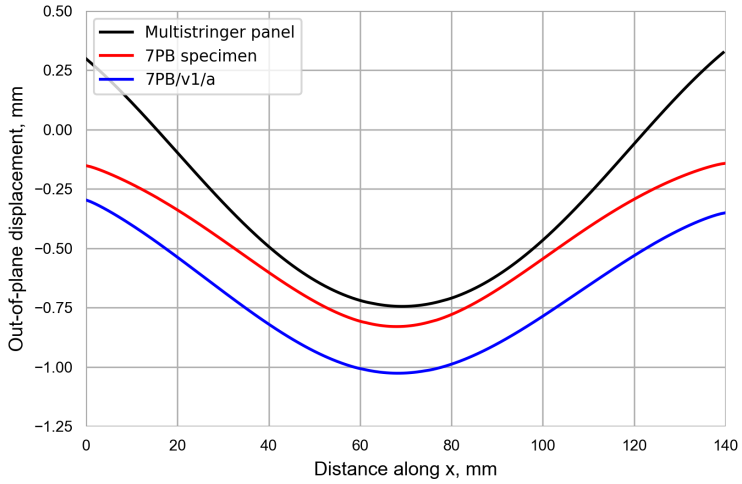

Figure 7.20: A comparison of the out-of-plane displacements of the skin at the stringer flange edge of the 7PB specimen, the original 7PB specimen and of the multistringer panel at damage initiation.

It can be concluded that the 7PB specimen can be verified with the multistringer panel in terms of damage initiation and location.

Chapter 8

Conclusions

The objective of this thesis work was to develop a numerical tool that was able to capture skin-stringer separation at critical locations of a specific multistringer panel in compression through a seven point bending (7PB) or four point twisting (4PT) specimen. The tape/fabric skin-stringer interface of the panel and the noodle regions at these interfaces had to be taken into account in the models.

Preliminary analyses were performed on a generic 7PB specimen to understand how to model the panel characteristics and to evaluate the sensitivity of the panel to different modelling parameters. In this model, a trilinear cohesive law through the superposition of two bilinear cohesive laws was used to capture the R-curve effect at the skin-stringer interface. The first bilinear law was based on standard tape/tape interface properties, while two sets of bridging properties were considered for the second bilinear law. Both these laws showed the ability to capture the R-curve effect, but literature indicates that both also show discrepancies with experimental results, so a clear "best" law could not be selected. Furthermore, the importance of the cohesive mesh was demonstrated. When the cohesive elements are too large, there are not enough cohesive elements in the cohesive zone to capture the non-linear stress state ahead of the crack tip, which leads to inaccuracies in the damage predictions.

Then, the multistringer panel in compression was modelled. The pad-up regions added to the skin and the potting at the panel ends were included in the model, since these influence the stress distribution within the panel significantly. Linear and non-linear buckling analyses were performed on the panel and the model was verified. The buckling analyses showed that the panel initially buckled at an applied displacement of approximately 1.5 mm in five halfwaves in the central bay. Then, at a displacement of 1.7 mm, the outer bays buckled as well and also in five halfwaves. An instability at an applied displacement of 2.6 mm was discovered and could not be captured with the initially used static Newton-Raphson solver. After switching to a dynamic implicit solver, it was observed that at this displacement, a mode jump occurred in the panel; the buckling mode shape in all bays suddenly changed from five to seven buckling halfwaves.

Critical locations, where skin-stringer separation was expected to occur, were identified based on the post-buckling deformations of the multistringer panel. To do so, it was assumed that

the buckling mode shape before the mode jump was critical. The location of maximum skin bending, for a mode I dominated skin-stringer separation, and the location of maximum skin twisting, for a combined mode II and mode III skin-stringer separation were identified and verified throughout the buckling analysis of the panel up until the mode jump. Based on the deformations near these critical locations, critical regions and consequently single stringer specimens were sized; a 7PB specimen for the location of maximum skin bending and a 4PT specimen for the location of maximum skin twisting. Then, for each specimen, the indenter positions were determined. To do so, an area of interest was defined that was used to calculate the shape error between the single stringer specimens and the critical regions in the multistringer panel. The importance of excluding the free edges from the area of interest was shown. Including these increased the shape error. Doing so showed that a difference in out-of-plane displacements of the skin along the stringer flange edge existed between the single stringer specimens and the multistringer panel. It is important that the displacements along this edge are accurately captured as these directly drive damage initiation and propagation. The difference could be attributed to the fact that a relatively large area of interest was used for the shape error calculation. To reduce the difference, the loading configurations were redetermined using an area of interest solely focused on the skin at the stringer flange edge. Doing so, it could be seen that the difference in out-of-plane displacements was significantly reduced, which proved the effectiveness of reducing the area of interest to find the loading configuration and to obtain a single stringer specimen that is representative of the multistringer panel without having to know the exact point of damage initiation in the panel beforehand.

Detailed damage models were then set up for the single stringer specimens. Cohesive elements were included underneath the stringer flanges and a trilinear cohesive law was applied to them. An out-of-plane displacement was applied to the loading indenter and skin-stringer separation was predicted in each of the models. The results showed that no damage occurred at the inflection point in the 4PT specimen. This indicated that, for the considered panel, a mode I dominated skin-stringer separation that is expected to occur at the location of maximum skin bending, is critical. Therefore, only the 7PB specimen was analyzed further and verified. The analysis showed that damage initiated in the 7PB specimen at an applied out-of-plane displacement of 2.35 mm, at the location of maximum bending. Considering the damage propagation, it could be seen that damage propagated in a mode I dominated fashion towards the noodle region in an elliptical shape. The stress and strain distributions within the noodle regions were investigated and a first assessment whether tensile damage occurred in the noodle region was performed based on assumed noodle properties. It could be seen that, based on the location of the maximum stresses and strains right before the damage reached the noodle region, if damage occurred in the noodle region, it would probably be in the part of the noodle at the location of maximum bending. Furthermore, comparing the maximum tensile stresses and strains to the assumed material allowables, it was revealed that with these properties, no tensile failure occurred in the noodle region of the 7PB specimen.

For the verification, a damage model was included in the multistringer panel. In this model, cohesive elements were inserted underneath the stringer flanges along the central bay and a non-linear buckling analysis up until the mode jump was performed. The results showed that damage initiated at the location of maximum skin bending at an applied in-plane displacement of 2.6 mm. Since the damage initiated right before the mode jump, no damage propagation occurred. Therefore, the 7PB specimen could not be verified with respect to this. The

verification revealed that the applied displacement at which damage initiation occurred in the 7PB specimen was slightly overpredicted. This could be attributed to the 7PB specimen being designed based on the deformations of the multistringer panel at an applied in-plane displacement of 2.2 mm, instead of 2.6 mm. Furthermore, comparison between the results of the 7PB specimen and a 7PB specimen using an area of interest that was not only focused on the skin along the stringer flange edge, confirmed that the current 7PB specimen is better representative of the multistringer panel. The 7PB specimen could be verified with the multistringer panel in terms of damage initiation and location.

With this, it can be concluded that the research objective has been achieved: skin-stringer separation in the multistringer panel has been numerically captured by a 7PB specimen. Furthermore, the importance of accurately capturing the deformation of the skin at the stringer flange edge has been proven crucial in the design of the single stringer specimens. Next to that, it was shown that a trilinear cohesive law is successful in capturing the R-curve effect associated with tape/fabric interfaces, but that comparison with experimental tests should be performed to reveal which bridging law captures the physical damage most accurately. Finally, a first assessment of the behaviour of the noodle regions was performed, which showed that if damage initiates in the noodle region, it will probably happen halfway along the 7PB specimen length.

For future research, a methodology to determine the size of the area of interest leading to an optimal representation of the skin at the stringer flange edge should be developed. Next to that, the damage propagation within the 7PB specimen should be validated with experimental tests. Furthermore, the single stringer specimen analyses should be re-executed with the structural bridging properties. This way, upon comparison with the experimental data, a substantiated choice can be made with respect to the second bilinear cohesive law in the superposed trilinear law that has been applied to the cohesive elements. On top of that, the exact noodle properties should be obtained and incorporated into the model and a damage model for the noodle region should be included. Furthermore, cohesive elements should be included at all of the noodle interfaces and underneath the interior wrap to obtain the complete damage behaviour of the single stringer specimens and the influence of the noodle region on the damage propagation.

Bibliography

[1] J. Action and U. Palliyaguru. "Testing of a multi-stringer post-buckled panel". In: *AIAA SciTech 2020 Forum*. 2020. DOI: 10.2514/6.2020-1480.

[2] R. Bai, Z. Lei, X. Wei, W. Tao, and C. Yan. "Numerical and experimental study of dynamic buckling behavior of a J-stiffened composite panel under in-plane shear". In: *Composite Structures* 166 (2017), pp. 96–103. ISSN: 0263-8223. DOI: 10.1016/j.compstruct.2017.01.022.

[3] J. Action, F. Leone, and N. Vieira De Carvalho. "Progressive damage analysis of a multi-stringer post-buckled panel". In: *AIAA SciTech 2020 Forum*. 2020. DOI: 10.2514/6.2020-1481.

[4] A. Raimondo and C. Bisagni. "Fatigue analysis of a post-buckled composite single-stringer specimen taking into account the local stress ratio". In: *Composites Part B: Engineering* 193 (2020), p. 108000. ISSN: 1359-8368. DOI: 10.1016/j.compositesb.2020.108000.

[5] L. Kootte, C. Bisagni, V. Ranatunga, S. Clay, C. Dávila, and C. Rose. "Effect of composite stiffened panel design on skin-stringer separation in postbuckling". In: *AIAA SciTech 2021 Forum* (2021), pp. 1–11. DOI: 10.2514/6.2021-0441.

[6] C. Bisagni, R. Vescovini, and C. Dávila. "Single-stringer compression specimen for the assessment of damage tolerance of postbuckled structures". In: *Journal of Aircraft* 48 (2 2011), pp. 495–502. ISSN: 1533-3868. DOI: 10.2514/1.C031106.

[7] E. Greenhalgh, C. Meeks, A. Clarke, and J. Thatcher. "The effect of defects on the performance of post-buckled CFRP stringer-stiffened panels". In: *Composites Part A: Applied Science and Manufacturing* 34 (7 2003), pp. 623–633. ISSN: 1359-835X. DOI: 10.1016/S1359-835X(03)00098-8.

[8] S. Lauterbach, A. Orifici, W. Wagner, C. Balzani, H. Abramovich, and R. Thomson. "Damage sensitivity of axially loaded stringer-stiffened curved CFRP panels". In: *Composites Science and Technology* 70 (2 2010), pp. 240–248. ISSN: 0266-3538. DOI: 10.1016/j.compscitech.2009.10.013.

[9] C. Bisagni, P. Brambilla, and C. Dávila. "Modeling delamination in postbuckled composite structures under static and fatigue loads". In: *SAMPE Conference*. 2013.

[10] J. Yetman, A. Sobey, J. Blake, and R. Shenoi. "Investigation into skin stiffener debonding of top-hat stiffened composite structures". In: *Composite Structures* 132 (2015), pp. 1168–1181. ISSN: 0263-8223. DOI: 10.1016/j.compstruct.2015.06.061.

[11] S. Masood, R. Vishakh, S. Viswamurthy, K. Gaddikeri, and I. Sridhar. "Influence of stiffener configuration on post-buckled response of composite panels with impact damages". In: *Composite Structures* 194 (2018), pp. 433–444. ISSN: 0263-8223. DOI: 10.1016/j.compstruct.2018.04.005.

[12] A. Orifici, R. Thomson, R. Degenhardt, and J. Bayandor. "The Design of postbuckling composite aerospace structures accounting for damage initiation and growth". In: *26th International Congress of Aeronautical Sciences*. 2008.

[13] A. Orifici, R. Thomson, R. Degenhardt, C. Bisagni, and J. Bayandor. "A finite element methodology for analysing degradation and collapse in postbuckling composite aerospace structures". In: *Journal of Composite Materials* 43 (26 2009), pp. 3239–3263. ISSN: 0021-9983. DOI: 10.1177/0021998309345294.

[14] C. Bisagni and C. Dávila. "Experimental investigation of the postbuckling response and collapse of a single-stringer specimen". In: *Composite Structures* 108 (1 2014), pp. 493–503. ISSN: 0263-8223. DOI: 10.1016/j.compstruct.2013.09.018.

[15] D. Zou and C. Bisagni. "Skin-stiffener separation in T-stiffened composite specimens in postbuckling condition". In: *Journal of Aerospace Engineering* 31 (4 2018). ISSN: 0893-1321. DOI: 10.1061/(ASCE)AS.1943-5525.0000849.

[16] N. Kolanu, G. Raju, and M. Ramji. "A unified numerical approach for the simulation of intra and inter laminar damage evolution in stiffened CFRP panels under compression". In: *Composites Part B: Engineering* 190 (2020), p. 107931. ISSN: 1359-8368. DOI: 10.1016/j.compositesb.2020.107931.

[17] A. Raimondo, S. Doesburg, and C. Bisagni. "Numerical study of quasi-static and fatigue delamination growth in a post-buckled composite stiffened panel". In: *Composites Part B: Engineering* 182 (2020), p. 107589. ISSN: 1359-8368. DOI: 10.1016/j.compositesb.2019.107589.

[18] C. Dávila and C. Bisagni. "Fatigue life and damage tolerance of postbuckled composite stiffened structures with indentation damage". In: *Journal of Composite Materials* 52 (7 2018), pp. 931–943. ISSN: 1530-793X. DOI: 10.1177/0021998317715785.

[19] A. Riccio, A. Raimondo, G. Di Felice, and F. Scaramuzzino. "A numerical procedure for the simulation of skin-stringer debonding growth in stiffened composite panels". In: *Aerospace Science and Technology* 39 (2014), pp. 307–314. ISSN: 1270-9638. DOI: 10.1016/j.ast.2014.10.003.

[20] A. Riccio, A. Raimondo, and F. Scaramuzzino. "A robust numerical approach for the simulation of skin-stringer debonding growth in stiffened composite panels under compression". In: *Composites Part B: Engineering* 71 (2015), pp. 131–142. ISSN: 1359-8368. DOI: 10.1016/j.compositesb.2014.11.007.

[21] A. Raimondo and A. Riccio. "Inter-laminar and intra-laminar damage evolution in composite panels with skin-stringer debonding under compression". In: *Composites Part B: Engineering* 94 (2016), pp. 139–151. ISSN: 1359-8368. DOI: 10.1016/j.compositesb.2016.03.058.

[22] N. Kolanu, G. Raju, and M. Ramji. "Experimental and numerical studies on the buckling and post-buckling behavior of single blade-stiffened CFRP panels". In: *Composite Structures* 196 (2018), pp. 135–154. ISSN: 0263-8223. DOI: 10.1016/j.compstruct.2018.05.015.

[23] H. Farokhi, O. Bacarreza, and M. Aliabadi. "Probabilistic optimisation of mono-stringer composite stiffened panels in post-buckling regime". In: *Structural and Multidisciplinary Optimization* 62 (2020), pp. 1395–1417. ISSN: 1615-1488. DOI: 10.1007/s00158-020-02565-9.

[24] F. Leone, K. Song, C. Rose, and W. Jackson. "Progressive damage analysis of post-buckled stiffened panels under static compressive loading". In: *AIAA SciTech 2020 Forum*. Vol. 1 Part F. 2020. ISBN: 9781624105951. DOI: 10.2514/6.2020-1479.

[25] R. Vescovini, C. Dávila, and C. Bisagni. "Failure analysis of composite multi-stringer panels using simplified models". In: *Composites Part B: Engineering* 45 (1 2013), pp. 939–951. ISSN: 1359-8368. DOI: 10.1016/j.compositesb.2012.07.030.

[26] A. Orifici, I. de Zarate Alberdi, R. Thomson, and J. Bayandor. "Compression and post-buckling damage growth and collapse analysis of flat composite stiffened panels". In: *Composites Science and Technology* 68 (15-16 2008), pp. 3150–3160. ISSN: 0266-3538. DOI: 10.1016/j.compscitech.2008.07.017.

[27] J. Van Rijn and J. Wiggenraad. *A seven-point bending test to determine the strength of the skin-stiffener interface in composite aircraft panels*. Tech. rep. NLR-TP-2000-044. National Aerospace Laboratory NLR, 2000.

[28] F. Leone, K. Song, W. Johnston, C. Rose, W. Jackson, C. Kosztowny, and C. Dávila. "Test/analysis correlation of damage states in post-buckled stiffened validation building block specimens". In: *American Society for Composites*. 2019. DOI: 10.12783/asc34/31277.

[29] J. Bertolini, B. Castanié, J. Barrau, J. Navarro, and C. Petiot. "Multi-level experimental and numerical analysis of composite stiffener debonding. Part 2: Element and panel level". In: *Composite Structures* 90 (4 2009), pp. 392–403. ISSN: 0263-8223. DOI: 10.1016/j.compstruct.2009.04.002.

[30] C. Dávila, F. Leone, K. Song, J. Ratcliffe, and C. Rose. "Material characterization for the analysis of skin/stiffener separation". In: *32nd American Society for Composites (ASC) Technical Conference*. 2017. DOI: 10.12783/asc2017/15407.

[31] C. Kosztowny, C. Dávila, K. Song, C. Rose, and W. Jackson. "Experimental and numerical analysis of skin-stiffener separation using a seven-point bend configuration". In: *AIAA SciTech 2019 Forum*. 2019. ISBN: 9781624105784. DOI: 10.2514/6.2019-1767.

[32] L. Kootte, C. Bisagni, C. Dávila, and V. Ranatunga. "Study of skin-stringer separation in postbuckled composite aeronautical structures". In: *Proceedings of the American Society for Composites Thirty-third Technical Conference*. 2018, pp. 1750–1761.

[33] L. Kootte and C. Bisagni. “A methodology to investigate skin-stringer separation in postbuckled composite stiffened panels”. In: *AIAA SciTech 2020 Forum*. 2020. DOI: 10.2514/6.2020-0477.

[34] M. Czabaj, J. Ratcliffe, and B. Davidson. “Observation of intralaminar cracking in the edge crack torsion specimen”. In: *Engineering Fracture Mechanics* 120 (2014), pp. 1–14. ISSN: 0013-7944. DOI: 10.1016/j.engfracmech.2014.03.002.

[35] C. Audd, B. Davidson, J. Ratcliffe, and M. Czabaj. “Reexamination of the edge crack torsion test for determining the mode III delamination toughness of laminated composites”. In: *Engineering Fracture Mechanics* 215 (2019), pp. 138–150. ISSN: 0013-7944. DOI: 10.1016/j.engfracmech.2019.05.007.

[36] J. Ratcliffe. *Characterization of the edge crack torsion (ECT) test for mode III fracture toughness measurement of laminated composites*. Tech. rep. NASA/TM-2004-213269. Hampton, Virginia: NASA Langley Research Center, 2004.

[37] C. Dávila and J. Ratcliffe. “Quasi-static and fatigue delamination at tape/fabric interfaces”. In: *AIAA SciTech 2020 Forum*. Vol. 1 Part F. 2020, pp. 1–10. ISBN: 9781624105951. DOI: 10.2514/6.2020-1384.

[38] T. Meireman, L. Daelemans, E. Van Verre, W. Van Paepegem, and K. De Clerck. “Nanofibre toughening of dissimilar interfaces in composites”. In: *Materials and Design* 195 (2020), p. 109050. ISSN: 1873-4197. DOI: 10.1016/j.matdes.2020.109050.

[39] M. Marjanović, G. Meschke, and D. Vuksanović. “A finite element model for propagating delamination in laminated composite plates based on the Virtual Crack Closure method”. In: *Composite Structures* 150 (2016), pp. 8–19. ISSN: 0263-8223. DOI: 10.1016/j.compstruct.2016.04.044.

[40] R. Krueger and P. Minguet. “Analysis of composite skin-stiffener debond specimens using a shell/3D modeling technique”. In: *Composite Structures* 81 (1 2007), pp. 41–59. ISSN: 0263-8223. DOI: 10.1016/j.compstruct.2006.05.006.

[41] A. Pereira and A. de Morais. “Mode I interlaminar fracture of carbon/epoxy multidirectional laminates”. In: *Composites Science and Technology* 64 (13-14 2004), pp. 2261–2270. ISSN: 0266-3538. DOI: 10.1016/j.compscitech.2004.03.001.

[42] W. Wagner and C. Balzani. “Simulation of delamination in stringer stiffened fiber-reinforced composite shells”. In: *Computers and Structures* 86 (9 2008), pp. 930–939. ISSN: 0045-7949. DOI: 10.1016/j.compstruc.2007.04.018.

[43] Y. Nikishkov, G. Nikishkov, G. Seon, B. Shonkwiler, and A. Makeev. “Structures technology for component damage and failure prediction”. In: *Vertical Flight Society’s 75th Annual Forum & Technology Display*. 2019.

[44] A. Rhead, Z. Sápi, S. Hutchins, R. Butler, and A. Rhead. “Novel filler materials for skin-stiffener structures”. In: *Twenty-second International Conference on Composite Materials (ICCM22)*. 2019.

[45] P. Manogharan, P. Rajagopal, and K. Balasubramaniam. “Axial guided wave technique for rapid inspection of the "noodle" regions in a stiffened composite component”. In: *AIP Conference Proceedings* 1650 (2015), pp. 668–675. ISSN: 1551-7616. DOI: 10.1063/1.4914667.

[46] Z. Sápi, R. Butler, and A. Rhead. "High fidelity analysis to predict failure in T-joints". In: *Composite Structures* 225 (2019), p. 111143. ISSN: 0263-8223. DOI: 10.1016/j.compstruct.2019.111143.

[47] X. Ma, K. Bian, H. Liu, Y. Wang, and K. Xiong. "Numerical and experimental investigation of the interface properties and failure strength of CFRP T-Stiffeners subjected to pull-off load". In: *Materials and Design* 185 (2020), p. 108231. ISSN: 1873-4197. DOI: 10.1016/j.matdes.2019.108231.

[48] A. Orifici, R. Thomson, R. Degenhardt, C. Bisagni, and J. Bayandor. "Development of a finite-element analysis methodology for the propagation of delaminations in composite structures". In: *Mechanics of Composite Materials* 43 (1 2007), pp. 9–28. DOI: 10.1007/s11029-007-0002-6.

[49] P. Camanho, C. Dávila, and M. De Moura. "Numerical simulation of mixed-mode progressive delamination in composite materials". In: *Journal of Composite Materials* 37 (16 2003), pp. 1415–1438. ISSN: 0021-9983. DOI: 10.1177/0021998303034505.

[50] W. Brocks. "Solid Mechanics and its Applications". In: vol. 244. Springer Verlag, 2018. Chap. The cohesive model, pp. 151–170. DOI: 10.1007/978-3-319-62752-6_9.

[51] P. Harper and S. Hallett. "Cohesive zone length in numerical simulations of composite delamination". In: *Engineering Fracture Mechanics* 75 (16 2008), pp. 4774–4792. ISSN: 0013-7944. DOI: 10.1016/j.engfracmech.2008.06.004.

[52] R. de Borst, M. Gutiérrez, G. Wells, J. Remmers, and H. Askes. "Cohesive-zone models, higher-order continuum theories and reliability methods for computational failure analysis". In: *International Journal for Numerical Methods in Engineering* 60 (1 2004), pp. 289–315. ISSN: 0029-5981. DOI: 10.1002/nme.963.

[53] A. Turon, C. Dávila, P. Camanho, and J. Costa. "An engineering solution for mesh size effects in the simulation of delamination using cohesive zone models". In: *Engineering Fracture Mechanics* 74 (10 2007), pp. 1665–1682. ISSN: 0013-7944. DOI: 10.1016/j.engfracmech.2006.08.025.

[54] U. Caliskan and M. Apalak. "Low speed impact behaviour of adhesively bonded foam-core sandwich T-joints". In: *Journal of Adhesion Science and Technology* 33 (3 2019), pp. 217–242. ISSN: 1568-5616. DOI: 10.1080/01694243.2018.1529882.

[55] F. Kamareh, A. Farrokhabadi, and G. Rahimi. "Experimental and numerical investigation of skin/lattice stiffener debonding growth in composite panels under bending loading". In: *Engineering Fracture Mechanics* 190 (2018), pp. 471–490. ISSN: 0013-7944. DOI: 10.1016/j.engfracmech.2017.12.043.

[56] P. Papanastasiou and E. Sarris. "Porous Rock Fracture Mechanics: With Application to Hydraulic Fracturing, Drilling and Structural Engineering". In: Elsevier Inc., 2017. Chap. Cohesive zone models, pp. 119–144. ISBN: 9780081007822. DOI: 10.1016/B978-0-08-100781-5.00006-3.

[57] A. Turon, P. Camanho, J. Costa, and C. Dávila. "A damage model for the simulation of delamination in advanced composites under variable-mode loading". In: *Mechanics of Materials* 38 (11 2006), pp. 1072–1089. ISSN: 0167-6636. DOI: 10.1016/j.mechmat.2005.10.003.

[58] A. Sane, D. Peshwe, C. Manjunatha, P. Padole, and R. Uddanwadiker. "Evaluation of progressive failure of composite T-joint using mixed mode cohesive zone model". In: *Transactions of the Indian Institute of Metals* 71 (2 2018), pp. 445–451. ISSN: 0975-1645. DOI: 10.1007/s12666-017-1189-4.

[59] *ABAQUS/Standard User's Manual, Version 2021*. Simulia, 2021.

[60] B. Bak, E. Lindgaard, and E. Lund. "Analysis of the integration of cohesive elements in regard to utilization of coarse mesh in laminated composite materials". In: *International Journal for Numerical Methods in Engineering* 99 (2014), pp. 566–586. DOI: 10.1002/nme.4688.

[61] S. Mukhopadhyay and S. Hallett. "An augmented cohesive element for coarse meshes in delamination analysis of composites". In: *Composite Structures* 254 (2020), p. 112890. DOI: 10.1016/j.compstruct.2020.112890.

[62] B. Falzon and M. Cerini. "An automated hybrid procedure for capturing mode-jumping in postbuckling composite stiffened structures". In: *Composite Structures* 73.2 (2006), pp. 186–195. DOI: https://doi.org/10.1016/j.compstruct.2005.11.053.

[63] A. Orifici, R. Thomson, I. Herszberg, T. Weller, R. Degenhardt, and J. Bayandor. "An analysis methodology for failure in postbuckling skin-stiffener interfaces". In: *Composite Structures* 86 (1-3 2008), pp. 186–193. ISSN: 0263-8223. DOI: 10.1016/j.compstruct.2008.03.023.

[64] A. Orifici, H. Abramovich, I. Herszberg, A. Kotler, T. Weller, R. Thomson, and J. Bayandor. "Failure in skin-stiffener interfaces under postbuckling loads". In: *Proceedings of the International Conference on Composite Structures (ICSS/14)*. 2008.

[65] *HexPly 8552 Product Data Sheet*. Hexcel Corporation. 2020. URL: https://www.hexcel.com/user_area/content_media/raw/HexPly_8552_us_DataSheet.pdf.